FACULTY OF SCIENCE
UNIVERSITY OF COPENHAGEN

PhD Thesis

Christian Bourjau cbourjau@cern.ch

Factorization of two-particle distributions measured in Pb–Pb collisions at $\sqrt{s_{\mathrm{NN}}} = 5.02\,\mathrm{TeV}$ with the ALICE detector

Academic advisor: Jens Jørgen Gaardhøje
Co-advisor: Kristjan Herlache Gulbrandsen

June 7, 2018

Abstract

The angular distribution of particles produced in relativistic heavy-ion collisions is commonly described in terms of their complex flow coefficients $V_n(\eta, p_{\mathrm{T}})$. This description implicitly assumes that two-particle distributions of a single collision can be described by the product of the complex flow coefficients; a property commonly referred to as factorization. The amplitude and phase of the coefficients fluctuate event-by-event and thereby break the factorization assumption for distributions which are averaged over many events. Additionally, factorization may also be broken by non-flow processes such as di-jets.

This analysis studies the factorization of sample-average two-particle distributions in the (η_a, η_b)-plane in Pb–Pb collisions at $\sqrt{s_{\mathrm{NN}}} = 5.02\,\mathrm{TeV}$. The analysis is performed over the large pseudorapidity range of $-3 < \eta < 5$ by combining the Forward Multiplicity Detector (FMD) and the Inner Tracking System (ITS) of the ALICE detector in a novel analysis method. The original factorization assumption is found to hold for particle pairs with a minimal longitudinal separation of $\Delta\eta_{\mathrm{min}} = 2.6 \pm 0.2$. A modified factorization assumption which accounts for a $|\Delta\eta|$-dependent attenuation of the two-particle Fourier coefficients due to fluctuations is also investigated. The attenuation effect is quantified by the empirical parameter F_2^{η} which is found to be in agreement with previous CMS observation at $\sqrt{s_{\mathrm{NN}}} = 2.76\,\mathrm{TeV}$ as well as with AMPT model calculations.

Acknowledgments

This thesis would not have been possible without the help and support of numerous people - certainly many more than I can name here. Nevertheless, I would like to express my gratitude to as many as I can.

First and foremost, I would like to thank my supervisors Professor Jens Jørgen Gaardhøje and Kristjan Gulbrandsen for the support and many discussions but also for the freedom to pursue my own ideas and the trust that entails. In that sense a special thanks is also due to Peter Christiansen: My very first ALICE mentor whose physics and karaoke skills were both an integral part throughout my time in this experiment. This work would not have been the same without the many discussions in the PWG/PAG meetings where Anthony Timmins and Alice Ohlson always provided me with the most valuable comments and suggestions. Many thanks also goes to the entire HEHI group group from Hans Bøggild, Børge Svane Nielsen, to Ian Bearden, and Christian Holm Christensen who made my time here so enjoyable. Furthermore, I had the incredible luck to work with people whom I am proud to also call my friends. The discussions with Freja Thoresen continuously put me on the right path again and this thesis would look very different without her comments. Helene, you should really apply for a PhD! Katarína, Laís, Meera, and Vojtěch: You are the best colleges one can wish for and who would have thought that not all Metal is trash? My doppelgänger Fabian Thiele helped me contemplate the bigger questions and I'm excited to see where our paths will cross the next time. Big thanks also goes to Marek Chojnacki for both the tips I followed and those I should have followed. In the course of my time in ALICE I traveled the world with Vytautas Vislavicius to find out that there always is a tomorrow, which is great since that allowed him to give me all those valuable comments about this thesis!

Ultimately, this thesis would also not be what it is without all the support and understanding during tough times from my friends and family. Special thanks to Jógvan, who shaped my Copenhagen experience from day one and to Esther for countless times reigniting my love for climbing. Thank you Janet, for continuing to be a source of inspiration but also for the invaluable help with this thesis itself! A very special thanks also goes out to my grandfather, Rolf Ignell, who was probably the one that sparked my love for science in the first place. Lastly, a big thanks to my parents and my sister for always having my back and understanding my troubles!

These last few years were an amazing time. Thank you all for making them possible!

Contents

Chapter 1

Introduction

Gravity, the electroweak force, and the strong force are considered the fundamental forces of nature. Each of these forces exhibit different properties and manifest them self on different length scales. Gravity is the dominant force governing the motion of gigantic celestial objects over very large distances. At the same time, gravity is too small to be studied at the small length scales of collider based experiments. Electromagnetism is well known from its applications in every-day life but is also responsible for the light seen from distant stars. Simultaneously, electromagnetism may also be studied in particle collisions making this force accessible on all lengths scales. In contrast to the previous two, the weak and strong force are confined to nuclear and sub-nuclear lengths scales in most circumstances. The weak force is famously responsible for the β-decay of atomic nuclei but is also a key component in collider based experiments. Lastly, the strong force is responsible for the formation of atomic nuclei from its individual nucleons and also describes the formation of the nucleons from its constituent quarks. Each of these forces may be regarded as the corner stone of various fields of physics and astronomy.

Heavy Ion research, including this work, is dedicated to studying the strong force and in particular its bulk properties. The strong force couples to the so-called color charged particles of the Standard Model (quarks and gluons) and is fundamentally described by Quantum-Chromodynamics (QCD). A peculiarity of the strong force is that the attraction between color charged particles increases with increasing distance. As a result color charged particles can never be observed in isolation. Under conditions of low density and temperature quarks and gluons form color neutral compound states (hadrons) such as protons and neutrons. However, it is insufficient to solely understand QCD in that regime. Neutron stars are an example of cold but high-density strongly interacting matter existing today. An example of strongly interacting matter at high temperature is the very first moment of the universe itself. The first few microseconds after the Big Bang the universe posed such hot and dense conditions that quarks and gluons were unable to form their compound states [1]. Instead, these particles formed a strongly interacting Quark-Gluon-Plasma (QGP) within which they were essentially deconfined. Expansion of the universe caused a cooling and eventually a *phase transition* to the hadronic matter which composes most of the universe today.

13.7 billion years later the Relativistic Heavy Ion Collider (RHIC) at the Brookhaven National Laboratory and subsequently the Large Hadron Collider (LHC) in Geneva succeeded to recreate small drops of QGP by colliding heavy nuclei such as gold and lead respectively. The evolution of each drop of QGP follows an evolution very similar to that of the early universe.

Describing the many-body-problem of a QGP by first principles of QCD is currently computationally impossible. Instead, a description in terms of thermodynamics and relativistic hydrodynamics emerged as a successful model. In this framework, properties of the QGP are described by the *equation of state*. Measuring the parameters of this equation has revealed that the QGP behaves as an almost perfect liquid [2]. A cornerstone of this observation was the measurement of the anisotropic *elliptic* flow in non-central collisions which is sensitive to the shear viscosity - a parameter of the equation of state. As studies of the elliptic flow became more refined initially unanticipated higher orders of anisotropic flow were also observed.

These higher order modes are now understood as a consequence of fluctuations of the initial state geometry of the particle collisions [3]. Since this realization, the study of fluctuations in Heavy Ion collisions continue to draw more attention. A property of the hydrodynamical description is that every particle in the final state must be produced independently of all other particles. This independence implies that the single-particle distribution is sufficient to describe the configuration of all the created particles. However, the experimentally accessible quantity for studying the anisotropies of the particle distributions are multi-particle distributions averaged over many events. The interpretation of the averaged distribution presents complications but also opens avenues to study the nature of event-by-event fluctuations. In 2012 researchers realized that averaged two-particle distributions exhibit deviations from the factorization assumption if the considered particles are selected from different transverse momentum (p_{T}) intervals [4]. Shortly after, this factorization breaking in p_{T} was attributed to fluctuations and was also reproduced in ideal hydrodynamic calculations [5]. More recently, attention has also turned to a factorization breaking with respect to the pseudorapidity η which has been observed p–Pb and Pb–Pb collisions at 2.76 TeV and 5.02 TeV [6, 7].

This work builds upon and extends our current knowledge of the factorizability of two-particle distributions in η by studying Pb–Pb collisions at 5.02 TeV with A Large Ion Collider Experiment (ALICE) at the LHC in Geneva, Switzerland. By combining the Forward Multiplicity Detector (FMD) and the Inner Tracking System (ITS), this analysis has access to an η-coverage of $-3.4 < \eta < 5.03$. However, the use of the FMD creates a significant and unique set of experimental challenges creating the need to adapt existing methods of analysis. The core observables of this analysis are the azimuthal Fourier coefficients $\hat{V}_{n,-n}$ of the event-sample-averaged two-particle distributions. The coefficients are measured for $n = 2$ with a resolution of 0.2 units of pseudorapidity in the (η_a, η_b)-plane yielding approximately 800 unique pair-configurations in pseudorapidity. Non-flow and decorrelation effects depending on η influence the shape of the measured $\hat{V}_{n,-n}(\eta_a, \eta_b)$ coefficients and can be quantified by fitting the observed data with an appropriate model. This work investigates two such models: The first being the often

implicitly used *pure factorization* which assumes that $\hat{V}_{n,-n}(\eta_a, \eta_b)$ can be written as the product of two identical functions of η. The second model includes *decorrelating* effects in the form of an exponential suppression of $\hat{V}_{n,-n}(\eta_a, \eta_b)$ with increasing separation between η_a and η_b.

This analysis identifies the sub-regions of the phase space, which are in good agreement with the models, and quantifies the decorrelation seen in the second model via the empirical parameter F_2^{η}. The observed decorrelation effect is compared to results published by the CMS collaboration for Pb–Pb collisions at 2.76 TeV and with model calculation based on the AMPT event-generator.

The structure of this thesis is as follows. Chapter 2 introduces the reader to the fundamental aspects of Heavy Ion Physics and the evolution of a typical Pb–Pb collision. The observables of this analysis are subsequently introduced in Chapter 3. Chapter 4 discusses the properties of multi-particle distributions and their event-sample averages. A summary of relevant previous studies is given in Chapter 5 and Chapter 6 introduces the experiment. The experimental considerations with respect to the used observables are laid out in Chapter 7. The event and tracklet selection is described in Chapter 8. Chapter 9 presents the results of this work which are discussed in Chapter 10. Lastly, a summary and perspectives for future analyses is given in Chapter 11.

Chapter 2

Heavy Ion physics

Collider based Heavy Ion (HI) physics is one of many possible fields of research in modern physics. This chapter puts emphasizes on where HI research is located in the bigger picture of subatomic physics while narrowing in on the core topics of this work. Fig. 2.1 provides a visual guide to what will be further explained in the remainder of this chapter. The Standard Model (SM) of particle physics describes the tangible world in terms of elementary particles and four force-carrying bosons. It is briefly introduced in Sec. 2.1 with a focus on the *strong force*. The properties of the strong force give rise to interesting bulk properties, in particular at high temperatures and low densities. Collisions of heavy ions provide sufficiently high temperatures to create a new state of matter, the QGP. The QGP is a core topic of HI physics and offers a unique way to study the strong force as a many-body problem. The creation and evolution of the QGP is covered in detail in Sec. 2.2.

2.1 Fundamental particles and forces

Commonly, the SM is referred to as a quantum field theory describing three of the four known fundamental interactions: electromagnetic, weak, and strong. The forth fundamental interaction is gravity which is described by general relativity. A unified description of general relativity and the SM is not known today. However, no experimental process which is simultaneously sensitive to gravity (or the graviton, its hypothetical force carrier) and the processes described by the SM is currently known.

2.1.1 The Standard Model

The SM consists of six quarks, six leptons, four force-carrying bosons and the Higgs boson. A schematic arrangement of these particles is shown in Fig. 2.2. The quarks and leptons are grouped vertically in three generations. Members of different generations differ from their counter parts only by their mass but share otherwise the same spins and charges. Ordinary matter encountered in every-day life is exclusively formed from the first generation (electrons, up-quark, and down-quark). Particles in the SM exclusively

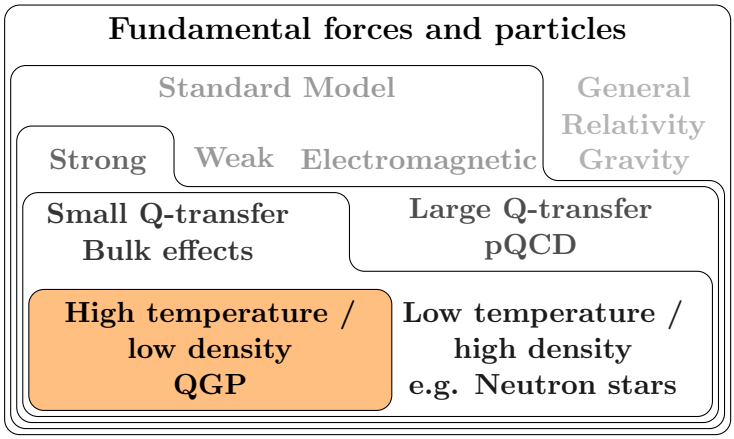

Figure 2.1: The place of heavy ion research in subatomic physics

interact with each other via the exchange of a boson. On the other hand, bosons only interact with appropriately charged particles[1]. Each of the three forces of the SM can be separated into *sectors* and are commonly studied and discussed fairly independent of each other. Heavy ion physics seeks to explain the bulk properties of the color-charged particles of the Standard Model. Such particles are described in the QCD sector of the SM which will therefore be described in more details below.

2.1.2 Quantum Chromodynamics

The color-charged particles of the SM include all the quarks and the force-carrying, massless gluons. The latter means that gluons can interact with each other, which gives rise to many distinct properties of the QCD sector. Any quark may, at any time, radiate and reabsorb a gluon. The radiated gluon may itself create a gluon-anti-gluon pair before being reabsorbed by the quark which initially emitted it. This process causes any color-charged particle to be constantly surrounded by a cloud of other color-charges seemingly enhancing the initial charge over increasing distances. This effect is referred to as *anti-screening*. The ramification of anti-screening of color-charged particles is that the attractive force between two color-charged particles increases over increasing distances. Once the field between two color-charges contains sufficient energy to create a quark-anti-quark pair, this pair may split up between the two initial color-charges and thus creating two separate, color-neutral *hadrons* such as protons or pions. This process, referred to as *color confinement*, makes it impossible to ever observe color-charged particles in isolation.

However, a high-momentum color-charged parton (quark or gluon), is capable of penetrating the color-charged cloud surrounding a separate parton. This causes the effective color-charge, and thus the *coupling constant* α_s between the two color-charged particles to decrease with increasing momentum transfers. Commonly, this effect is

[1] Or mass in case of the Higgs boson

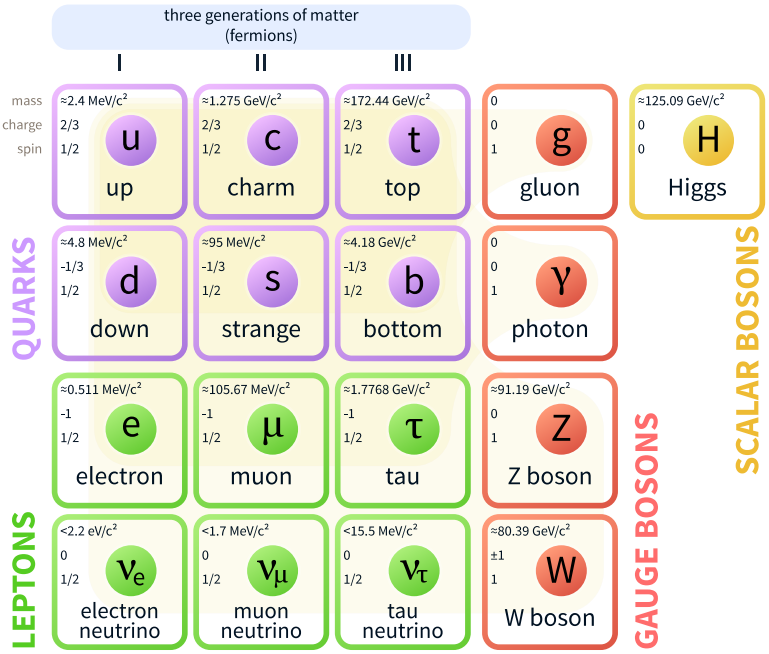

Figure 2.2: Schematic of the fundamental mass particles and force carrying bosons of the Standard Model. The background color indicates which particles interact with which bosons. The quarks and the gluon are the most important particles for HI physics. Figure taken from [8].

described as *asymptotic freedom*. Processes with a large momentum transfer and thus $\alpha_s < 1$ can be studied in the framework of *perturbative QCD* (pQCD), similar to the interaction in the electro-weak sector of the SM. However, small (also known as *soft*) momentum transfers in the order of $\sim 200\,\text{MeV}$ are very common in HI collisions and such processes cannot be described perturbatively.

Non-perturbative QCD calculations are computationally extremely expensive due to the ever increasing α_s for smaller momentum transfers. One well-established way of performing approximate, non-perturbative QCD calculations is *lattice QCD*. The ansatz of this approach is to place the involved partons on a discreet space-time grid. The spacing between the grid points provides an implicit momentum cut-off enabling the computations. Results obtained from lattice QCD can then be extrapolated to an infinitely small grid size to recover the conditions of the SM. Lattice QCD has been able to make predictions concerning the bulk property of strongly interacting matter, in particular concerning the nature of the phase-transition in QCD phase-diagram

2.1.3 The QCD phase-diagram and the Quark-Gluon Plasma

Depending on the baryon chemical potential μ_b and the temperature T, QCD matter may assume different phases which can be represented in a phase diagram like the schematic depicted in Fig. 2.3. The common state of matter found in today's universe is in the hadronic state of low temperature and density. However, the existence of other states of

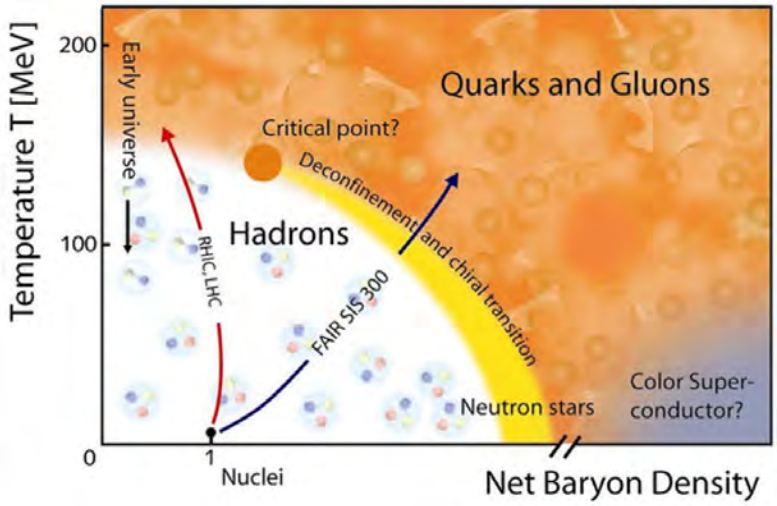

Figure 2.3: Schematic illustration of the QCD phase diagram for temperature T and net baryon density. The early universe underwent a transition from the QGP to the hadronic state which can be recreated in collider based experiments. Figure taken from [10].

matter were already theorized in the 1970s [9]. The conditions in the very first moments of our universe were sufficiently hot for strongly interacting matter to exist in a plasma-like state where color-charged particles are *deconfined* of each other[2]. This is the state which is commonly referred to as the (strongly interacting) QGP. The transition from a QGP to the hadronic state may either occur abruptly with a phase transition or in a continuous fashion by moving across the *crossover* region of the phase-diagram. In our current understanding, the universe underwent the latter evolution from the QGP to the hadronic matter found today within a few µs after the Big Bang[1].

Relativistic heavy ion collisions at the LHC and RHIC have recreated small volumes of QGP which follow a similar time evolution in the phase diagram as the early universe. Early indications that a QGP had been created at the SPS collider at the European Organization for Nuclear Research (CERN) emerged in the early 2000s [11] while the actual discovery is usually credited to the three RHIC experiments BRAHMS, PHOBOS, and STAR [12, 13, 14]. The small volumes and the rapid transition back into hadronic matter within femto-seconds still poses experimental challenges. Matters are further complicated by the fact that all stages, the creation, the evolution, and the eventual *freeze-out* of the QGP all play a role in the observable final state. The following section focuses on these three steps in the life of a drop of QGP.

[2]Deconfinement should be understood that a parton can move independently in the plasma, but its mean free path between interactions is nevertheless short.

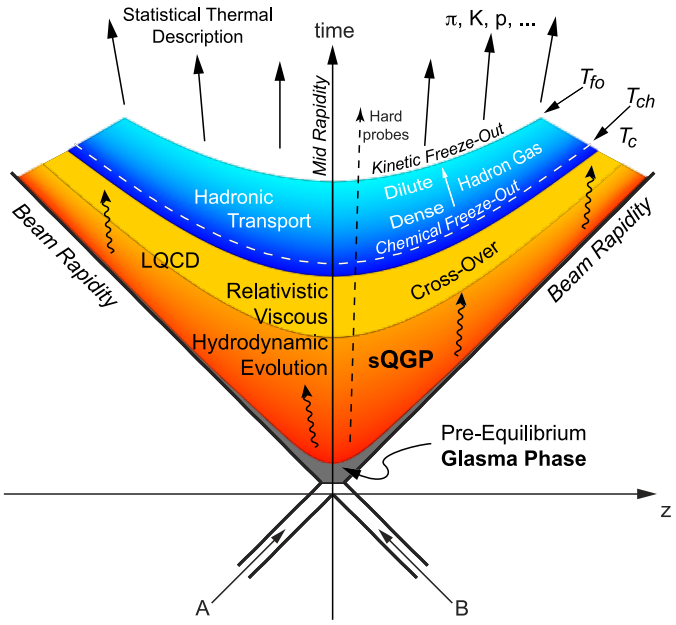

Figure 2.4: Creation, evolution, and freeze out of a QGP in heavy ion collisions. Two particles (A and B) are collided at time $t = 0$. The system then evolves with time through the depicted phases. Figure taken from [15].

2.2 The evolution of the QGP

The process of the creation, evolution and the eventual freeze-out of a QGP created in heavy ion collisions is schematically depicted in Fig. 2.4. Two particles are collided at time $t = 0$. Before a QGP is created the system evolves through a pre-equilibrium phase. This phase is possibly the least understood today and is commonly described in the framework of the Color-Glass-Condensate (CGC) [16]. Once the system has reach a state of local equilibrium, its evolution along pressure gradients can be well described in the framework of relativistic hydrodynamics. The expansion process leads to a cooling of the medium and a gradual hadronization around the critical temperature T_C. Lattice QCD calculations indicate T_C to be below between 155 and 175 MeV [17]. Shortly after the freeze-out, the condensed hadrons continue to scatter inelastically off each other until the system has cooled down to the chemical freeze-out temperature T_{ch}. It is predicted that $T_{ch} \approx T_C$ and experimental evidence indicates that this freeze-out process takes place at approximately 170 TeV [11]. After the chemical freeze-out, the system forms an elastically scattering hadron-gas. The temperature at which even these elastic scatterings cease to occurred is referred to as the kinetic freeze-out temperature.

Correlations between the final state particles stem mainly from the initial state anisotropy, which is preserved throughout the hydrodynamical evolution.

2.2.1 Color-Glass-Condensate

The CGC describes the state of the colliding nuclei prior to the actual collision. The guiding principle of the CGC is that the gluon density increases rapidly for decreasing *Bjorken* x, where x is the fraction of the total momentum of the nuclei carried by the gluon. This behavior stems from the emission and self-interaction of low-momentum gluons, as described in Sec. 2.1.2. At relativistic energies a saturation effect occurs for the low-x gluons once their wave lengths approach the size of the nuclei. At the relativistic energies achieved at modern heavy ion colliders, each of the colliding nuclei is highly Lorentz-contracted in the lab frame. At the time of impact the two nuclei pass through each other, creating a strong color field in their wake commonly referred to as *glasma*.

Initial calculations of the glasma model treated the created system as an approximately boost-invariant, 2D system [18]. However, experimental [7, 6] and theoretical [19, 20, 21] studies of the η dependent event-plane decorrelations have created the need to revisit this restriction. Recent studies of a three dimensional glasma have therefore dropped the requirement of approximate boost-invariance [22]. The rapidity dependence of the gluon density is then computed from a JIMWLK evolution which results in a rapidity dependent structure of the colliding nuclei as is illustrated in Fig. 2.5. In the respective work, the gluon fields were used as the initial conditions to solve the source free Yang-Mills equations for each rapidity individually. This in turn yields the rapidity dependent energy-momentum tensor $T^{\mu\nu}$. The tensor is symmetric [23] and each component is usually a function of the four-dimension space-time $x^\mu = (t, x, y, z)$. The components of $T^{\mu\nu}$ describes the energy and momentum flux of a system and are also a fundamental quantity in the later hydrodynamic description. Its components are schematically shown in Fig. 2.6.

The individual components of T describe the following properties of the system at a given point (t, x, y, z)

- T^{00} describes the energy density
- $T^{\mu\mu}$ describes the pressure of the system
- $T^{\mu 0}$ give the flux of mass through the surface where x^μ is constant
- The remaining off-diagonal elements $T^{\mu\nu}$ describe the flux along the surface x^μ of the ν component [23]

The component T^{00} computed with the 3D-glasma model for Pb–Pb collisions at $\sqrt{s_{\mathrm{NN}}} = 2.76\,\mathrm{TeV}$ and $0.2\,\mathrm{fs}/c$ after the collision is depicted in Fig. 2.7. While the approximate boost invariance of the energy density is apparent, clear long and short-range deviations due to the JIMWLK evolution are visible.

In the same work, agreement was found between the described gluon densities and the decorrelations effects observed experimentally. This is in agreement with previous predictions stating that the hydrodynamic evolution preserves the longitudinal structure of the glasma phase [17]. Nevertheless, the hydrodynamical evolution is crucial step for

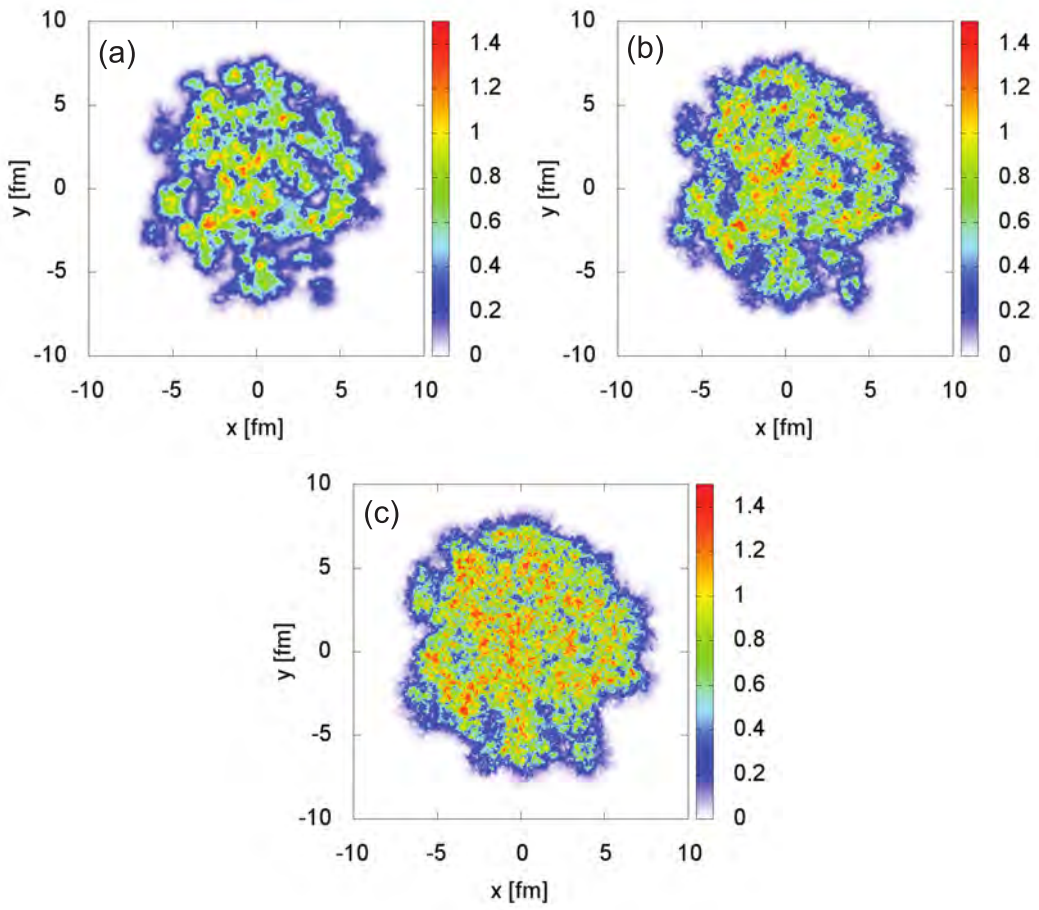

Figure 2.5: Gluon field of one of the colliding nuclei at different rapidities after the JIMWLK evolution. From (a) to (c) the panels depict the rapidities $Y = -2.4$, $Y = 0$ and $Y = 2.4$. The overall geometry remains correlated over the shown rapidity region. Figure taken from [22].

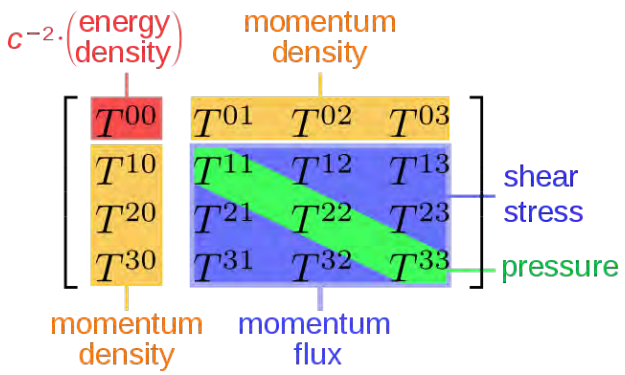

Figure 2.6: Schematic description of the energy-momentum tensor. Figure taken from [24]

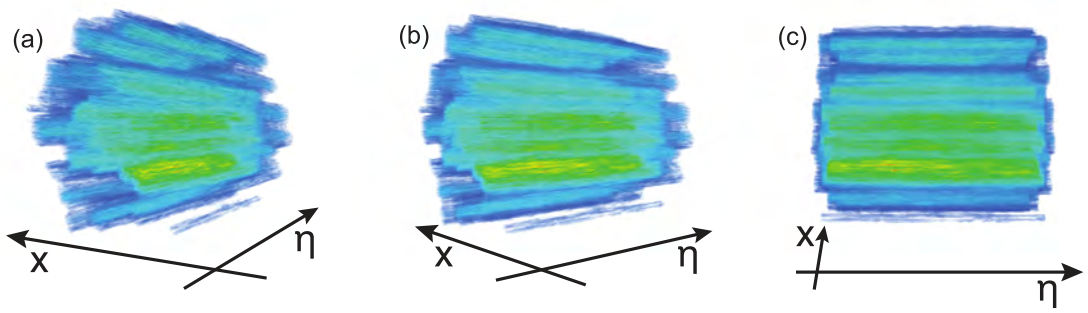

Figure 2.7: Pseudorapidity dependent energy-momentum tensor of a Pb–Pb collision at $\sqrt{s_{\mathrm{NN}}} = 2.76\,\mathrm{TeV}$ from 3D glasma calculations. The approximate boost invariance is apparent along with the η dependent structures introduced by the JIMWLK evolution. Figure taken from [22]

the descriptions of particle distribution in the transverse plane. The energy momentum tensor computed with the (3D)-glasma can be used as the initial conditions of the hydrodynamical evolution of the QGP [22].

2.2.2 Relativistic hydrodynamics

The applicability of hydrodynamics requires that the system is in *local thermodynamic equilibrium*. While various definitions of this condition exist, it can usually be described such that the pressure and temperature only vary over characteristic lengths scales which are larger than the mean free path of a particle within the system [23]. This condition is reached during the glasma phase.

If the condition of local equilibrium is given, hydrodynamics can be used to evolve the energy-momentum tensor of a system from an initial configuration to a later state. However, the evolution of the medium decreases the rate at which momentum transfers take place in the system to a point where local equilibrium is no longer applicable. Thus, hydrodynamics can only be used to evolve the system up until a *final condition* is met. A hydrodynamic description of a heavy ion collision is therefore usually followed by another model describing the hadronic freeze-out.

Equation of motion

The equations of motion of a hydrodynamic system are given by the energy-momentum conservation and the conversation of currents. The former is given by

$$\partial_\mu T^{\mu\nu} = 0 \tag{2.1}$$

where ∂_μ is the common short hand notation for the partial derivative $\partial/\partial x_\mu$ in the μ dimension. The conservation of currents is similarly given by

$$\partial_\mu N_i^\mu = 0 \tag{2.2}$$

where N_i^μ is the ith conserved current such as the electric charge or baryon number [25]. A further restriction on the evolution of the system is that the second law of thermodynamics

$$\partial_\mu S^\mu \geq 0 \tag{2.3}$$

where S^μ is the entropy current that has to be conserved.

The pressure P at the initial condition is closely related to the initial anisotropy of the energy-density and it is the driving force for the transverse evolution of the QGP. The medium will accelerate fastest along the highest pressure gradients and will thus maintain some memory of the initial state anisotropy throughout its evolution.

Once the fluid has expanded and cooled down to the freeze-out temperature one can no longer continue the hydrodynamic expansion. At this point the assumption is made that the momentum distribution of the fluid is equal to the momentum distribution of the outgoing particles and that the outgoing particles are produced *independently* of each other [23]. Lastly, the number of particles produced from one fluid element is governed by Boltzmann statistics. Since the movement of these fluid elements maps to the momentum distribution of the fluid it is possible to deduce the final state anisotropies of the QGP from the experimentally accessible particle distributions.

2.2.3 Anisotropic flow

The assumption of independently produced particles from the previous section has important ramifications for the (multi-) particle probability distributions. In its most general form the distribution of m-tuples (pairs, triplets, ...) between the created particles can be written in terms of the probability density $P_m(x_1, x_2, \ldots, x_m)$ where x_i denotes any kinematic variable of the ith particle such as p_T, η, φ etc [26]. The first restriction on this distribution is that it must be symmetric under any permutation of the particles such that

$$P_m(x_1, x_2, \ldots, x_m) = P_m(x_2, x_1, \ldots, x_m) \tag{2.4}$$

Under the assumption that the particles were produced independently, it further follows that the multi-particle probability distribution can be factorized into a products of identical single-particle distributions $P_1(x)$

$$P_m(x_1, x_2, \ldots, x_m) = \prod_{i=1}^{m} P_1(x_i) \tag{2.5}$$

It is common to describe these distribution as Fourier series. The following replaces x with the commonly used variables $(\eta, \varphi, p_\mathrm{T})$

$$P_1(\eta, \varphi, p_\mathrm{T}) = \frac{1}{2\pi} \sum_{n=-\infty}^{\infty} V_n(p_\mathrm{T}, \eta) e^{-in\varphi} \tag{2.6}$$

where the $V_n(\eta, p_\mathrm{T})$ is the nth complex Fourier coefficient in the azimuth of the single-particle distribution. These coefficients are commonly use to describe the azimuthal

anisotropies of the final state particle distributions. As written in Eq. (2.6), the coefficients dependent on η and p_{T} but are also known to depend on other kinematic variables such as the particle species. Since Eq. (2.6) is the Fourier series of a real valued function it can be written out in the terms of real valued parameters as

$$P_1(\eta, \varphi, p_{\mathrm{T}}) = \frac{1}{2\pi}\left(1 + 2\sum_{n=1}^{\infty} v_n(\eta, p_{\mathrm{T}}) \cos n\left[\varphi - \psi_n(\eta, p_{\mathrm{T}})\right]\right) \tag{2.7}$$

where v_n is commonly referred to as the nth flow coefficient and ψ_n is its corresponding phase. Naturally, a multi-dimensional Fourier transformation can also be applied to multi-particle distributions. The two-particle case, relevant for this analysis is given by

$$P_2(\eta_a, \eta_b, \varphi_a, \varphi_b, p_{\mathrm{T},a}, p_{\mathrm{T},b}) \tag{2.8}$$

$$= \left(\frac{1}{2\pi}\right)^2 \sum_{n=-\infty}^{\infty} \sum_{m=-\infty}^{\infty} V_{n,m}(\eta_a, p_{\mathrm{T},a}, \eta_b, p_{\mathrm{T},b}) e^{-in\varphi_a} e^{-im\varphi_b} \tag{2.9}$$

Where $V_{n,m}$ are the complex Fourier coefficient of the distribution. If the assumption of independent particle emission holds true, $V_{n,m}$ factorized into a product of the respective single-particle coefficients

$$V_{n,m}(\eta_a, p_{\mathrm{T},a}, \eta_b, p_{\mathrm{T},b}) = V_n(\eta_a, p_{\mathrm{T},a}) V_m(\eta_b, p_{\mathrm{T},b}) \tag{2.10}$$

By measuring the particle densities produced in heavy ion collisions, one can infer the shape of the underlying probability distributions which is quantified it with the here introduced Fourier coefficients. Furthermore, the measurement of two-particle distributions averaged over many events, gives insights into the event-by-event fluctuations of the Fourier coefficients.

2.3 Monte Carlo simulations and event generators

Monte Carlo (MC) Simulations of HI collisions allow a comparisons of theoretical predictions with observed data. This section introduces the most common techniques used for such simulations.

2.3.1 Glauber models

Glauber MC simulations are commonly used to approximate the initial conditions of a HI collision. Glauber models treat the collision as a collection of uncorrelated binary collisions between the constituents of the colliding nuclei. The nucleons inside the colliding nuclei are presumed to be randomly distributed by a Wood-Saxon distribution. When two nuclei collide, each of their nucleons may interact one or several times based on the inelastic nucleon-nucleon cross-section. The overlap (*centrality*) of a collision is parameterized by the impact parameter b defined as the distance between the two geometric centers of the colliding nuclei. Fig. 2.8 depicts a Glauber MC simulation of

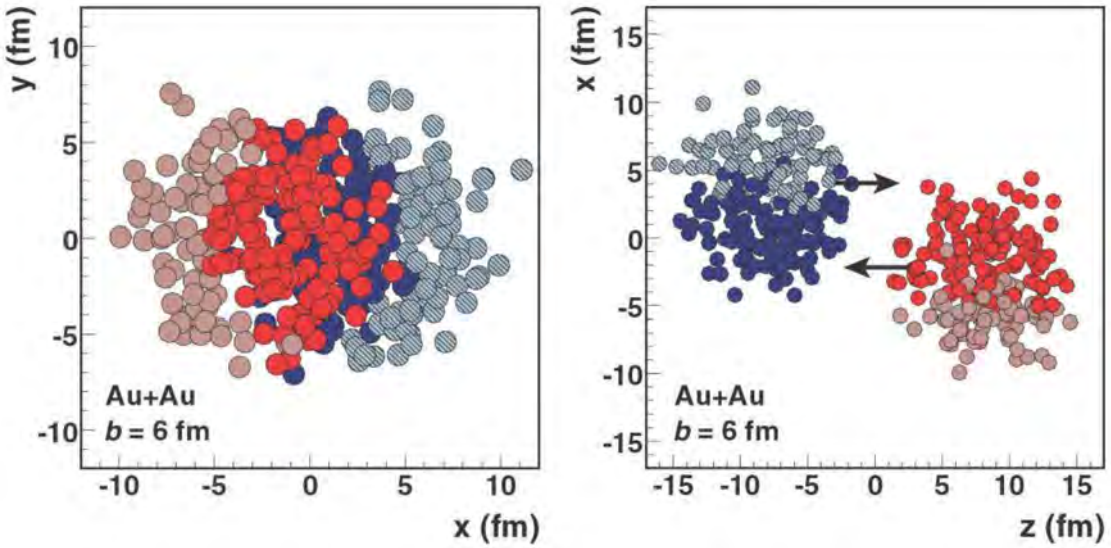

Figure 2.8: Glauber Monte Carlo simulation of a Au+Au collision viewed in the transverse plane (left) and the (x-z)-plane (right). Darker circles mark nucleons participating in the collision. Figure taken from [27].

a Au–Au collisions where the darker circles indicate participating nucleons. The initial states produced by Glauber MC simulations exhibit an initial anisotropy which is strongly dependent on the impact parameter (the "almond"-shaped overlap region in Fig. 2.8 (left)) but also exhibits significant event-by-event fluctuations.

2.3.2 HIJING

The most commonly used event generator in relativistic HI physics is Heavy Ion Jet Interaction Generator (HIJING) [28]. HIJING uses a Glauber model to compute the initial conditions of a collision. The interactions between nucleons with a large momentum transfer are described in a pQCD fashion using multiple minijets. Soft interactions are treated in the Lund-string framework. Notably, the Hijing event generator does not include processes which preserve the initial state azimuthal anisotropies. Therefore, HIJING fails to reproduce results from anisotropic flow measurements.

2.3.3 AMPT

A Multi Phase Transport model (AMPT) combines various components and techniques reflecting the complexity of a heavy ion collision [29]. The initial stage is computed using HIJING providing the full information of produced excited strings and minijets. For the *string melting* scenario, which is used for the model comparisons in this work, the excited strings and minijets are passed into Zhang's Parton Cascade (ZPC) which describes scattering processes among partons until the hadronic freeze-out. Lastly, A

Relativistic Transport (ART) model is applied to describe final hadronic rescattering processes.

Thanks to the ZPC phase, AMPT preserves information of the initial state anisotropies throughout the evolution to the final state. AMPT with string melting has been able to reproduce measurements of $v_n(\eta)$ [30] and also exhibits η-dependent event-plane fluctuations [21] which are of importance to this analysis.

Chapter 3

Observable definitions

This chapter presents a brief overview of the observables used throughout this analysis. All observables in this analysis are p_{T} integrated due to technical limitation of the detectors involved. Therefore, the following introduces all variables only with a η and φ dependence but a generalization to also include p_{T} is straight forward and presents an interesting avenue for future analyses.

3.1 One and two-particle densities

As discussed in Sec. 2.2.3, measuring anisotropies in the number of produced particles provides insights into the energy-momentum distribution of a collision. By measuring the single-particle and two-particle densities and averaging them over many events one can approximate the underlying probability distributions governing the particle production. The single-particle density is defined as

$$\hat{\rho}_1(\eta, \varphi) = \left\langle \frac{d^2N}{d\eta d\varphi} \right\rangle \tag{3.1}$$

where N is the number of particles at that given point in phase-space. Hence, $\hat{\rho}_1$ denotes the particle density averaged over many events.

The averaged density of particle pairs is similarly defined as

$$\hat{\rho}_2(\eta_a, \eta_b, \varphi_a, \varphi_b) = \left\langle \frac{d^4N_{\mathrm{pairs}}}{d\eta_a d\eta_d \varphi_a d\varphi_b} \right\rangle \tag{3.2}$$

where the subscripts a and b differentiate between the two particles in the pair.

Due to experimental considerations further explained in Chapter 7 it is beneficial to work with the *normalized two-particle density* defined by

$$r_2(\eta_a, \eta_b, \varphi_a, \varphi_b) = \frac{\hat{\rho}_2(\eta_a, \eta_b, \varphi_a, \varphi_b)}{\hat{\rho}_1(\eta_a, \varphi_a)\hat{\rho}_1(\eta_b, \varphi_b)} \tag{3.3}$$

3.2 Fourier coefficients of the two-particle distribution

A summary of the most important properties of the (multidimensional) Fourier transformation is given in Appendix C.1. The Fourier decomposition of r_2 along its azimuthal dimensions yields the two-particle Fourier coefficients

$$\hat{V}_{n,m}(\eta_a, \eta_b) = \left(\frac{1}{2\pi}\right)^2 \int_0^{2\pi} \int_0^{2\pi} r_2(\eta_a, \eta_b, \varphi_a, \varphi_b) e^{-in\varphi_a} e^{-im\varphi_b} d\varphi_a d\varphi_b \tag{3.4}$$

where the $\hat{}$ (caret symbol) emphasizes that this coefficient is calculated from the event sample average and is thus not necessary identical with the coefficients of the event-by-event distributions. In Chapter 4 it will be shown that the only non-zero modes of $\hat{V}_{n,m}(\eta_a, \eta_b)$ are $n = -m$ and that $\hat{V}_{n,-n}(\eta_a, \eta_b)$ is real.

3.3 Factorization

This analysis is concerned with the functional shape of $\hat{V}_{n,-n}(\eta_a, \eta_b)$. The two different models which are described in the following are both focused on the hydrodynamical assumption described in Sec. 2.2.3. They do not attempt to describe other processes (commonly referred to as *non-flow*) such as di-jets or weak decays. The experimental procedure of performing the factorization is described in Sec. 7.4.

3.3.1 Purely factorizing model (Model A)

In a purely hydrodynamical picture all particles are emitted independently. This property causes the two-particle Fourier coefficients to factorize on an event-by-event level. This factorization is expressed as

$$\hat{V}_{n,-n}(\eta_a, \eta_b) = \langle V_n(\eta_a) V_n^*(\eta_b) \rangle \tag{3.5}$$

$$= \left\langle v_n(\eta_a) v_n(\eta_b) e^{in(\psi_n^a - \psi_n^b)} \right\rangle \tag{3.6}$$

$$= \hat{v}_n^A(\eta_a) \hat{v}_n^A(\eta_b) \tag{3.7}$$

where $\hat{v}_n^A(\eta)$ are the flow coefficients extracted from the average over the event sample. If fluctuations of v_n are uncorrelated along η and if the event-planes ψ_n^a and ψ_n^b are always identical within one event Eq. (3.7) holds and $\hat{v}_n^A(\eta)$ is the mean value of the event-by-event flow coefficients $v_n(\eta)$. Decorrelation effects (i.e., ψ_n^a and ψ_n^b are not identical within one event), cause an attenuation of the averaged flow coefficients such that $\hat{v}_n^A(\eta) < \langle v_n(\eta) \rangle$. In that case, Model A deviates from the data if the decorrelation effects are dependent on η. The degree to which the observed $\hat{V}_{n,-n}(\eta_a, \eta_b)$ is compatible with Model A provides a limit to the size of factorization-breaking fluctuations of the flow coefficients, event-plane decorrelations and non-flow effects.

The flow coefficients $\hat{v}_n^A(\eta)$ are found as the numerical best-fit solution to the observed $\hat{V}_{n,-n}(\eta_a, \eta_b)$. The latter is measured as a histogram of finite bin size in η_a and η_b.

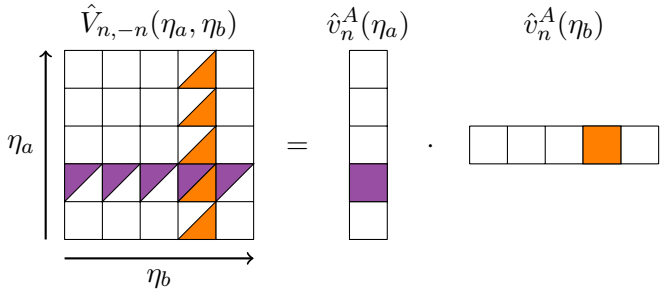

Figure 3.1: Schematic representation of Model A. Each element of $\hat{v}_n^B(\eta)$ affects several elements of $\hat{V}_{n,-n}(\eta_a, \eta_b)$.

Eq. (3.7) can therefore be seen as a non-linear equation system

$$\hat{V}_{n,-n}(\eta_a^i, \eta_b^j) = \hat{v}_n^A(\eta_a^i)\hat{v}_n^A(\eta_b^j) \tag{3.8}$$

where i and j are the bin-indices along η_a and η_b respectively. Graphically, Eq. (3.8) can be represented as shown in Fig. 3.1 where $\hat{V}_{n,-n}(\eta_a, \eta_b)$ is a two-dimensional matrix and $\hat{v}_n^A(\eta)$ a one-dimensional vector. Solving Eq. (3.8) for all points in $\hat{V}_{n,-n}(\eta_a, \eta_b)$ yields the "vector" $\hat{v}_n^A(\eta)$ which best describes the observed data.

3.3.2 Long-range decorrelating model (Model B)

The second model which is compared to the observed data was suggested by the CMS collaboration albeit based on a vastly different analysis method [6]. The model is given by

$$\hat{V}_{n,-n}(\eta_a, \eta_b) = \hat{v}_n^B(\eta_a)\hat{v}_n^B(\eta_b)e^{-F_n^\eta|\eta_a-\eta_b|} \tag{3.9}$$

The parameter F_n^η is an empirical measure for a $\Delta\eta = \eta_a - \eta_b$ dependent factorization breaking and as such provides insights into longitudinal fluctuations during the early stages of the collision [19, 21]. It is important to stress that the best fit of the observed data to either model yields $\hat{v}_n^A(\eta) \neq \hat{v}_n^B(\eta)$ unless $F_n^\eta = 0$.

The flow coefficients $\hat{v}_n^B(\eta)$ and the constant F_n^η are found by solving

$$\hat{V}_{n,-n}(\eta_a^i, \eta_b^j) = \hat{v}_n^B(\eta_a^i)\hat{v}_n^B(\eta_b^j)e^{-F_n^\eta|\eta_a^i-\eta_b^i|} \tag{3.10}$$

with respect to the measured $\hat{V}_{n,-n}(\eta_a, \eta_b)$. The analogous graphical representation of Eq. (3.10) is schematically shown in Fig. 3.2. The additional factor compared to Model A is constant along $\eta_a + \eta_b$ and exponentially attenuates $\hat{V}_{n,-n}(\eta_a, \eta_b)$ along $|\Delta\eta|$.

3.4 Factorization ratio

The non-linear character of the models proposed in Sec. 3.3.1 and Sec. 3.3.2 make the data-to-model comparison non-trivial. The observable of choice for this comparison is

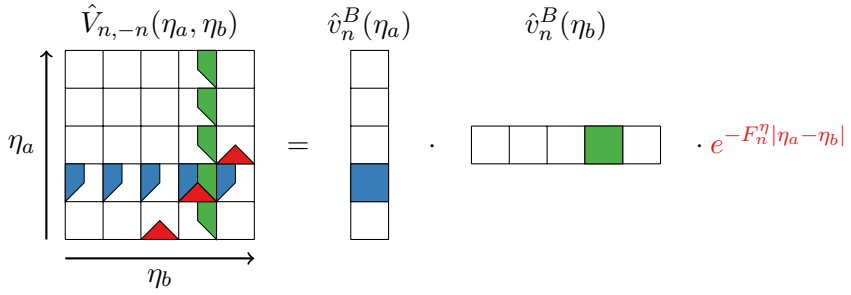

Figure 3.2: Schematic representation of Model B. Each point in $\hat{v}_n^B(\eta)$ affects several elements in $\hat{V}_{n,-n}(\eta_a, \eta_b)$. The factor $e^{-F_n^\eta|\eta_a-\eta_b|}$ attenuates $\hat{V}_{n,-n}(\eta_a, \eta_b)$ along $|\Delta\eta|$.

the ratio f_n between the observed value to the prediction of the fitted model

$$f_n(\eta_a, \eta_b) = \frac{\hat{V}_{n,-n}(\eta_a, \eta_b)}{M(\eta_a, \eta_b)} \tag{3.11}$$

where the Model $M(\eta_a, \eta_b)$ is either $\hat{v}_n^A(\eta_a)\hat{v}_n^A(\eta_b)$ for Model A or $\hat{v}_n^B(\eta_a)\hat{v}_n^B(\eta_b)e^{-F_n^\eta|\eta_a-\eta_b|}$ for Model B.

Chapter 4

Event sample averages of multi-particle distributions

The probability distribution of an individual event may be described by the complex Fourier coefficients $V_n(\eta, p_\mathrm{T})$, but these coefficients may fluctuate from event to event. More specifically, this chapter treats the flow coefficients v_n and their associated phases ψ_n as random variables. Throughout this chapter, the effects of different kinds of fluctuations of v_n and ψ_n are assessed with respect to the experimentally accessible quantities $\hat{\rho}_1$, $\hat{\rho}_2$, and $\hat{V}_{n,m}$.

The structure of this chapter is as follows: Sec. 4.1 introduces a short-hand notation which enables this chapter to be generic over any kinematic variable while maintaining a good readability. Sec. 4.2 investigates if the Fourier coefficient of an averaged (multi-) particle distribution is identical to the average of the event-by-event coefficients. Sec. 4.3 studies the averaged one- and two-particle distributions in the absence of any fluctuations and under the assumption that every event shares the same orientation in the detector. The latter restriction is relaxed in Sec. 4.4 such that the event sample contains events of any possible orientation. Sec. 4.5 then treats the scenario where the phase and the amplitude are expected to fluctuate event-by-event.

4.1 Short hand notation of this chapter

Even though the analysis presented here only performs measurements with respect to η, it is desirable to understand the effect of the averaging procedure with respect to any kinematic variable or particle species. Since the readability would suffer considerably if each possible variable were to be written out explicitly, a short-hand notation is introduced for this chapter. The only coordinates which are written out explicitly are the azimuthal coordinates φ_a and φ_b of particle a and b. All other dimensions are implicit and a superscript is used to denote that an observable is from the phase-space region a and/or b. For example, $\hat{\rho}_2^{a,b}(\varphi_a, \varphi_b)$ is to be understood as the average particle density at $(\eta_a, \eta_b, \varphi_a, \varphi_b, p_{\mathrm{T},a}, p_{\mathrm{T},b}, \ldots)$. For Fourier coefficient, the azimuthal dimensions are replaced with the modes n and m. Therefore, $\hat{V}_{n,m}(\eta_a, \eta_b, p_{\mathrm{T},a}, p_{\mathrm{T},b}, \ldots)$ is written as

$\hat{V}^{a,b}_{n,m}$. Quantities which only depend on the variables of a single-particle only have a single superscript e.g., $\hat{v}^a_n$ is to be understood as $\hat{v}_n(\eta_a, \varphi_a, p_{\mathrm{T},a}, \ldots)$.

4.2 Fourier Coefficients of an averaged distributions

Regardless of fluctuations of V_n, the question arises if the Fourier coefficients of an averaged particle distribution are identical to the average of the coefficients. This section clarifies this answer and thereby lays the groundwork for the remainder of this chapter. In the course of the following the total number of particles in an event N^{tot} is used to normalize the particle distributions. In this regard, the assumption is made that all events in the event sample have the same multiplicity. N^{tot} is therefore a constant for any configuration of v_n and ψ_n.

4.2.1 Averaged single-particle distributions

The first case to be studied is the single-particle distribution given by

$$\hat{V}^a_n = \frac{1}{2\pi}\frac{1}{N^{\mathrm{tot}}}\int_0^{2\pi} d\varphi_a e^{-in\varphi_a}\left\langle \rho^a(\varphi_a)\right\rangle \stackrel{?}{=} \left\langle V^a_n\right\rangle \tag{4.1}$$

Is $\hat{V}^a_n = \langle V^a_n\rangle$ for arbitrary fluctuations of v^a_n and ψ^a_n? The event-by-event fluctuations of the latter two parameters can be expressed by their joint probability density function (PDF) $h^a_n(v^a_n, \psi^a_n)$. The averaged single-particle distribution $\langle\rho^a(\varphi_a)\rangle$ can then be written as

$$\left\langle \rho^a(\varphi_a)\right\rangle = \int_0^{2\pi} d\psi^a_n \int_0^1 dv^a_n h^a_n(v^a_n, \psi^a_n)\left\langle \rho^a(\varphi_a)\big|_{v^a_n,\psi^a_n}\right\rangle \tag{4.2}$$

where $\left\langle\cdot\big|_{v^a_n,\psi^a_n}\right\rangle$ describes an average over events which all share identical v^a_n and ψ^a_n parameters i.e., the average is formed over events whose particle distributions are all described by the same probability distribution. For an average over many events, the mean particle density can be assumed to converged to the underlying probability distribution times the number of produced particles[1]:

$$\left\langle \rho^a(\varphi_a)\big|_{v^a_n,\psi^a_n}\right\rangle = N^{\mathrm{tot}} P^a_1(\varphi_a)\big|_{v^a_n,\psi^a_n} \tag{4.3}$$

where $P^a_1\big|_{v^a_n,\psi^a_n}$ is the probability distribution defined in Eq. (2.6), for fixed values of v^a_n and ψ^a_n. Inserting Eq. (4.2) and (4.3) into Eq. (4.1) and rearranging the order of the integrations yields

$$\hat{V}^a_n = \int_0^{2\pi} d\psi^a_n \int_0^1 dv^a_n h^a_n(v^a_n, \psi^a_n)\frac{1}{2\pi}\int_0^{2\pi} d\varphi_a e^{-in\varphi_a} P^a(\varphi_a)\big|_{v^a_n,\psi^a_n} \tag{4.4}$$

[1]For a single event, the observed particle distribution may deviate from its probability distribution due to the finite number of particles.

one can identify that the right most integral is the definition of the nth Fourier coefficient of P_1, which in turn is V_n^a as defined in Eq. (2.6). Rewriting Eq. (4.4) one more time

$$\hat{V}_n^a = \int_0^{2\pi} d\psi_n^a \int_0^1 dv_n^a h_n^a(v_n^a, \psi_n^a) V_n^a = \langle V_n^a \rangle \tag{4.5}$$

reveals that the Fourier coefficients of the averaged distribution are indeed the averaged Fourier coefficients.

4.2.2 Averaged two-particle distribution

The reasoning about the Fourier coefficients of the averaged two-particle distribution is analogous to that about single-particle distributions but with two minor differences: Firstly, the density of pairs needs to be normalized to the total number of pairs per event $N_{\text{pair}}^{\text{tot}}$ which is assumed to be identical for all events in the sample. Secondly, the joint-PDF has to be modified to include the coordinates of both particles $h_{n,m}^{a,b}(v_n^a, v_m^b, \psi_n^a, \psi_m^b)$. The averaged two-particle density is then given by

$$\begin{aligned}
&\left\langle \rho^{a,b}(\varphi_a, \varphi_b) \right\rangle \\
&= \int_0^1 dv_n^a \int_0^1 dv_m^b \int_0^{2\pi} d\psi_n^a \int_0^{2\pi} d\psi_m^b h_{n,m}^{a,b}(v_n^a, v_m^b, \psi_n^a, \psi_m^b) \left\langle \rho_2^{a,b}(\varphi_a, \varphi_b)\Big|_{v_n^a, v_m^b, \psi_n^a, \psi_m^b} \right\rangle \qquad (4.6) \\
&= \int_0^1 dv_n^a \int_0^1 dv_m^b \int_0^{2\pi} d\psi_n^a \int_0^{2\pi} d\psi_m^b h_{n,m}^{a,b}(v_n^a, v_m^b, \psi_n^a, \psi_m^b) N_{\text{pair}}^{\text{tot}} P_2^{a,b}\Big|_{v_n^a, v_m^b, \psi_n^a, \psi_m^b} \qquad (4.7)
\end{aligned}$$

where $\cdot\Big|_{v_n^a, v_m^b, \psi_n^a, \psi_m^b}$ denotes the parameters of the preceding quantity. The mean density of pairs was replaced in Eq. (4.7) by $N_{\text{pair}}^{\text{tot}} P_2^{a,b}$ where $P_2^{a,b}$, in turn, is the pair-probability-distribution defined by Eq. (2.9).

The Fourier coefficients of $\left\langle \rho_2^{a,b}(\varphi_a, \varphi_b) \right\rangle$ can be written as

$$\hat{V}_{n,m}^{ab} = \left(\frac{1}{2\pi}\right)^2 \frac{1}{N_{\text{pair}}^{\text{tot}}} \int_0^{2\pi} d\varphi_a e^{-in\varphi_a} \int_0^{2\pi} d\varphi_b e^{-im\varphi_b} \left\langle \rho_2^{a,b}(\varphi_a, \varphi_b) \right\rangle \tag{4.8}$$

By plugging Eq. (4.7) into Eq.(4.8) and using the definition in Eq. (2.9) one arrives at

$$\hat{V}_{n,m}^{ab} = \int_0^1 dv_n^a \int_0^1 dv_m^b \int_0^{2\pi} d\psi_n^a \int_0^{2\pi} d\psi_m^b h_{n,m}^{a,b}(v_n^a, v_m^b, \psi_n^a, \psi_m^b) V_{n,m}^{a,b} = \left\langle V_{n,m}^{a,b} \right\rangle \tag{4.9}$$

Using Eq. (4.5) and Eq. (4.9) it is possible to asses the effects of fluctuations and correlations by considering the mean Fourier coefficients instead of the mean distributions.

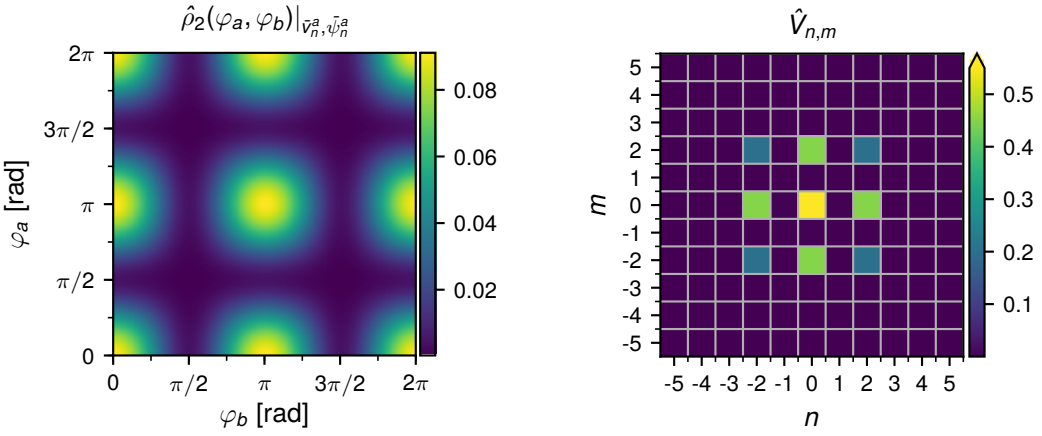

Figure 4.1: Idealized two-particle distribution $\hat{\rho}_2(\varphi^a, \varphi^b)$ (left) and its Fourier coefficients $\hat{V}_{n,m}$ (right) for constant V_n^a and V_m^b. All flow coefficients are 0 except $v_0 = 0$ and $v_2 = 0.45$. The averaged Fourier coefficients $\hat{V}_{n,m}$ exhibit non-zero off-diagonal ($n \neq -m$) elements.

4.3 Identical events at constant azimuthal orientation

This section introduces the simplest possible case: V_n^a and V_m^b do not fluctuate from event to event and their amplitudes and phases are set to ($\bar{v}_n^a$, $\bar{\psi}_n^a$) and ($\bar{v}_m^b$, $\bar{\psi}_m^b$) respectively. The event-plane of every event is identical as well i.e., every event shares the exact same orientation in the detector. Since none of the involved quantities fluctuate, the average of the single-particle V_n^a is given by

$$\langle V_n^a \rangle = \left\langle v_n^a e^{-in\psi_n^a} \right\rangle = \left\langle v_n^a \right\rangle \left\langle e^{-in\psi_n^a} \right\rangle = \bar{v}_n^a e^{-in\bar{\psi}_n^a} \tag{4.10}$$

and the two-particle coefficients by

$$\hat{V}_{n,m}^{a,b} = \left\langle V_n^a V_m^b \right\rangle = \left\langle v_n^a e^{-in\psi_n^a} v_m^b e^{-im\psi_m^b} \right\rangle = \bar{v}_n^a \bar{v}_m^b e^{-in\bar{\psi}_n^a} e^{-im\bar{\psi}_m^b} \tag{4.11}$$

An illustration of a two-particle distribution with $\bar{v}_0^a = \bar{v}_0^b = 1$ and $\bar{v}_2^a = \bar{v}_2^b = 0.45$ is shown in Fig. 4.1 (left). The amplitudes of the Fourier coefficients are shown in the right panel. In both cases, the resulting quantity is the product of two single-particle distributions or coefficients.

4.4 No fluctuations and random orientation

Even if the fluctuations between every event could be assumed to be negligibly small, each collision occurs at a random azimuthal orientation in the detector. This random orientation can be thought of as a rotation of each event by α, which is uniformly distributed in the interval $0 \leq \alpha < 2\pi$. Such a rotation of the underlying distributions is reflected by a phase shift in the Fourier coefficients.

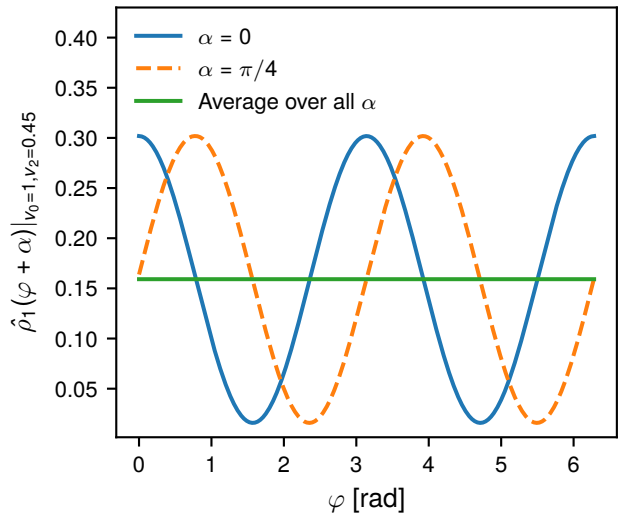

Figure 4.2: Illustration of $\hat{\rho}_1$ computed from a set of events whose particle distributions are described by identical probability distributions. The flow coefficients are set to $v_0 = 1$ and $v_2 = 0.45$. The orientation α of the events in the detector is a phase shift of the distributions. The average over all orientations yields a uniform distribution.

4.4.1 Single-particle distributions

The single-particle coefficients for events with a particular phase α is by

$$\langle V_n^a \rangle \big|_\alpha = \bar{v}_n^a e^{-in(\bar{\psi}_n^a + \alpha)} \tag{4.12}$$

Since α is uniformly distributed, the average over all possible α values is then given by

$$\langle \langle V_n^a \rangle \rangle_\alpha = \bar{v}_n^a \frac{1}{2\pi} \int_0^{2\pi} e^{-in(\bar{\psi}_n^a + \alpha)} d\alpha \tag{4.13}$$

The integral on the right hand side of Eq. (4.13) is only non-zero for $n = 0$. Thus, the averaged single-particle coefficients are given by

$$\langle V_n^a \rangle = \begin{cases} V_0^a = v_0^a & \text{if } n = 0 \\ 0 & \text{else} \end{cases} \tag{4.14}$$

Eq. 4.14 states that event-by-event anisotropies cannot be measured from the average single-particle distributions due to the random azimuthal orientation of each collision. Fig. 4.2 illustrates this for a simple sinusoidal event-by-event distribution which is randomly rotated from one collision to then next. The average over all possible phases α yields a constant, isotropic distribution which is in agreement to Eq. (4.14).

In the next section it will be shown that the same averaging procedure over a two-particle distributions does not necessarily removes all anisotropies.

4.4.2 Two-particle distributions

Analogous to the single-particle case, the average two-particle Fourier coefficient at a particular value of α is given by

$$\left\langle V_n^a V_m^b \big|_\alpha \right\rangle = \bar{v}_n^a \bar{v}_m^b e^{-in(\bar{\psi}_n^a+\alpha)} e^{-im(\bar{\psi}_m^b+\alpha)} \tag{4.15}$$

It is important to stress here that the same α is added to the azimuthal coordinate of both particles. The average of Eq. (4.15) over all possible α values is performed analogously to the single-particle case in the previous section.

$$\left\langle \left\langle V_n^a V_m^b \big|_\alpha \right\rangle \right\rangle_\alpha = \bar{v}_n^a \bar{v}_m^b \frac{1}{2\pi} \int_0^{2\pi} e^{-in(\bar{\psi}_n^a+\alpha)} e^{-im(\bar{\psi}_m^b+\alpha)} d\alpha \tag{4.16}$$

$$= \bar{v}_n^a \bar{v}_m^b e^{-in(\bar{\psi}_n^a)} e^{-im(\bar{\psi}_m^b)} \frac{1}{2\pi} \int_0^{2\pi} e^{-i\alpha(n+m)} d\alpha \tag{4.17}$$

$$= \bar{V}_n^a \bar{V}_m^b \frac{1}{2\pi} \int_0^{2\pi} e^{-i\alpha(n+m)} d\alpha \tag{4.18}$$

$$= \begin{cases} \bar{V}_n^a \bar{V}_{-n}^b & \text{if } m = -n \\ 0 & \text{otherwise} \end{cases} \tag{4.19}$$

Similarly to the single-particle distribution, certain modes of the averaged two-particle coefficients are zero regardless of their event-by-event value. However, contrary to the single-particle case, modes with $n = -m$ may assume non-zero values in Eq. (4.19). For real function such as the underlying particle distribution, negative modes of the Fourier coefficients are the complex conjugates of the positive ones:

$$V_n^b = V_{-n}^{b*} \tag{4.20}$$

Using Eq. (4.20) and examining the $m = -n$ modes of Eq. (4.15) yields

$$\left\langle V_n^a V_{-n}^b \big|_\alpha \right\rangle = \left\langle V_n^a V_n^{b*} \big|_\alpha \right\rangle \tag{4.21}$$

$$= \bar{v}_n^a \bar{v}_n^b e^{-in(\bar{\psi}_n^a+\alpha)} e^{in(\bar{\psi}_n^b+\alpha)} \tag{4.22}$$

$$= \bar{v}_n^a \bar{v}_n^b e^{-in(\bar{\psi}_n^a-\bar{\psi}_n^b)} \tag{4.23}$$

$$= \left\langle V_n^a V_n^{b*} \right\rangle \tag{4.24}$$

From Eq. (4.23) one can see that the modes $n = -m$ are not affected by the orientation of the event, since the complex conjugate makes this combination of modes independent of α. This also holds in the general case where v_n and ψ_n are allowed to fluctuate since the orientation in the detector must be independent of the underlying physical processes. Therefore, the following focuses on the non-zero modes with $n = -m$.

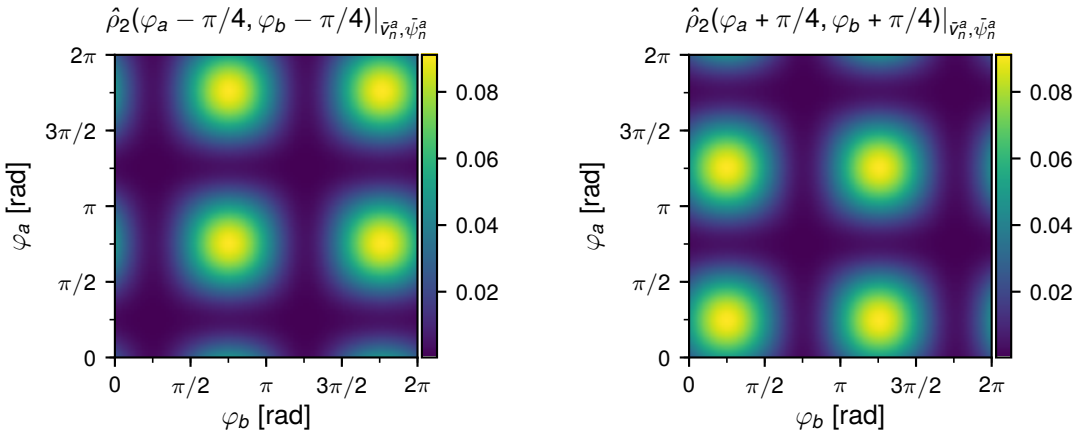

Figure 4.3: Effect of the phase-shift α on the two-particle distribution $\hat{\rho}_2(\varphi^a + \alpha, \varphi^b + \alpha)$. The distributions are identical to Fig. 4.1 (left) except that the events have been rotated by $\alpha = -\pi/4$ (left) and $\alpha = \pi/4$ (right). The phase α translates the distribution along the diagonal of the (φ^a, φ^b) plane.

4.4.3 Two-particle distribution as a one dimensional problem

Before further studying the effect of fluctuations on the sample averages, it is instructive to understand the effect of a rotation by α on the two-particle distributions themselves. Fig. 4.3 shows $\hat{\rho}_2^{a,b}(\varphi_a + \alpha, \varphi_b + \alpha)$ based on the same distribution shown in Fig. 4.2, but for $\alpha = -\pi/2$ (left) and $\alpha = \pi/2$ (right). It is evident that different values of α move the distribution along the diagonal of the (φ_a, φ_b)-plane.

An averaging over all possible α therefore creates a *striped* pattern as is shown in Fig. 4.4 (left). The right hand panel of Fig. 4.4 shows the amplitudes of the Fourier coefficients from the left panel. A comparison with Fig. 4.1 reveals that combinations of modes n, m, which were non-zero in the event-by-event case, are zero in the event average. As expected from Eq. (4.19), the only non-zero modes are indeed those where $n = -m$. The non-zero values are identical to the corresponding values of the event-by-event case in Fig. 4.1.

It is clear from the left hand panel in Fig. 4.4 that $\hat{\rho}_2(\varphi_a, \varphi_b)$ is constant along the diagonal and that the entire distribution could be described as a one dimensional problem after a coordinate transformation. In fact, such a coordinate system is commonly used in two-particle correlations analyses.

Coordinate transformation to azimuthal differences and averages

The new coordinate system is one of angular difference and averages given by

$$\Delta\varphi = \varphi_a - \varphi_b \tag{4.25}$$

$$\widetilde{\varphi} = \frac{1}{2}(\varphi_a + \varphi_b) \tag{4.26}$$

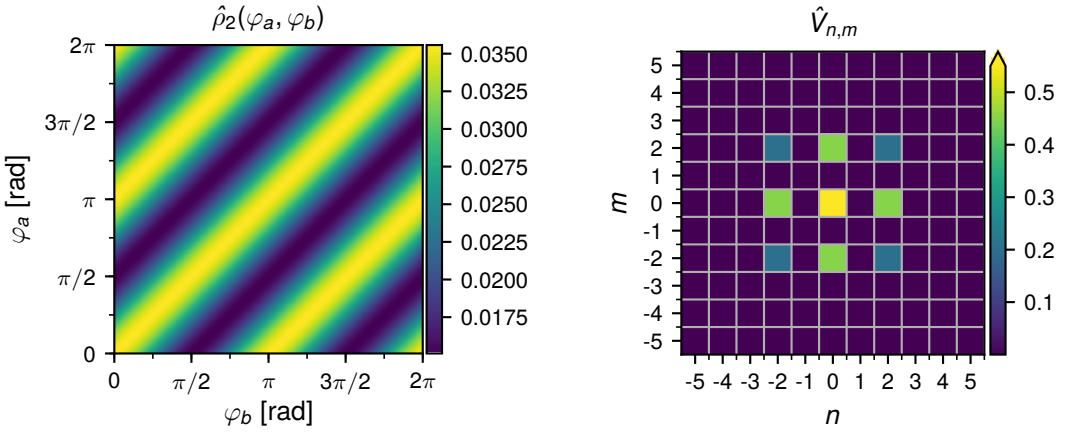

Figure 4.4: Average two-particle distribution (left) and its Fourier coefficients (right) for an event sample where every event shares an identical probability distribution but is randomly oriented in the detector.

where $\Delta\varphi$ is the azimuthal difference and $\widetilde{\varphi}$ is the azimuthal average. In Fig. 4.4 (left), $\Delta\varphi$ is perpendicular to the stripes while $\tilde{\varphi}$ is parallel.

The Jacobian of the transformation $(\varphi_a, \varphi_b) \to (\Delta\varphi, \widetilde{\varphi})$ is given by

$$\mathbf{J}(\Delta\varphi, \widetilde{\varphi}) = \begin{bmatrix} \frac{\partial(\Delta\varphi)}{\partial\varphi_a} & \frac{\partial(\Delta\varphi)}{\partial\varphi_b} \\ \frac{\partial\widetilde{\varphi}}{\varphi_a} & \frac{\partial\widetilde{\varphi}}{\varphi_b} \end{bmatrix} = \begin{bmatrix} 1 & -1 \\ \frac{1}{2} & \frac{1}{2} \end{bmatrix} \tag{4.27}$$

which yields the determinant 1.

Using the definition from Eq. 4.8, the non-vanishing coefficients ($n = -m$) are given by

$$\hat{V}^{a,b}_{n,-n} = \left\langle V^a_n V^{b*}_n \right\rangle \tag{4.28}$$

$$= \int_0^{2\pi} d\varphi_a e^{in\varphi_a} \int_0^{2\pi} d\varphi_b e^{-in\varphi_b} \frac{1}{N^{\text{tot}}_{\text{pair}}} \left\langle \rho^{a,b}_2(\varphi_a, \varphi_b) \right\rangle \tag{4.29}$$

$$= \int_0^{2\pi} d\varphi_a \int_0^{2\pi} d\varphi_b e^{in(\varphi_a - \varphi_b)} \frac{1}{N^{\text{tot}}_{\text{pair}}} \left\langle \rho^{a,b}_2(\varphi_a, \varphi_b) \right\rangle \tag{4.30}$$

Eq. (4.30) can then be rewritten as

$$\hat{V}^{a,b}_{n,-n} = \int_0^{2\pi} d\Delta\varphi e^{in(\Delta\varphi)} \int_0^{2\pi} d\tilde{\varphi} \left\langle \rho^{a,b\prime}_2(\Delta\varphi, \tilde{\varphi}) \right\rangle \tag{4.31}$$

where $\rho^{a,b'}_2$ is the two-particle distribution in the new coordinate system. The second integral is precisely the integration parallel to the isotropic strips in Fig. 4.4 (left).

Denoting the result of that integration by $\left\langle \rho_2^{a,b\prime\prime}(\Delta\varphi) \right\rangle$ one finds that

$$\hat{V}_{n,-n}^{a,b} = \int_0^{2\pi} d\Delta\varphi e^{in(\Delta\varphi)} \frac{1}{N_{\text{pair}}^{\text{tot}}} \left\langle \rho_2^{a,b\prime\prime}(\Delta\varphi) \right\rangle \tag{4.32}$$

This is indeed the one dimensional notation one intuitively expected. Eq. (4.31) shows that the two-particle coefficients extracted from the distribution of angular differences is identical to those computed from the distribution of pairs in the (φ_a, φ_b)-plane.

The real amplitude of Eq. (4.32) is often denoted as $V_{n\Delta}$ in literature. However, as shown in this section, the identical coefficients can be computed from either coordinate system and $\hat{V}_{n,-n}$ will be used to label the two-particle coefficients throughout this work.

4.5 Fluctuations of v_n and ψ_n

In Sec. 4.4 it was shown that in the absence of fluctuations $\hat{V}_{n,-n}^{a,b}$ are the only potential non-zero coefficients due to the random orientation of each event. This section turns the attention to event-by-event fluctuations of v_n and ψ_n. Such fluctuations may be random or correlated between a and b or between the amplitudes and the phases. Under the assumption that fluctuations between the amplitudes are not correlated with fluctuations in the phases, it is possible to treat each component individually

$$\hat{V}_{n,-n}^{a,b} = \left\langle V_n^a V_n^{b*} \right\rangle \tag{4.33}$$

$$= \left\langle v_n^a v_n^b \right\rangle \left\langle e^{-in(\psi_n^a - \psi_n^b)} \right\rangle \tag{4.34}$$

This assumption is made for the following two sections which will first investigate the phase-terms and then the amplitudes.

4.5.1 Fluctuating phases

The value to which the term $\left\langle e^{-in(\psi_n^a - \psi_n^b)} \right\rangle$ computes depends on the correlations of the phases between a and b. If the phases at point a and point b are not correlated, the average is given by

$$\left\langle e^{-in(\psi_n^a - \psi_n^b)} \right\rangle = \left\langle e^{-in\psi_n^a} \right\rangle \left\langle e^{in\psi_n^b} \right\rangle \tag{4.35}$$

Due to the random orientation of each event, all ψ_n^a and ψ_n^b are equally likely to occur and each of the terms on the right hand side evaluate to zero, except for the $n = 0$ mode. In that case, it is impossible to measure any anisotropies in an averaged two-particle distribution. However, two-particle distributions have been found to exhibit azimuthal anisotropies, and therefore the phases between a and b must be correlated.

Although the exact form of the correlation is unknown, one can expect that the fluctuations of the phase are equally likely in either direction. Therefore, the average must be identical if the regions a and b are reversed:

$$\left\langle e^{-in(\psi_n^a - \psi_n^b)} \right\rangle = \left\langle e^{-in(\psi_n^b - \psi_n^a)} \right\rangle \tag{4.36}$$

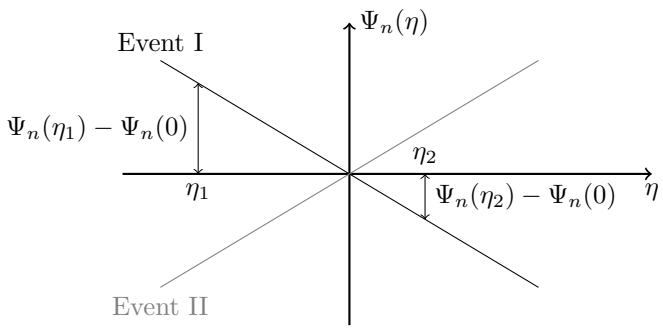

Figure 4.5: Decorrelation effect due to a linear event-plane twist with slope $-m$ (Event I) Due to symmetry considerations, a twist of m is just as likely to be found in the event sample (Event II). The decorrelation effect increases with increasing $|\Delta\eta|$ between two points.

Eq. 4.36 only holds true if the average is real valued. Based on the same consideration it follows that $|\left\langle e^{-in(\psi_n^a - \psi_n^b)} \right\rangle| < 1$. Thus, any fluctuations of the event-planes will always attenuate $\hat{V}_{n,-n}^{a,b}$.

If the fluctuations at a and b are uncorrelated, but around a common mean value Ψ_n, this attenuation will be identical for all combinations of a and b[2]. Thus, the shape of $\hat{V}_{n,-n}^{a,b}$ will be unchanged but scaled by a constant value. However, if $\Psi_n^{a,b}$ does depend on a and b, it will cause an a, b dependent attenuation of $\hat{V}_{n,-n}^{a,b}$.

A η-dependent event-plane $\Psi_n(\eta)$ is of particular relevance to this analysis. Due to the symmetry constraint in Eq. (4.36), $\Psi_n(\eta)$ must be just as common in the event sample as $\Psi_n(-\eta)$. If $\Psi_n(\eta)$ is a slowly varying function, two point with a small $|\eta_a - \eta_b| = \Delta\eta$ will exhibit a smaller decorrelation effect than points with larger separations. Fig. 4.5 illustrates this effect for a linear event-plane twist $\Psi_n(\eta)$. The further two points are separated in η, the larger their relative phase difference. From the symmetry argument discussed above, it follows that an event with $\Psi(-\eta)$ is just as likely to occur. This introduces a bias in the sample average: Pairs with a large separation in η will exhibit a stronger decorrelation behavior than pairs with a small longitudinal separation. This leads to a non-factorizable, $|\Delta\eta|$-dependent attenuation of $\hat{V}_{n,-n}^{a,b}$. It should be noted that $\Psi_n(\eta)$ does not necessarily need to be linear [21]. However, the argument that decorrelation effect increases with larger η separation still holds.

4.5.2 Fluctuating v_n

This section investigates fluctuations of the coefficients v_n in the term $\left\langle v_n^a v_n^b \right\rangle$ from Eq. (4.33). In case the fluctuations between a and b are uncorrelated, one may write the average as

$$\left\langle v_n^a v_n^b \right\rangle = \langle v_n^a \rangle \langle v_n^b \rangle \tag{4.37}$$

[2]This scenario is identical to the rotation of the event in the detector by α discussed in Sec. 4.4.

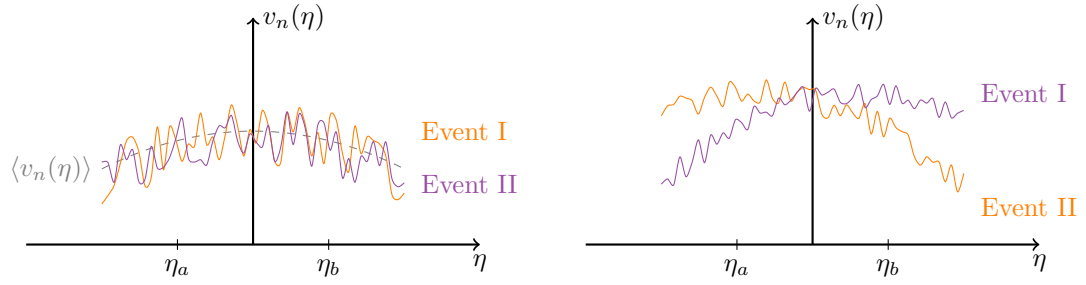

Figure 4.6: Uncorrelated (left) and correlated(right) fluctuations of $v_n(\eta)$. In the uncorrelated case, all fluctuations are around a constant mean. Correlations may arise from forward-backward asymmetries which vary event-by-event.

Note that the independence in Eq. (4.37) does not attenuate the measured $\hat{V}^{a,b}_{n,-n}$, contrary to the fluctuations of the event-planes discussed in Sec. 4.5.1.

Independence between a and b is given if the fluctuations at a have no influence on the fluctuations at b. Fig. 4.6 (left) schematically depicts this scenario where all fluctuations are local.

Fig. 4.6 (right) depicts a correlated fluctuation. The two depicted events exhibit a forward-backward asymmetry in η which may be present in individual events but not in the averaged distribution. Considering correlated fluctuations, $\left\langle v_n^a v_n^b \right\rangle$ can be written as

$$\left\langle v_n^a v_n^b \right\rangle = \left\langle v_n^a \right\rangle \left\langle v_n^b \right\rangle + \mathrm{Cov}\left[v_n^a, v_n^b\right] \tag{4.38}$$

Where $\mathrm{Cov}\left[v_n^a, v_n^b\right]$ denotes the covariance between the two points. The covariance may be a function of a and b itself or a constant. However, given the sum in Eq. (4.38), either scenario affects the factorizability of $\left\langle v_n^a v_n^b \right\rangle$.

4.5.3 Simultaneously fluctuating v_n and ψ_n

The correlations between the event-planes and the flow coefficients have recently received increased attention due to recent experimental observations of event-plane decorrelation effects [7, 6, 31]. Fig. 4.7 depicts the correlation between the event-plane differences to the relative fluctuations of the flow coefficients based on hydrodynamical calculations [20]. A stronger correlation is observed in central events than in the mid-central events.

The disentanglement of the event-plane and amplitude fluctuations is a difficult problem. Future research with the method described in this thesis could introduce a new model to fit the observed data such as

$$\hat{V}_{n,-n}(\eta_a, \eta_b) = (\hat{v}_n(\eta_a)\hat{v}_n(\eta_b) + c(\eta_a, \eta_b))e^{-F_n^{\eta}|\eta_a - \eta_b|} \tag{4.39}$$

where $c(\eta_a, \eta_b)$ reflects the sum in Eq. (4.38). However, using a sum in the fitted model creates additional technical difficulties with respect to the detector efficiencies and is outside of the scope of this work.

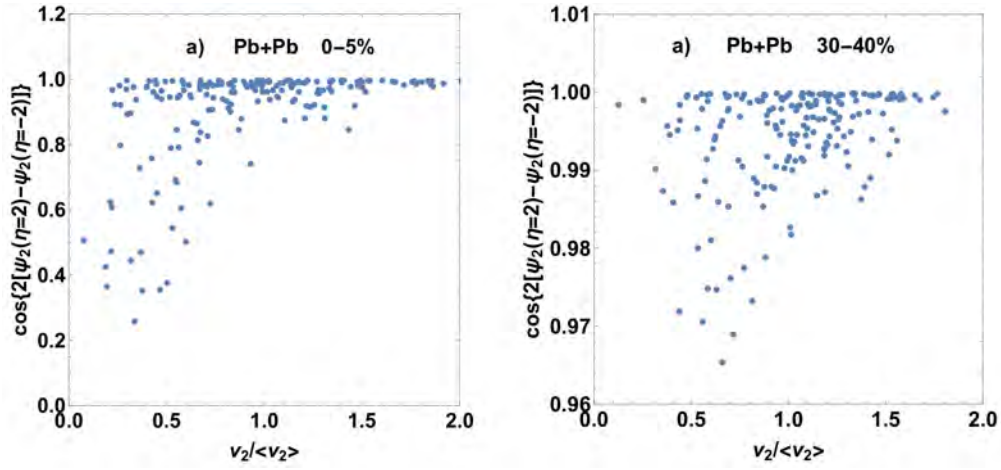

Figure 4.7: Correlation between event-plane and flow coefficient fluctuations based on 3+1D hydrodynamical calculations of Pb–Pb collisions for two different centralities. The strength of the correlation is stronger for central collisions than the mid-central ones. Figure taken from [20]

Chapter 5

Previous studies of the factorization of multi-particle distributions

The factorization of multi-particle distributions has been in the focus of research for many years. This chapter highlights some of the most important studies with respect to this analysis.

5.1 p_{T} dependent factorization breaking

5.1.1 Experimental observation

In 2012 the ALICE collaboration published a study using two-particle distributions to measure the p_{T}-dependent flow coefficients $v_n(p_{\mathrm{T}})$ based on the factorization assumption defined in Eq. (2.10) [4]. For this purpose, the two-particle correlation function, C, was measured as a function of $\Delta\varphi, \Delta\eta, p_{\mathrm{T},a}$, and $p_{\mathrm{T},b}$. It can be shown that C is proportional to the reduced two-particle distribution used in this analysis [32]. The two-particle Fourier coefficients were measured by averaging $C(\Delta\varphi, \Delta\eta, p_{\mathrm{T},a}, p_{\mathrm{T},b})$ over the interval $0.8 < |\Delta\eta| < 1.8$ and fitting the $\Delta\varphi$ distribution to the first 6 modes of a Fourier series given by

$$C(\Delta\varphi, p_{\mathrm{T},a}, p_{\mathrm{T},b}) = 1 + \sum_{n=1}^{n=6} V_{n\Delta}(p_{\mathrm{T},a}, p_{\mathrm{T},b}) \cos(n\Delta\varphi) \tag{5.1}$$

where $V_{n\Delta}(p_{\mathrm{T},a}, p_{\mathrm{T},b})$ are the p_{T}-dependent two-particle Fourier coefficients. In the absence of correlated fluctuations and event-plane decorrelations, $V_{n\Delta}(p_{\mathrm{T},a}, p_{\mathrm{T},b})$ can be written as

$$V_{n\Delta}(p_{\mathrm{T},a}, p_{\mathrm{T},b}) = \langle v_n(p_{\mathrm{T},a}) \rangle \langle v_n(p_{\mathrm{T},b}) \rangle \tag{5.2}$$

A fitting procedure similar to the one described in Sec. 3.3.1 was performed on $V_{n\Delta}(p_{\mathrm{T},a}, p_{\mathrm{T},b})$ under the assumption of pure factorization:

$$V_{n\Delta}(p_{\mathrm{T},a}, p_{\mathrm{T},b}) = v_n^{\mathrm{fit}}(\eta) v_n^{\mathrm{fit}}(\eta) \tag{5.3}$$

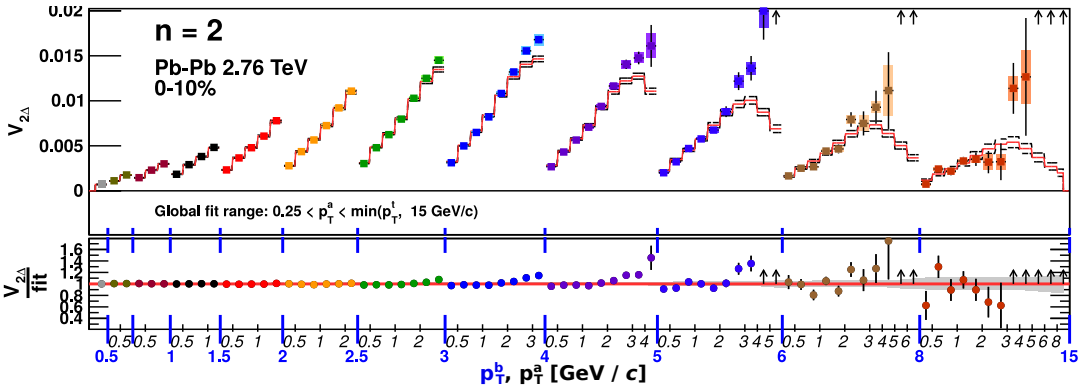

Figure 5.1: Factorization of $V_{2\Delta}(p_{\mathrm{T},a}, p_{\mathrm{T},b})$ in Pb–Pb collisions at 2.76 TeV [4]. Top: Unique combinations of all p_{T}-bins of the measured $V_{2\Delta}$ coefficient (points) and the best-fit factorized form (red lines). Bottom: Factorization ratio $r_n^{p_{\mathrm{T}}}$. Arrows indicate points outside of the plotted range.

The degree to which the factorization assumption holds was evaluated using the factorization ratio defined by

$$r_n^{p_{\mathrm{T}}}(p_{\mathrm{T},a}, p_{\mathrm{T},b}) = \frac{V_{n\Delta}(p_{\mathrm{T},a}, p_{\mathrm{T},b})}{v_n^{\mathrm{fit}}(p_{\mathrm{T},a}) v_n^{\mathrm{fit}}(p_{\mathrm{T},b})} \tag{5.4}$$

The coefficients $V_{n\Delta}(p_{\mathrm{T},a}, p_{\mathrm{T},b})$ were measured form particles with $0.5\,\mathrm{GeV}/c < p_{\mathrm{T}} < 15\,\mathrm{GeV}/c$ and are shown for $n = 2$ on an interleaved $p_{\mathrm{T},a}, p_{\mathrm{T},b}$ axis in Fig. 5.1. The fitting procedure was performed over the entire $(p_{\mathrm{T},a}, p_{\mathrm{T},b})$-plane without explicitly excluding any regions of the phase space. However, an implicit bias toward pairs of low-p_{T} particles due to the larger statistical weight is present in the measurement. The results of the fitting procedure is shown as red lines in Fig. 5.1 (top). The ratio between the measured $V_{n\Delta}(p_{\mathrm{T},a}, p_{\mathrm{T},b})$ and the resulting fit is shown in the bottom panel. It was observed that the purely factorizing model of Eq. (5.3) is not able to simultaneously describe pairs of low-p_{T} particles and pairs of high-p_{T} particles. This breaking of the factorization assumption was attributed to non-flow effects [4].

5.1.2 Factorization breaking in ideal hydrodynamics

Following the observation of p_{T}-dependent factorization breaking it was realized that such an effect is not necessarily a non-flow effect but rather a consequence of initial state fluctuations and the averaging over events [5]. The factorization ratio used to study this claim is

$$r_n^{\text{3-point}}(p_{\mathrm{T},a}, p_{\mathrm{T},b}) = \frac{\langle V_n^*(p_{\mathrm{T},a}) V_n(p_{\mathrm{T},b})\rangle}{\sqrt{\langle V_n^*(p_{\mathrm{T},a}) V_n(p_{\mathrm{T},a})\rangle \langle V_n^*(p_{\mathrm{T},b}) V_n(p_{\mathrm{T},b})\rangle}} \tag{5.5}$$

Eq. (5.5) compares 3 points in the $(p_{\mathrm{T},a}, p_{\mathrm{T},b})$-plane and yields unity if all three points are compatible with the factorization assumption. In contrast to the factorization ratio $r_n^{p_{\mathrm{T}}}$ defined in Eq. (5.4), $r_n^{\text{3-point}}$ is not biased by the higher statistical weight of low-p_{T}

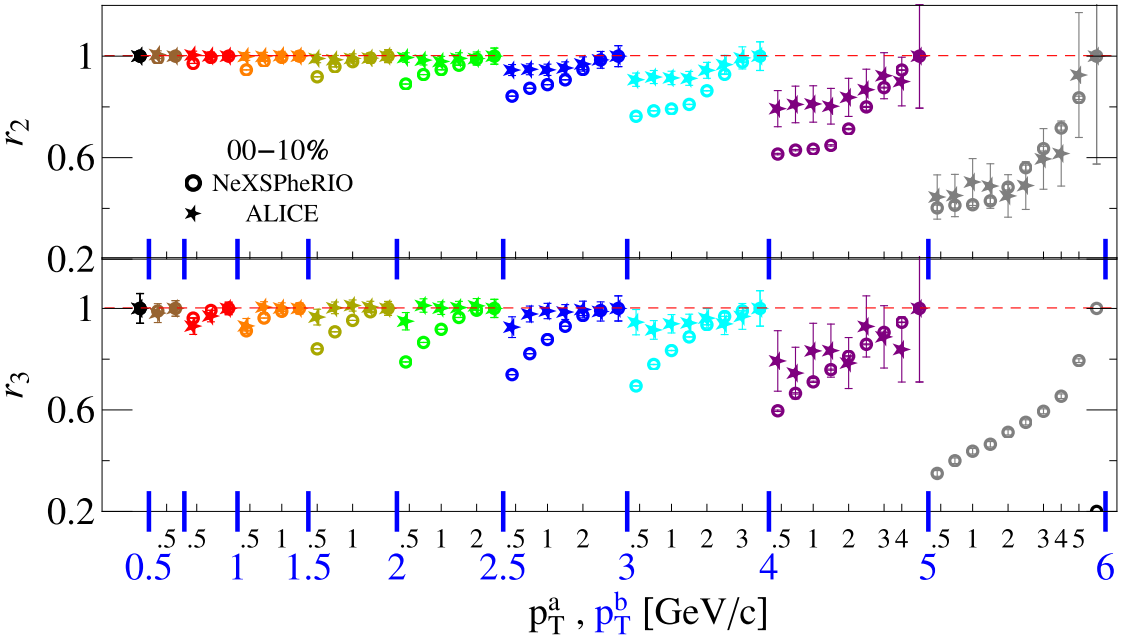

Figure 5.2: Factorization ratio $r_n^{3-\mathrm{point}}$ for $V_{n\Delta}(p_{\mathrm{T}}^a, p_{\mathrm{T}}^b)$ in Pb–Pb collisions at 2.76 TeV for the 10% most central events (stars) (see Fig. 5.1). The ALICE results are compared with the results from ideal hydrodynamics simulations (NeXSPheRIO) for Au–Au collisions at 200 GeV. Figure taken from [5].

particles. Under the expectation that $V_n(p_{\mathrm{T}})$ varies smoothly with p_{T}, two particles at $p_{\mathrm{T},a}$ and $p_{\mathrm{T},b}$ will exhibit an increasingly large decorrelation effect for an increasing separation in p_{T}. In Eq. (5.5), the nominator is susceptible to such decorrelations while the two terms in the denominator always correlate two-particles with identical p_{T}. The effect of such fluctuations is evaluated using the NeXSPheRIO relativistic ideal hydrodynamics event generator with fluctuating initial conditions. NeXSPheRIO simulated Au–Au collisions at $\sqrt{s_{\mathrm{NN}}} = 200\,\mathrm{GeV}$. The factorization ratio given by Eq. (5.5) is shown for $n = 2$ and $n = 3$ for the simulated events in Fig. 5.2.

The simulation is compared with the previously discussed ALICE observations in Pb–Pb collisions at $\sqrt{s_{\mathrm{NN}}} = 2.76\,\mathrm{TeV}$ [4]. The ideal hydrodynamic simulation exhibits a factorization breaking of similar trend and larger magnitude than the experimental observation. The factorization breaking of the simulated data set originated exclusively from initial state fluctuations. Therefore, the observation of a factorization breaking is in agreement with hydrodynamics and not necessarily a non-flow effect.

Subsequent studies by the CMS collaboration observed a similar factorization breaking in p_{T} and further compared their observations to two different initial state models - MC Glauber and MC-KLN - in the framework of viscose hydrodynamics [6]. The results of that study are shown in Fig. 5.3 as a function of momentum difference between the two particles a and b. The simulations succeeded in qualitatively describing the trend of the experimental data, but failed to predict the correct scale of the factorization break-

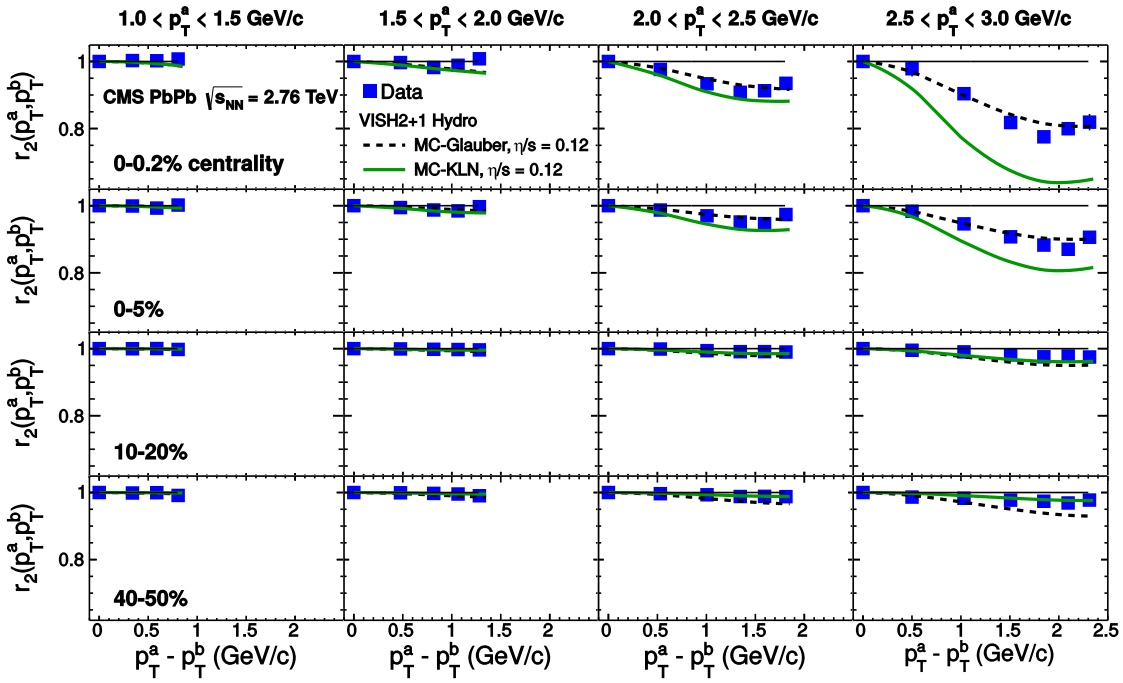

Figure 5.3: p_{T}-dependent factorization ratio $r_2^{\text{3-point}}(p_{\mathrm{T},a}, p_{\mathrm{T},b})$ for various centralities (rows) and values of p_{T}^a (columns) in Pb–Pb collisions at 2.76 TeV [6]. The results of viscose hydrodynamic simulations are shown for the MC-Glauber and MC-KLN initial condition models at $\eta/s = 0.12$. A significant factorization breaking is observed for central events and for particle pairs with large separations in p_{T} and large values of p_{T}^a. The simulations reproduce the correct shape of the factorization breaking but fail to quantitatively describe the data.

ing. The factorization was found to be largely insensitive to the shear viscosity (η/s) used in the hydrodynamical evolution.

5.2 η-dependent factorization breaking

In Ref. [5], it was also suggested to perform a similar study with respect to the relative difference between particles in η. However, using a factorization ratio analogous to the one defined in Eq. (5.5) for pseudorapidity instead of p_{T} is not feasible. Particle pairs with a small $\Delta\eta$-separation are known to often originate from non-flow processes such as di-jets or weak decays. It is therefore not appropriate to use such pairs in a study which seeks to investigate the factorization breaking from a hydrodynamic perspective.

The CMS collaboration proposed a factorization ratio which is based on asymmetries

caused by decorrelation effects [6]. The ratio is given by

$$r_n^{\mathrm{CMS}}(\eta_a, \eta_b) = \frac{\hat{V}_{n,-n}(\eta_a, \eta_b)}{\hat{V}_{n,-n}(-\eta_a, \eta_b)} \tag{5.6}$$

$$= \frac{\langle v_n(-\eta_a) v_n(\eta_b) \cos\left[n\left(\Psi_n(-\eta_a) - \Psi_n(\eta_b)\right)\right]\rangle}{\langle v_n(\eta_a) v_n(\eta_b) \cos\left[n\left(\Psi_n(\eta_a) - \Psi_n(\eta_b)\right)\right]\rangle} \tag{5.7}$$

For symmetric collision systems $\langle v_n(\eta_a)\rangle$ has to be symmetric around $\eta_a = 0$. It is then further assumed that fluctuations in the amplitudes of the Fourier coefficients are uncorrelated to the event-planes Ψ_n and to each other[1]. Under these assumptions, one can simplify Eq. (5.7) to

$$r_n^{\mathrm{CMS}}(\eta_a, \eta_b) \approx \frac{\langle \cos\left[n\left(\Psi_n(-\eta_a) - \Psi_n(\eta_b)\right)\right]\rangle}{\langle \cos\left[n\left(\Psi_n(\eta_a) - \Psi_n(\eta_b)\right)\right]\rangle} \tag{5.8}$$

It is important to understand the limits of Eq. (5.8). In the case of $\eta_a = 0$ the ratio yields unity by construction. On the other hand, if η_a approaches η_b one has to expect increasing short-range non-flow contributions in the denominator causing a deviation from unity. Therefore, care has to be taken to only interpret values of $r_n^{\mathrm{CMS}}(\eta_a, \eta_b)$ which are sufficiently far away from these two limits. The measurement was performed on pairs formed between a track in the Tracker ($|\eta| < 2.5$) and a hit in the forward calorimeter (HF+) which has an an η-coverage of $3 < \eta < 5.2$. The ratio $r_n^{\mathrm{CMS}}(\eta_a, \eta_b)$ was then evaluated for various values of η_a in the central rapidity region and for a constant value of η_b in the HF+. The η_b bins which were evaluated in the forward regions are $3.0 < \eta_b < 4.0$ and $4.4 < \eta_b < 5.0$. Fig. 5.4 depicts the regions of the (η_a, η_b)-plane used in the CMS analysis based on these acceptances. The corresponding factorization ratios are shown in Fig. 5.5 for various centralities. A significant deviation from unity is observed in all centrality bins. A dependence on η_b is also observed and strongest in central and peripheral collisions. As depicted in Fig. 5.4, the study for $3.0 < \eta_b < 4.0$ includes particle pairs with a $|\Delta\eta| < 0.5$. Such a small separation might include sizable non-flow contributions.

The observed factorization breaking is attributed to event-plane decorrelations according to Eq. (5.8). In order to quantify the effect, an empirical parametrization is introduced:

$$\cos\left[n\left(\Psi_n(\eta_a) - \Psi_n(\eta_b)\right)\right] = e^{-F_n^{\eta}|\eta_a - \eta_b|} \tag{5.9}$$

where F_n^{η} is the identical parameter introduce in the definition of Model B in Eq. (3.9). For small $\Delta\eta = \eta_a - \eta_b$ Eq. (5.9) is approximately linear and r_n^{CMS} can be expressed by

$$r_n^{\mathrm{CMS}}(\eta_a, \eta_b) \approx e^{-2F_n^{\eta}\eta_a} \tag{5.10}$$

[1] Considering the discussion in Sec. 4.5, the validity of these assumptions may be drawn in question. If the assumptions are not valid, the interpretation of the observed factorization breaking cannot be conclusively attributed to an event-plane fluctuation but may also be caused by fluctuations of the flow coefficients.

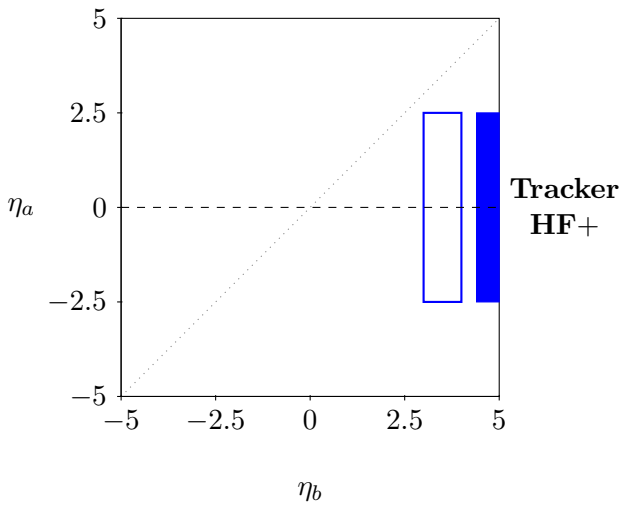

Figure 5.4: The regions of the (η_a, η_b)-plane used for the measurements shown in Fig. 5.5. Asymmetries of $\hat{V}_{n,-n}(\eta_a, \eta_b)$ are evaluated across the dashed line. The gray dotted line marks $\eta_a = \eta_b$.

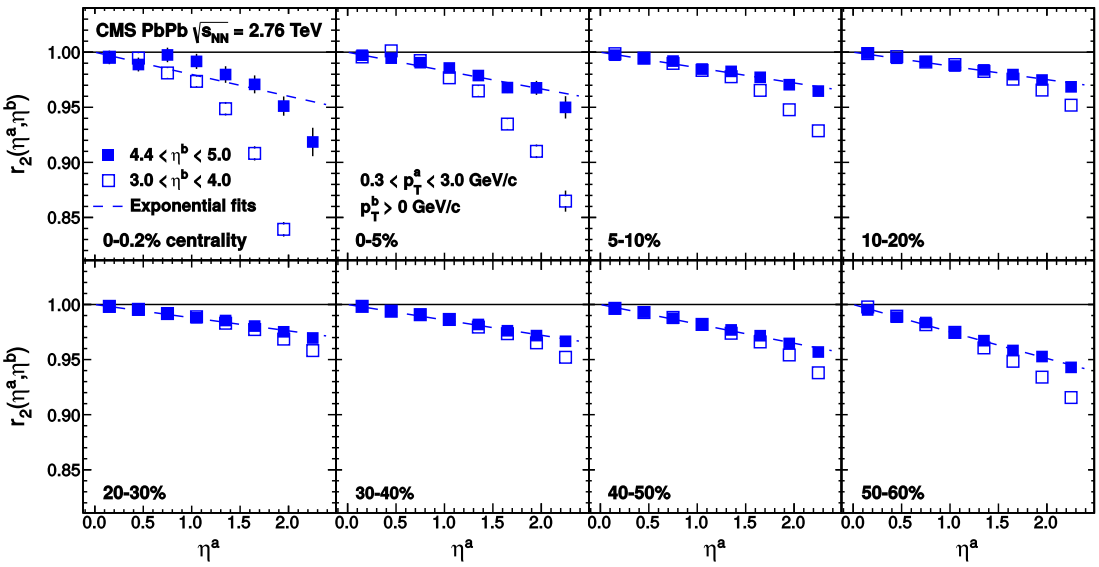

Figure 5.5: η_a dependent factorization ratios as defined in Eq. (5.8) for Pb–Pb collisions at 2.76 TeV at various centralities [6]. A η_a-dependence is observed for all centralities. A dependence on η_b is most pronounced for the most central and most peripheral events. The dashed lines correspond to the fit to the data for $4.4 < \eta_b < 5.0$ according to Eq. (5.10).

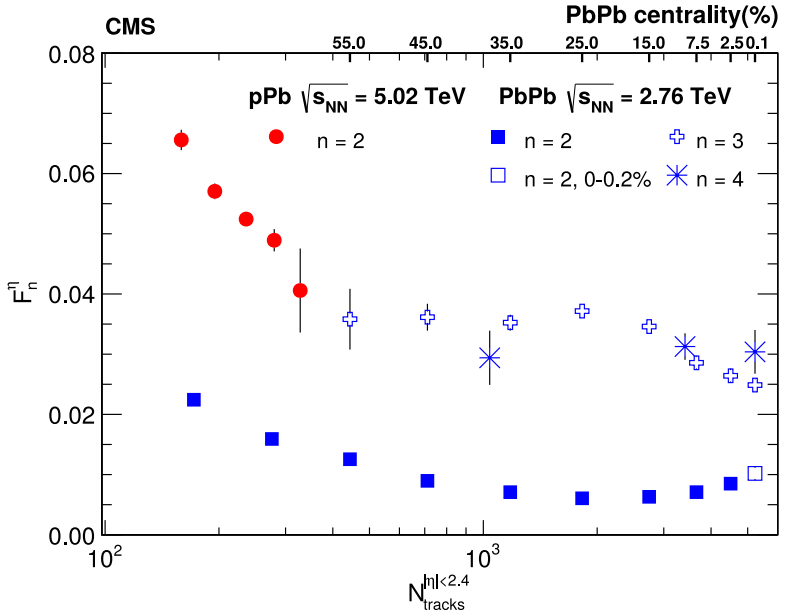

Figure 5.6: Measurements of the empirical decorrelation parameter F_n^η as a function of centrality for Pb–Pb collisions at 2.76 TeV and p–Pb collisions at 5.02 TeV (not further discussed here) [6]. A significant centrality dependence is observed for $n = 2$.

Therefore, F_n^η can be measured from r_n^{CMS} by performing a fit according to Eq. (5.10). The result of the fit is shown in Fig. 5.5 as the dashed blue line. The corresponding F_n^η parameters are depicted in Fig. 5.6.

5.3 Factorization breaking as non-flow identification

The PHOBOS collaboration conducted a study to identify the minimal $|\Delta\eta|$-gap necessary for the factorization assumption to hold for $\hat{V}_{2,-2}(\eta_a, \eta_b)$ in 200 GeV Au–Au collisions [33]. Therefore, that study bears strong resemblance to the identification of $\Delta\eta_{\mathrm{min}}$ in this work. The factorization of $\hat{V}_{2,-2}(\eta_a, \eta_b)$ was performed according to Model A defined in Eq. (3.7) at various $\Delta\eta$-gaps. The measured $\hat{V}_{2,-2}(\eta_a, \eta_b)$ is shown in Fig. 5.7 (left) and the factorized best-fit for $|\Delta\eta| \geq 2$ is shown on the (right).

Instead of forming a factorization ratio similar to the one in this analysis, the assumption is made that the non-flow contributions can be regarded as an addition to the observed $\hat{V}_{2,-2}(\eta_a, \eta_b)$. Under that assumption the non-flow $\delta(\eta_a, \eta_b)$ can be isolated by

$$\delta(\eta_a, \eta_b) = \hat{V}_{2,-2}(\eta_a, \eta_b) - v_2^A(\eta_a) v_2^A(\eta_b) \tag{5.11}$$

The non-flow contributions of Fig. 5.7 (left) are depicted in Fig. 5.8.

If the non-factorizing non-flow only extends to a maximal $|\Delta\eta|$, any factorization with a $|\Delta\eta|$-gap larger than that extent will yield identical values of $\delta(\eta_a, \eta_b)$. In order

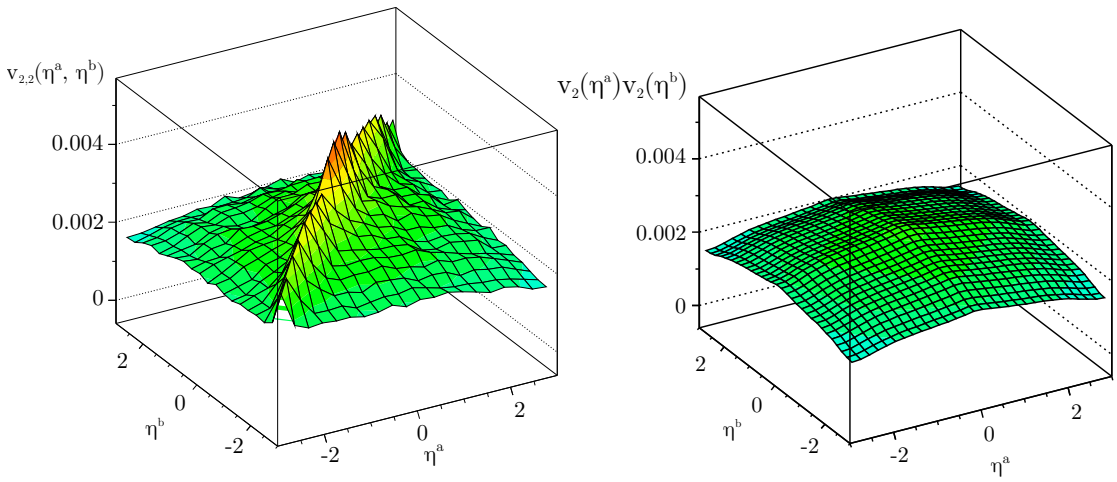

Figure 5.7: $\hat{V}_{2,-2}(\eta_a, \eta_b)$ (left) of Au–Au collisions at 200 GeV and the fitted factorization (right) [33]. The factorization was conducted with a minimal separation between the particle pairs of $|\Delta\eta| \geq 2$. The non-factorizable short-range non-flow is clearly visible along the diagonal of the (η_a, η_b)-plane.

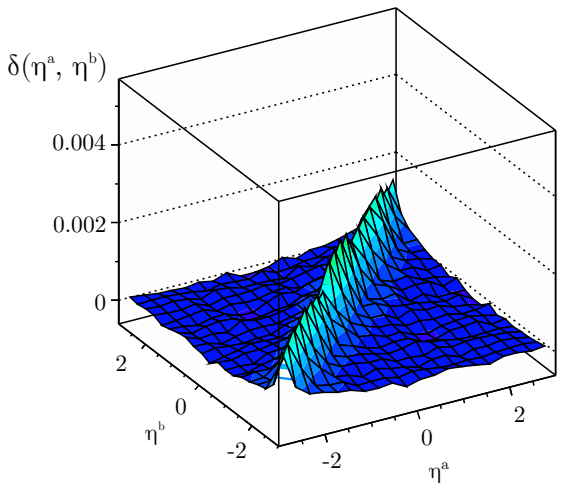

Figure 5.8: Non-flow in Au–Au collisions at 200 GeV isolated by means of factorization in the long-range region [33]. The non-flow contribution is largest for particle pairs with small separations in η. The factorization assumption appears to hold well for particle pairs with a separation larger than $|\Delta\eta| \geq 2$.

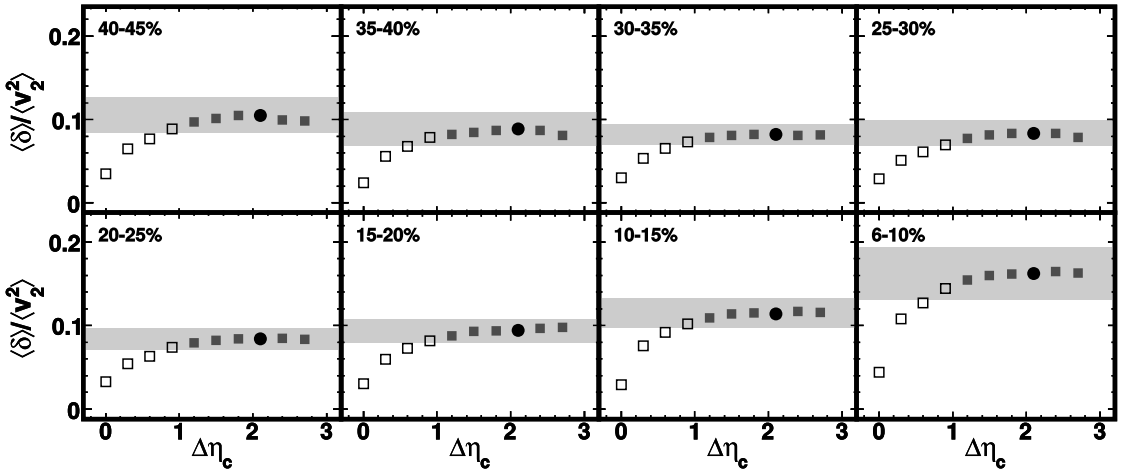

Figure 5.9: Ratio of non-factorizable non-flow δ to the factorized flow coefficients $v_2(\eta)$ for various values of $|\Delta\eta_c|$ (the minimal η separation between particle pairs) [33]. The gray band denotes the 90% C.L. of the systematic uncertainty. A convergence of the non-flow contribution is observed for $\Delta\eta_c \geq 2$.

to asses if such a behavior is observed in the data the following ratio is defined

$$r_2^{\text{PHOBOS}}(\Delta\eta_C) = \frac{\langle \delta(\eta_a, \eta_b)|_{\Delta\eta_C} \rangle}{\left\langle \hat{V}_{2,-2}(\eta_a, \eta_b) \right\rangle} \tag{5.12}$$

where $\Delta\eta_C$ is the $|\Delta\eta|$-gap applied during the factorization, $\cdot|_{\Delta\eta_C}$ denotes that this result was formed with the gap $\Delta\eta_C$, and $\langle\cdot\rangle$ is an average over the entire (η_a, η_b)-plane. If r_2^{PHOBOS} converges to a constant value for increasing $\Delta\eta_C$ this can be interpreted as having excluded the non-factorizing non-flow effects. The ratio $r_2^{\text{PHOBOS}}(\Delta\eta_C)$ for Au–Au collisions at 200 GeV is shown in Fig. 5.9 for various centralities. A convergence to a constant value is observed for all centralities and the minimal required $|\Delta\eta|$-gap is determined to be $|\Delta\eta| \gtrsim 2$.

Chapter 6

The ALICE Experiment

CERN was established in 1954 as one of Europe's first scientific joint ventures. It has since grown from its original 12 member states to 22 member states and now houses the LHC as well as ALICE. This chapter provides an introduction to these facilities with a particular focus on the subdetectors which were used in this analysis.

6.1 The Large Hadron Collider

CERN has housed various particle accelerators in the past which are partly still in use for other experiments or as pre-accelerators for the LHC. The LHC itself measures 27 km in circumference and is currently the worlds largest and most powerful accelerator. It is situated approximately 100 m underground on the boarder between France and Switzerland and provides high energy particle collisions to four large experiments: ALICE, ATLAS, CMS, and LHCb. All four of these experiments maintain a heavy ion program and are involved in the analysis of proton–proton (pp), proton–lead (pPb), xenon–xenon (Xe–Xe), and lead–lead (Pb–Pb) collisions. Each of the four main experiments has a specific focus in the field of particle or nuclear physics. ALICE is the dedicated heavy ion experiment.

6.2 ALICE

ALICE is a global collaboration composed of 1800 members distributed over 176 institutes in 41 countries [34]. The experiment was designed to study soft, non-perturbative QCD physics such as the QGP and participates in the data collection for all collision systems provided by the LHC. The entire experiment measures $16 \times 16 \times 25\,\mathrm{m}^3$ and is composed of 18 subdetector systems. A schematic drawing of the detector and its subsystems is depicted in Fig. 6.1. The main design goal of the experiment was to provide an excellent momentum resolution and particle identification [36] in the central rapidity region of $-0.8 < \eta < 0.8$; often also referred to as the central barrel. The central barrel consists of six detectors (arranged from the interaction point): The Inner

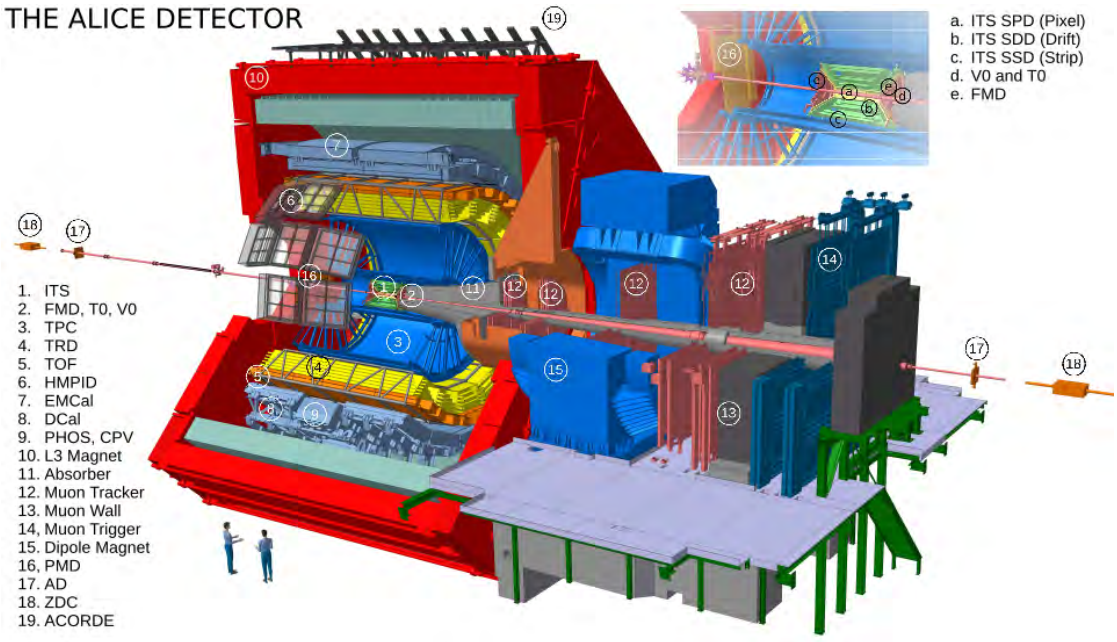

Figure 6.1: Schematic drawing of ALICE and its subdetectors. Taken from [35]

Tracking System (ITS), Time Projection Chamber (TPC), Transition Radiation Detector (TRD), Time of Flight (TOF), and the High-Momentum Particle Identification Detector (HMPID). Furthermore, ALICE is equipped with several detectors at smaller angles at the backward and forward rapidities. The detectors in the forward region which are relevant for this analysis are the FMD and the VZERO (often also referred to as V0) detector. The former is used in this analysis to measure the particle distributions in the forward and backward acceptance while the latter is used for triggering and multiplicity estimation purposes. All of these detectors operate within a magnetic field of 0.5 T provided by a solenoid magnet (L3).

The detectors coordinate system follows the common conventions used in collider based experiments where the z-axis is aligned with the direction of the beam. The nominal Interaction Point (IP) is centered in the detector at $z = 0\,\mathrm{cm}$, but collisions may occurred displaced from the IP.

It is very common for analyses in ALICE to not use all subdetectors simultaneously and this analysis is no exception. The primary factor for the choice of the deployed detectors is to optimize the longitudinal acceptance while also maintaining a sufficient resolution in η as well as in the azimuth. The FMD provides a very large η acceptance of $-3.4 < \eta < -1.7$ and $1.7 < \eta < 5.0$ but neither provides tracking nor p_{T} resolution capabilities. The full tracking capabilities of the central barrel are only available within $-0.9 < \eta < 0.9$ which would leave large acceptance gaps at $0.9 < |\eta| < 1.7$. In order to maximize the η coverage, the decision was made to only use the two inner most layers of the ITS when estimating the particle densities. This increased the acceptance in the

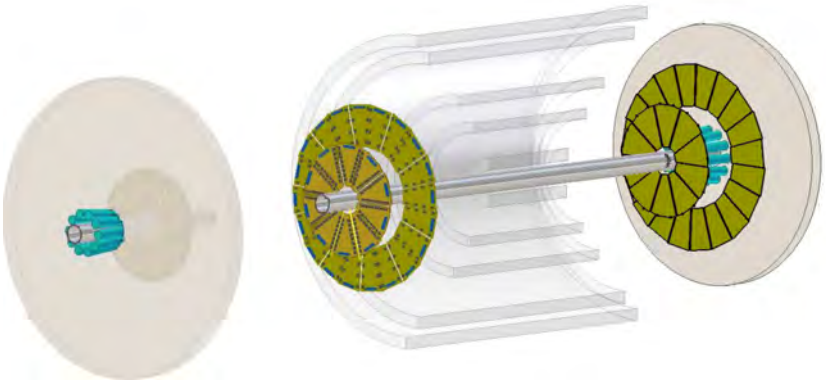

Figure 6.2: Schematic drawing of ITS and the forward detectors. The cylindrical layers are the ITS, the dark-brown disk are the subsystems of the FMD. The turquoise components are the T0 and the light brown disks are the VZERO detectors. The IP is located in the center of the ITS. Figure is taken with modifications from [37].

central region to $-1.5 < \eta < 1.5$. As in most analysis by ALICE, the VZERO detector was used for triggering purposes. The detectors which are used in this analysis are depicted in Fig. 6.2 and are described in more details in the following.

6.2.1 The Inner tracking system and the SPD

The ITS is one of the core detectors of ALICE which plays a vital role in almost all analyses. Its primary design goals were the capability to reconstruct the primary vertex of a collision to within less than 100 µm, while also providing crucial tracking information for particle identification[36]. The ITS has full azimuthal coverage and surrounds the beam pipe. The ITS directly supports the beam pipe to avoid relative movements during operation. The inner tracking system is itself composed of three subdetectors: the Silicon Pixel Detectors (SPD), the Silicon Drift Detectors (SDD), and the Silicon Strip Detectors (SSD). The SPD as the inner most detector is situated $r = 3.9\,\text{cm}$ from the interaction point while the outermost SSD is located at $r = 43.0\,\text{cm}$. If all three subdetectors are combined for tracking purposes, the ITS has a coverage of $|\eta| < 0.9$, but it is also possible to use each subdetector individually as is done for this analysis.

In order to maximize the η-acceptance of the analysis, only the SPD as the innermost detector with the largest longitudinal coverage is used. The SPD is itself comprised of two separate layers. The coverage of the inner (outer) layer is $|\eta| < 2.0$ ($|\eta| < 1.4$) respectively. The SPD's close proximity to the IP make it ALICE's most important vertex detector. Its fast clock-cycle of 10 MHz also allows it to be used for triggering purposes. Given its close proximity to the IP, the SPD is designed to operated in high track densities of up to $50\,\text{tracks/cm}^2$. The necessary resolution as well as radiation resistance is provided by 9.8 million cells which are read out binary, i.e., if the signal from the cell surpasses a given threshold the cell is regarded as hit. Each cell measures $50\,\mu\text{m} \times 425\,\mu\text{m}$ in $r\varphi$ and z respectively. If a particle traverses both layers of the SPD,

Table 6.1: Summary of individual FMD subsystems. Numbers taken from [39].

Name	Azimuthal sectors	z [cm]	r [cm]	η coverage	φ resolution
FMD1	20	320	4.2–17.2	$[3.68, 5.03]$	18°
FMD2i	20	83.4	4.2–17.2	$[2.28, 3.68]$	18°
FMD2o	40	75.2	15.4–28.4	$[1.70, 2.29]$	9°
FMD3i	20	−75.2	4.2–17.2	$[-2.29, -1.70]$	18°
FMD3o	40	−83.4	15.4–28.4	$[-3.40, -2.01]$	9°

it is likely to create a signal in one or two neighboring cells in each layer. A pair of such clusters in the inner and outer layer are referred to as a *tracklet*. The primary vertex of a collision is found by first computing all possible tracklets and subsequently finding the point which has the smallest distance to all tracklets. That point is then the most likely primary vertex position. Once the primary vertex position is established a refitting of the tracklets, taking the primary vertex position into account is conducted [38]. The tracklets found from this second procedure are then available for the subsequent analysis.

6.2.2 Forward multiplicity detector

The FMD is used to measure the particle multiplicities in the forward and backward regions and its location with respect to the other detectors of this analysis is depicted in Fig. 6.2. Similarly to the ITS the FMD is divided into three subsystems: FMD1, FMD2, and FMD3. All subsystems are silicon strip detectors arranged in five rings with their surface areas oriented perpendicular with respect to the beam pipe providing a total of 51200 channels. The FMD's primary purpose is to provide a large and high resolution η-acceptance in the regions not covered by the central barrel. Furthermore, its φ solution was chosen with anisotropic flow measurements in mind making this detector the natural choice for this analysis.

Depending on their distance from the beam pipe the five rings are divided into *inner* (i) and *outer* (o) rings whose properties are summarized in Tab. 6.1. The number of azimuthal segments is the limiting factor for the φ resolution of the detector. Notably, the FMD was not designed as a trigger detector which is reflected in its long integration time of $\approx 2\,\mu s$ which makes this detector susceptible to the pile-up effects discussed in Sec. 8.1. A very detailed description of the FMD may be found in Refs. [39, 40].

6.2.3 VZERO

The VZERO detector is comprised of two ring-shaped scintillator arrays on either side of the IP which cover approximately the same η-region as the FMD, i.e., $-3.7 < \eta < -1.7$ (V0C) and $2.8 < \eta < 5.1$ (V0A). It was primarily designed to act as an online multiplicity trigger, but can also be used for other purposes such as centrality and event-plane estimation or beam-induced background rejection[41]. The timing characteristics

Table 6.2: Summary of the two VZERO subsystems VZERO-A and VZERO-C. Numbers taken from [41].

Name	Azimuthal sectors	Radial sectors	z [cm]	r [cm]	η coverage	φ resolution
V0A	8	4	329	$[4.3, 41.2]$	$[2.8, 5.1]$	45.0°
V0C	8	4	$[-88, -86]$[1]	$[4.5, 32.0]$	$[-3.7, -1.7]$	45.0°

(≈ 0.6 ns) of the VZERO are significantly better than those of the FMD but not sufficient to locate the vertex position or as a timing detector [37].

The two rings of the VZERO - V0A and V0C - are located asymmetrically around the IP and their properties are summarized in Tab. 6.2. The signal produced by the scintillator tiles of the VZERO is related by a monotonic function to the number of particles traversing the detector. The detector can therefore be used to estimate the centrality of a Pb–Pb collision since the number of produced particles is strongly correlated with the impact parameter of the collision. While the VZERO could technically also be used for analyses of the produced particle densities, its large segmentation make its use for anisotropic flow measurements difficult [42]. This analysis uses the VZERO as a trigger and to identify out-of-bunch pile-up events in the FMD as described in Sec. 8.1.

6.2.4 Multiplicity and centrality estimation

The impact parameter b of a HI collision is defined as the distance between the two geometric centers of the colliding nuclei. Head-on (central) collisions therefore have an impact parameter of $b = 0$ and the overlap region between the nuclei is maximal. With a decreasing overlap region the number of nucleons *participating* in the collision (N_{part}) also decreases; a process which is commonly simulated using MC Glauber simulations. The multiplicity N_{ch} produced in a collision increases monotonically as a function of N_{part}. While neither b nor N_{part} cannot be directly measured, N_{ch} is easily accessible. The centrality of Pb–Pb collisions is therefore commonly estimated by measuring N_{ch} and relying on the strong correlation between N_{ch}, N_{part}, and b. These correlations extend over a large range in η such that the number of charged particles can either be measured in the central, or in the forward/backward region of the detector. A given event is classified in terms of its multiplicity and therefore centrality with respect to the entire event sample. Commonly, the relation to the event sample is expressed in terms of the accumulated percentile points of events with a multiplicity larger than the given event. Therefore, 0% denotes the most central and 100% the most peripheral events.

In ALICE the most commonly used detector for centrality estimation is the V0. However, due to its z_{vtx} dependent η-overlap with the FMD it was not used for that purpose in this analysis. Instead the centrality was estimated using the number of clusters in the inner most layer of the SPD (CL0).

[1] The radial segments are slightly displaced in z.

Chapter 7

Experimental considerations

The measurement of $\hat{V}_{n,-n}(\eta_a, \eta_b)$ and the corresponding factorization ratios bear various experimental complications. The material budget of the ALICE detector in the forward and backward region is not precisely known, thus making corrections based on MC simulations difficult for the FMD. Therefore, it is desirable to construct observables which are as independent of detector effects as possible. The reduced two-particle density $r_2(\eta_a, \eta_b, \varphi_a, \varphi_b)$ is such a quantity and its robustness against uncorrelated detector effects is discussed in Sec. 7.1. A further complication arises from the highly non-uniform acceptance regions in (η, φ) of the detectors involved. This can be partly overcome by exploiting the symmetries of the averaged two-particle distributions before computing $\hat{V}_{n,-n}(\eta_a, \eta_b)$ as discussed in Sec. 7.2. A residual detector effect present in $\hat{V}_{n,-n}(\eta_a, \eta_b)$ is caused by secondary particles from material interactions. In Sec. 7.3 the effects of such secondary particles is discussed. The implementation of the factorization procedure and the propagation of statistical uncertainties through the entire analysis is discussed subsequently in Sec. 7.4 and Sec. 7.5. Lastly, the assumptions made with regard to the robustness of this analysis are verified in a MC-closure test in Sec. 7.6.

7.1 Uncorrelated detector efficiencies

Generally, the number of particles observed in a detector might not necessarily correspond to the number of primary particles produces in the collision. Reasons for this discrepancy may be a finite probability to successfully detect and reconstruct a particle traversing a detector, which decreases the number of observed particles. However, the number of detected particles may also increase due to detector effects. In the case of the FMD, every primary particle produces on average more than two secondary particles which may also be detected but cannot be differentiated from primary particles. The effects caused by secondary particles from material interactions are primarily dependent on the detector geometry and are constant throughout the data taking period. Furthermore, they can be assumed to affect each primary particle individually. The number of observed particles N^{obs} is then understood as the product of the *true* number of primary particles N^{truth} times a detector dependent factor ϵ. For detectors with p_{T} resolution,

the density of observed particles can therefore be expressed by

$$\left\langle \frac{d^3N^{\text{obs}}}{d\eta d\varphi dp_{\text{T}}} \right\rangle = \epsilon(\eta, \varphi, p_{\text{T}}) \left\langle \frac{d^3N^{\text{truth}}}{d\eta d\varphi dp_{\text{T}}} \right\rangle \tag{7.1}$$

where ϵ is constant for all events.

However, since neither the FMD nor the SPD resolve in p_{T} the approximation is made that the effect of the p_{T} dependence is small when forming the average. This allows the (η, φ) dependent particle density to be written as

$$\hat{\rho}_1^{\text{obs}}(\eta, \varphi) = \left\langle \frac{d^2N^{\text{obs}}}{d\eta d\varphi} \right\rangle \approx \epsilon'(\eta, \varphi)\hat{\rho}_1^{\text{truth}}(\eta, \varphi) \tag{7.2}$$

where $\epsilon'(\eta, \varphi)$ is a modified efficiency after averaging over p_{T}. The quantities $\hat{\rho}_1^{\text{obs}}$ and $\hat{\rho}_1^{\text{truth}}$ are the single particle distributions as defined in Eq. (3.1). In Sec. 4.2.1 it was shown that single-particle distributions, averaged over the event sample, have no azimuthal anisotropies. Thus, all observed anisotropies must originate from detector effects and one may rewrite Eq. (7.2) as

$$\hat{\rho}_1^{\text{obs}}(\eta, \varphi) \approx \epsilon'(\eta, \varphi)\hat{\rho}_1^{\text{truth}\prime}(\eta) \tag{7.3}$$

where $\hat{\rho}_1^{\text{truth}\prime}$ emphasizes the φ-independence of the averaged single-particle distribution.

The same approximation with respect to the p_{T}-dependence may also be performed for the two-particle density

$$\hat{\rho}_2^{\text{obs}}(\eta_a, \eta_b, \varphi_a, \varphi_b) \approx \epsilon(\eta_a, \varphi_a)\epsilon(\eta_b, \varphi_b)\hat{\rho}_2^{\text{truth}}(\eta_a, \eta_b, \varphi_a\varphi_b) \tag{7.4}$$

From Eq. (7.3) and Eq. (7.4) it is apparent that the former can be used to cancel out the detector effects in the latter without altering the azimuthal dependencies of the two-particle distribution. Plugging Eq. (7.2) and Eq. (7.4) into the definition of the reduced two particle density r_2 from Eq. (3.3) yields

$$r_2(\eta_a, \eta_b, \varphi_a, \varphi_b) = \frac{\hat{\rho}_2^{\text{obs}}(\eta_a, \eta_b, \varphi_a, \varphi_b)}{\hat{\rho}_1^{\text{obs}}(\eta_a, \varphi_a)\hat{\rho}_1^{\text{obs}}(\eta_b, \varphi_b)} \tag{7.5}$$

$$= \frac{\epsilon(\eta_a, \varphi_a)\epsilon(\eta_b, \varphi_b)\hat{\rho}_2^{\text{truth}}(\eta_a, \eta_b, \varphi_a, \varphi_b)}{\epsilon(\eta_a, \varphi_a)\epsilon(\eta_b, \varphi_b)\hat{\rho}_1^{\text{truth}}(\eta_a)\hat{\rho}_1^{\text{truth}}(\eta_b)} \tag{7.6}$$

$$= \frac{\hat{\rho}_2^{\text{truth}}(\eta_a, \eta_b, \varphi_a, \varphi_b)}{\hat{\rho}_1^{\text{truth}}(\eta_a)\hat{\rho}_1^{\text{truth}}(\eta_b)} \tag{7.7}$$

In Eq. (7.7), all efficiencies cancel out, making r_2 robust with respect to uncorrelated detector effects. Therefore, r_2 can be used to compute $\hat{V}_{n,-n}(\eta_a, \eta_b)$.

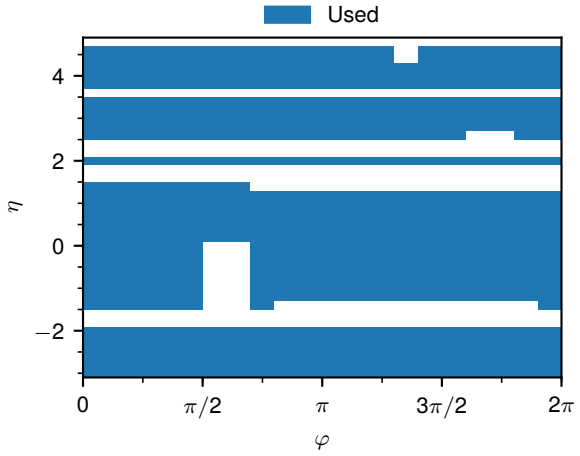

Figure 7.1: Detector acceptance in (η, φ) for $0 < z_{\text{vtx}} < 0.5\,\text{cm}$. White areas represent excluded regions (see text).

Limitations to the robustness of r_2

It is important to address the limitations of the robustness of r_2 in the context of this analysis. While Eq. (7.7) holds true analytically, $\hat{\rho}_1^{\text{obs}}$ and $\hat{\rho}_2^{\text{obs}}$ are measured in finite bins of η, φ, and also z_{vtx}. If the efficiency varies significantly within a bin it is not justifiable to move $\epsilon(\eta, \varphi)$ out of the average in Eq. (7.2). However, if that approximation is not applicable, the efficiencies will not cancel out in Eq. (7.7). It is therefore important for this analysis to exclude any histogram bins over which the efficiency can not be assumed as approximately constant.

7.2 Non-uniform acceptance and Fourier decomposition

While both, the FMD and the SPD were designed to have a full 2π coverage, both detectors exhibit gaps within their acceptance. Depending on the reconstructed vertex position, these gaps appear at different positions, which makes the acceptance z_{vtx}-dependent. Histogram bins which partly overlap with an inactive region of the detector in η, φ, or z_{vtx} are removed from the analysis. In order to not exclude more regions of the phase-space than necessary, the analysis is performed in narrow z_{vtx} bins of 0.5 cm width. The resulting acceptance map for $0\,\text{cm} < z_{\text{vtx}} < 0.5\,\text{cm}$ is shown in Fig. 7.1.

The gaps in the acceptance inevitably lead to some bins of $r_2(\eta_a, \eta_b, \varphi_a, \varphi_b)$ having an incomplete φ coverage for either one or both particles. Fig. 7.2 shows the (φ_a, φ_b)-plane of r_2 at $\eta_a = 0$ and $\eta_b = 4$ where particle a exhibits a gap in its φ acceptance. Such gaps in the (φ_a, φ_b)-plane make an efficient two-dimensional Fast Fourier Transform (FFT) impossible and a two-dimensional fit to a Fourier series unstable. In order to extract $\hat{V}_{n,-n}(\eta_a, \eta_b)$ from regions with acceptance gaps in φ, the symmetries of r_2 along the diagonal of the (φ_a, φ_b)-plane are exploited as described in Sec. 4.4.3. The transformation

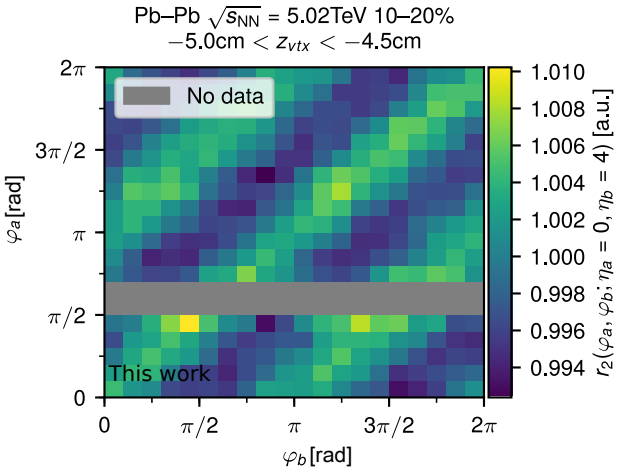

Figure 7.2: Normalized two-particle density r_2 in the (φ_a, φ_b)-plane in $-5.0\,\text{cm} \leq z_{\text{vtx}} < -4.5\,\text{cm}$ and $10-20\%$ centrality. Particle pairs are formed from the same phase space as in Fig. 9.5 except of the z_{vtx} position. Particle a exhibits an acceptance gap in the φ.

$(\varphi^a, \varphi^b) \to (\Delta\varphi, \widetilde{\varphi})$ has a Jacobian of 1 and therefore $r_2(\eta_a, \eta_b, \varphi_a, \varphi_b)$ can be trivially transformed to the new coordinate system:

$$r_2(\eta_a, \eta_b, \varphi_a, \varphi_b) \to r_2'(\eta_a, \eta_b, \Delta\varphi, \widetilde{\varphi}) \tag{7.8}$$

Since $r_2'(\eta_a, \eta_b, \Delta\varphi, \widetilde{\varphi})$ does not depend on $\widetilde{\varphi}$ one may perform an average along that coordinate without loss of generality

$$r_2''(\eta_a, \eta_b, \Delta\varphi) = \left\langle r_2'(\eta_a, \eta_b, \Delta\varphi, \widetilde{\varphi}) \right\rangle_{\widetilde{\varphi}} \tag{7.9}$$

Acceptance gaps can be taken into account when forming the average such that $r_2''(\eta_a, \eta_b, \Delta\varphi)$ is defined in every bin of $\Delta\varphi$.

It is important to note here that the uncorrected $\hat{\rho}_2$ is not constant along $\widetilde{\varphi}$ since detector effects depend on absolute values of φ and thus remain after averaging over the event sample. Therefore, r_2'' cannot be calculated as

$$r_2''(\eta_a, \eta_b, \Delta\varphi) \neq \frac{\left\langle \hat{\rho}_2^{\text{obs}\prime}(\eta_a, \eta_b, \Delta\varphi, \widetilde{\varphi}) \right\rangle_{\widetilde{\varphi}}}{\left\langle \hat{\rho}_1^{\text{obs}}(\eta_a, \varphi_a) \hat{\rho}_1^{\text{obs}}(\eta_b, \varphi_b) \right\rangle_{d\widetilde{\varphi}}} \tag{7.10}$$

A more detailed study of the effects introduced when performing the normalization according to Eq. (7.10) is provided in Ref. [43].

7.2.1 Fourier transformation

The Fourier coefficients $\hat{V}_{n,-n}(\eta_a, \eta_b)$ are computed from $r_2''(\eta_a, \eta_b, \Delta\varphi)$ in the $\Delta\varphi$ dimension. The procedure has to be performed in every bin of the (η_a, η_b)-plane, for each z_{vtx}-bin, and for each centrality bin separately. Furthermore, errors are propagated with

a bootstrapping method (see Sec. 7.5) requiring the analysis to be repeated hundreds of times. For the binning chosen in this analysis, this results in approximately ~ 1 million separate Fourier transformations. A Fourier decomposition may be performed very efficiently using a FFT: a numerical, deterministic algorithm which is a standard tool in most scientific libraries [44, 45]. While an ordinary least square fit would perform at best with complexity $O(n(\log_2 n)^2)$ [46], a FFT can be performed at $O(\frac{n}{2}\log n)$ [47] where n is the number of bins in the $\Delta\varphi$ dimension. For the 20 bins used in this analysis, the FFT is approximately one order of magnitude faster than the least square procedure. The FFT yields the complex Fourier coefficients for the frequencies from $-n/2$ up to $n/2$.

7.3 Secondary particles from material interactions

In Sec. 7.1 it was shown that $r_2''(\eta_a, \eta_b, \Delta\varphi)$ is a robust observable with respect to uncorrelated detector efficiencies. Thus, no further corrections to r_2'' are required in that respect. However, in addition to uncorrelated detection efficiencies, correlated detector effects are also present in the observed quantities.

7.3.1 Secondary particles from detector material interaction

Whenever a particle traverses detector material it has a finite chance to interact. This interaction may be an absorption, a deflection, or a creation of a secondary particle. The secondary particle will be strongly correlated to the initial momentum of the incident particle. This correlation will be present in the observed particle-pair density if both particles are subsequently detected. Furthermore, a deflection from the azimuthal direction of the primary particle causes a decorrelation effect with respect to an underlying flow-signal. If the deployed detectors have tracking capabilities it is possible to reconstruct the vertex where the secondary particle has been created and thus disregard it in the subsequent analysis. The SPD-tracklets are refitted to the event's vertex position, thus decreasing the effect of secondary particles. However, the FMD has no tracking capabilities making it impossible to differentiate primary and secondary particles in the analysis.

Based on MC simulations, Fig. 7.3 depicts the origin of secondary particles which were subsequently detected by the FMD as a function of z_{vtx} and distance from the beam axis r. The ITS subdetectors and support structure along with the beam pipe are found to contribute a large number of secondary particles to the multiplicity observed in the FMD.

To better understand the origin of the observed multiplicities as a function of η Fig. 7.4 depicts the number of charged particles traversing active regions of the ITS and the FMD for collisions within $-2\,\text{cm} \leq z_{\text{vtx}} \leq 2\,\text{cm}$. The simulation was performed on Pb–Pb collisions at $\sqrt{s_{\text{NN}}} = 2.76\,\text{TeV}$ but the energy dependence of the number of secondary particles produced per primary particle is expected to be small. The different colors denote in which part of the detector the secondary particles were created. Evi-

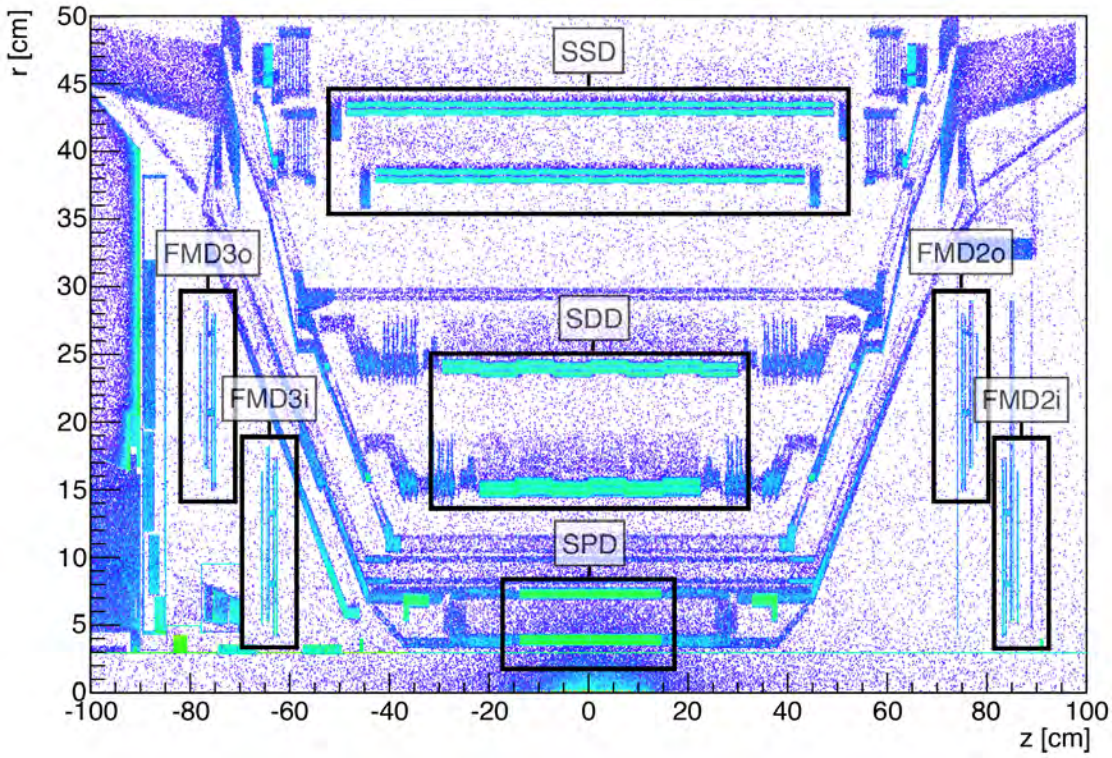

Figure 7.3: Origin of secondary particles created by material interactions. The active detector elements of the ITS, its support structure as well as the four inner rings of the FMD are clearly visible. Figure taken from [48].

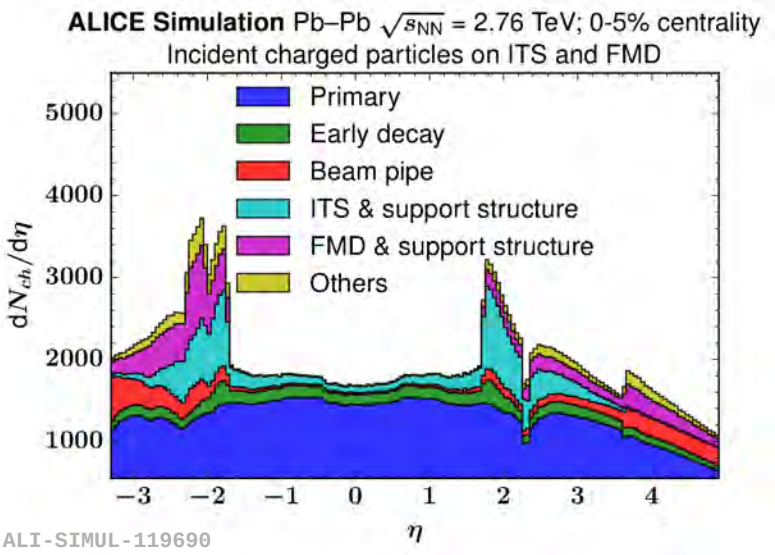

Figure 7.4: Origin of particles traversing the FMD or ITS. The FMD exhibits a large number of secondary particles compared to primary particles. The number of observed secondary particles depends strongly on the pseudorapidity η. The simulation was conducted for Pb–Pb collisions at 2.76 TeV within $-2\,\mathrm{cm} \leq z_{\mathrm{vtx}} \leq 2\,\mathrm{cm}$.

dently, the SPD experiences a much smaller and more homogeneous flux of secondary particles compared to the FMD where the number of secondary particles is in parts more than 3 times larger to the number of detected primary particles. The origin of the secondary particles exhibits a strong η dependence.

$\Delta\varphi$ between two primary particles

The effect of secondary particles on the measured angular distance between a pair of primary particles is schematically shown in Fig. 7.5. The two primary particles were produced in the collision at φ_a and φ_b. In the absence of detector effects, the difference for this pair is well defined as $\Delta\varphi = \varphi_a - \varphi_b$. However, if one or both particles are deflected or produce correlated secondary particles, it *blurs* the $\Delta\varphi$ distribution as well. This effect can be described in terms of a blurring function $f(\eta, \varphi)$ which is *convolved*[1] along the azimuth with the distribution of primary particles. The observable two-particle probability distribution is then given by

$$P_2^{\mathrm{obs}}(\eta_a, \eta_b, \varphi_a, \varphi_b) = f(\varphi_a) * f(\varphi_b) * P_2^{\mathrm{truth}}(\eta_a, \eta_b, \varphi_a, \varphi_b) \tag{7.11}$$

where $*$ denotes a convolution. Convolutions are multiplications in Fourier space, making Eq. (7.11) easier to work with after applying the Fourier transformations along the

[1] A short summary of the most important properties of convolutions is given in Appendix C.2

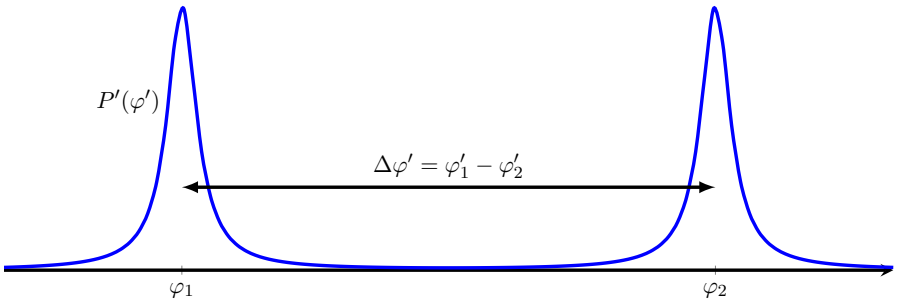

Figure 7.5: Schematic of how secondary particles decorrelated the azimuthal differences of two underlying primary particles created at φ_1 and φ_2.

azimuthal dimensions (denoted by $\mathcal{F}_a$ and $\mathcal{F}_b$).

$$V^{\text{obs}}_{n,m}(\eta_a, \eta_b) = \mathcal{F}_a \left[\mathcal{F}_b \left[P_2^{\text{obs}}(\varphi_a, \varphi_b, \eta_a, \eta_b) \right] \right] \tag{7.12}$$

$$= \left(\frac{1}{2\pi} \right)^2 \cdot \mathcal{F}_a[f(\varphi_a)] \cdot \mathcal{F}_b[f(\varphi_b)] \cdot \mathcal{F}_a \left[\mathcal{F}_b \left[P_2^{\text{truth}}(\varphi_a, \varphi_b, \eta_a, \eta_b) \right] \right] \tag{7.13}$$

$$= \zeta_n(\eta_a) \cdot \zeta_m(\eta_b) \cdot V_{n,m}(\eta_a, \eta_b) \tag{7.14}$$

The Fourier transform of the blurring functions (scaled by $1/2\pi$) $\zeta_n(\eta_a)$ and $\zeta_n(\eta_b)$ act as η dependent scaling factor of the Fourier coefficients. The described blurring effect is dominated by secondary particles from material interactions and is therefore a property of the detector which is independent of the event-by-event fluctuations of $V_{n,m}(\eta_a, \eta_b)$. The averaged Fourier coefficients can therefore be written as

$$\hat{V}_{n,-n}(\eta_a, \eta_b) = \zeta_n(\eta_a) \cdot \zeta_m(\eta_b) \cdot \left\langle V^{\text{truth}}_{n,n}(\eta_a, \eta_b) \right\rangle \tag{7.15}$$

which shows that the blurring of the azimuthal dimensions of the two-particle distribution does not affect their factorizability in the (η_a, η_b)-plane. When the factorization is performed, $\zeta_n(\eta)$ is implicitly combined with the flow coefficients

$$v_n^{\text{obs}}(\eta) = \zeta_n(\eta) v_n^{\text{truth}}(\eta) \tag{7.16}$$

This holds true for both Model A, and Model B. For the factorization ratio defined in Eq. (3.11), $\zeta_n(\eta)$ cancels out completely.

Furthermore, Eq. (7.15) shows that analyses which seek to measure corrected flow coefficients should apply a correction for secondary particles in Fourier space [30].

Correlations between primary and secondary particles

The observed two-particle distribution also contains pairs between secondary particles and their respective primary mothers. Such pairs are expected to be strongly correlated and in short azimuthal and longitudinal distance of each other. Eq. (7.11) does not apply to correlated pairs and thus the effect of such pairs is not expected to cancel out when forming the factorization ratio $f_n(\eta_a, \eta_b)$.

7.3.2 Detector segmentation

The effects of the detector segmentation on the Fourier coefficients $\hat{V}_{n,-n}$ is conceptually very similar to that of independent secondary particles. The finite width of a detector element can be viewed as a finite detector resolution which acts as a filter function on the particle distributions. Instead of detecting a particle with its precise azimuth φ, a detector consisting of N segments can only resolve a hit within the azimuthal width $\delta\varphi = 2\pi/N$ of one element. The filter function is therefore a rectangular function $\texttt{rect}(\varphi/\delta\varphi)$ of width $\delta\varphi$. The observable single-particle probability distribution is thus given by

$$P_1^{\text{obs}}(\varphi) = \texttt{rect}\left(\frac{\varphi}{\delta\varphi}\right) * P_1^{\text{truth}}(\varphi) \tag{7.17}$$

The Fourier transformation of Eq. (7.17) is given by

$$\mathcal{F}(P_1^{\text{obs}}(\varphi)) = \mathcal{F}\left[\texttt{rect}\left(\frac{1}{\delta\varphi}\varphi\right)\right] \cdot \mathcal{F}\left[P_1^{\text{truth}}(\varphi)\right] \tag{7.18}$$

$$= |\delta\varphi|\texttt{sinc}\left(\frac{n\delta\varphi}{2\pi}\right) \cdot \mathcal{F}\left[P_1^{\text{truth}}(\varphi)\right] \tag{7.19}$$

$$= |\delta\varphi|\texttt{sinc}\left(\frac{n}{N}\right) \cdot \mathcal{F}\left[P_1^{\text{truth}}(\varphi)\right] \tag{7.20}$$

where $\texttt{sinc}(x)$ is defined as $\frac{\sin(\pi x)}{\pi x}$.

This derivation assumes that P_1^{truth} has no modes above the sampling frequency of $N/2$ where N is the number of detector elements in the azimuth. This result is in agreement with a more general derivation found in Ref. [42].

The FMD has a minimal segmentation of $N = 20$. Thus, the detector segmentation reduces the observed $\hat{V}_{n,-n}$ by 3.2% if both particles are within the FMD acceptance. However, the segmentation affects each particle independently and therefore does not affect the factorization ratio.

7.4 Factorization procedure

Model A and Model B described in Sec. 3.3 are both non-linear equation systems. The solution of the equation system is complicated by various factors:

- Neither model includes a description of the non-flow contribution in $\Delta\eta \lesssim 2$
- Each point in $\hat{V}_{n,-n}(\eta_a, \eta_b)$ has an associated statistical uncertainty $\sigma_{n,-n}(\eta_a, \eta_b)$
- The acceptance in the (η_a, η_b)-plane exhibits large gaps
- $v_n(\eta)$ dependents on z_{vtx} (due to secondary particles) whereas F_n^η does not. It is desirable to find the best fit $v_n(\eta)$ per z_{vtx}-bin, but one common F_n^η for the entire z_{vtx}-acceptance.

The approach taken in this analysis is a weighted least-square-optimization which accommodates all of the above points. Using the bin-index notation from Sec. 3.3, the weighted sum of squares S is given by

$$S = \sum_{i,j=1}^{N_a,N_b} \left(\frac{\hat{V}_{n,-n}(\eta_a^i, \eta_b^j) - M(\eta_a^i, \eta_b^j)}{\sigma_{n,-n}(\eta_a^i, \eta_b^j)} \right)^2 \tag{7.21}$$

where N_a (N_b) is the number of bins in η_a (η_b) and M represents either Model A or Model B. Points outside of the acceptance in the (η_a, η_b)-plane or pairs with a $|\Delta\eta|$ separation of less than $\Delta\eta_{\min}$ can be removed from the sum. The best fit of the chosen model is found by minimizing S with respect to the parameters of the model; namely the values of $v_n(\eta^i)$ and additionally F_n^η in case of Model B.

7.5 Error propagation

An analytical description of the error-propagation through the Fourier Transformation and the non-linear fits in the optimization procedure is complicated. Instead, a bootstrapping-like scheme is chosen to propagate the statistical uncertainties from $r_2(\eta_a, \eta_b, \varphi_a, \varphi_b)$ to the desired observable. The procedure is as follows:

1. A new *sample* $r_2^{boot}(\eta_a, \eta_b, \varphi_a, \varphi_b)$ is created by randomly varying each point in $r_2(\eta_a, \eta_b, \varphi_a, \varphi_b)$ by a Gaussian distribution with a width according to the statistical uncertainty of each point
2. The full analysis is performed on r_2^{boot} yielding the desired final observable $(\hat{V}_{n,-n}(\eta_a, \eta_b),\ F_2^\eta,\ f(\Delta\eta),\ \dots)$
3. The result of the sample is recorded
4. Step 1–3 is repeated approximately 100 times
5. The variance between the recorded results is used as an estimate of the statistical uncertainty

While numerically expensive, this procedure provides a good approximation of the final statistical uncertainties.

7.6 Monte Carlo closure test

In the previous sections of this chapter it was argued that the factorization ratio given by Eq. (3.11) is robust with respect to detector effects and requires no further correction, with an exception for short-range pairs between hits in the FMD. This section presents a MC-closure test to confirm the previously made assumptions. Such a test is based on two simulated data sets: One which includes only the charged primary particles of the collision (*truth*) and one which uses the same simulated events but also includes

a simulation of the detector response (*reconstructed*). The reconstructed event sample only includes events which fulfilled all event and tracklet selection requirements otherwise applied to the measured data. If the assumptions made concerning the robustness of r_2 and the understanding of the effect of secondary particles is correct, one expects the factorization ratios of both data sets to be identical. Using a simulated data set with a flow signal[2] and a simulated detector response it is possible to test this expectation. The factorization ratio is computed for the truth and the reconstructed sample and compared in a ratio

$$\text{Closure} = \frac{f_n^{\text{rec}}(\eta_a, \eta_b)}{f_n^{\text{truth}}(\eta_a, \eta_b)} \tag{7.22}$$

Fig. 7.6 shows the result of the MC-closure test in the (η_a, η_b)-plane along with the associated relative uncertainties of each bin. A visual aid for the different detector combinations encountered in the (η_a, η_b)-plane is provided in Fig. 7.7. Due to poor statistics in the given data set, the centrality bin had to be chosen to span the large interval of $10 - 60\%$. The factorization was performed on pairs of particles with $|\Delta\eta| > 2$ using Model A. As expected, the ratio is approximately 1 for most regions of the phase space, even for points well within $\Delta\eta < 2$ - the region excluded during the fit. Most notably, the ratio deviates from unity in the short range region of the FMD due to correlated pairs of secondary particles from material interaction. These particles break the factorization assumption and are only present in the reconstructed sample. Therefore, the reconstructed and the MC-truth sample deviate from each other for short-range pairs of hits in the FMD.

In order to asses which points of Fig. 7.6 (top) are compatible with unity within their uncertainties, it is helpful to plot the residuals of each point. The residual R of a point at (η_a, η_b) is defined as

$$R(\eta_a, \eta_b) = \frac{\text{Closure} - 1}{\sigma^{\text{closure}}(\eta_a, \eta_b)} \tag{7.23}$$

where σ^{closure} is the uncertainty at the respective point. The residual thus expresses deviations from the expected value in units of standard deviations. Fig. 7.8 depicts the residuals of the MC-closure test (top). The bottom plot in the same figure is based on the same data, but excludes all points within 2σ in order to make outliers more visible. The short-range non-closure in the FMD is significant with respect to the statistical uncertainties; as was expected. The remaining phase space is found to be in agreement with a successful MC-closure.

The small statistics and the large multiplicity binning make a MC-closure test with respect to F_2^η infeasible at this point. A larger MC production with anisotropic flow and a reconstructed detector response in the forward region is currently being prepared by the ALICE collaboration.

[2] LHC12a11g further described in Appendix B.4

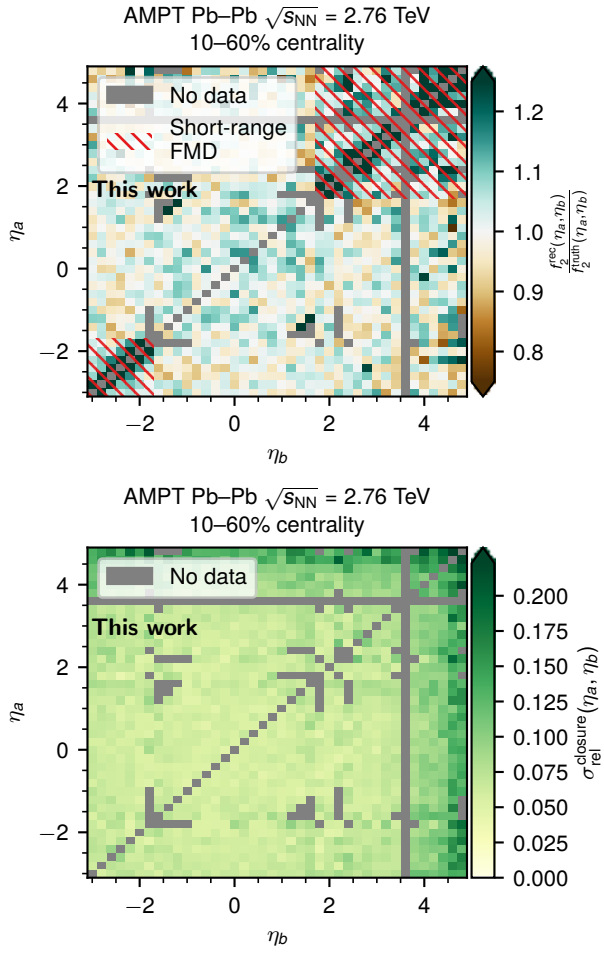

Figure 7.6: Top: MC-closure test for the factorization ratios base on Model A in the (η_a, η_b) plane. Bottom: Relative statistical uncertainties of the MC-closure test.

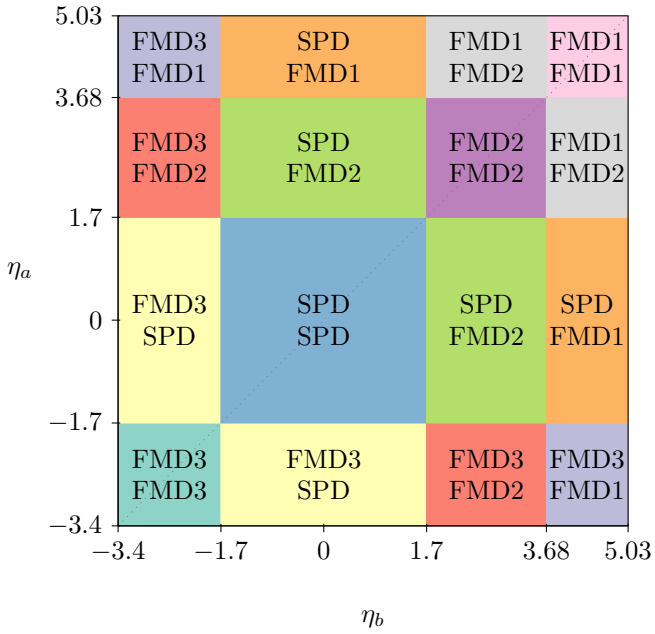

Figure 7.7: Schematic drawing of detector combinations in the (η_a, η_b)-plane.

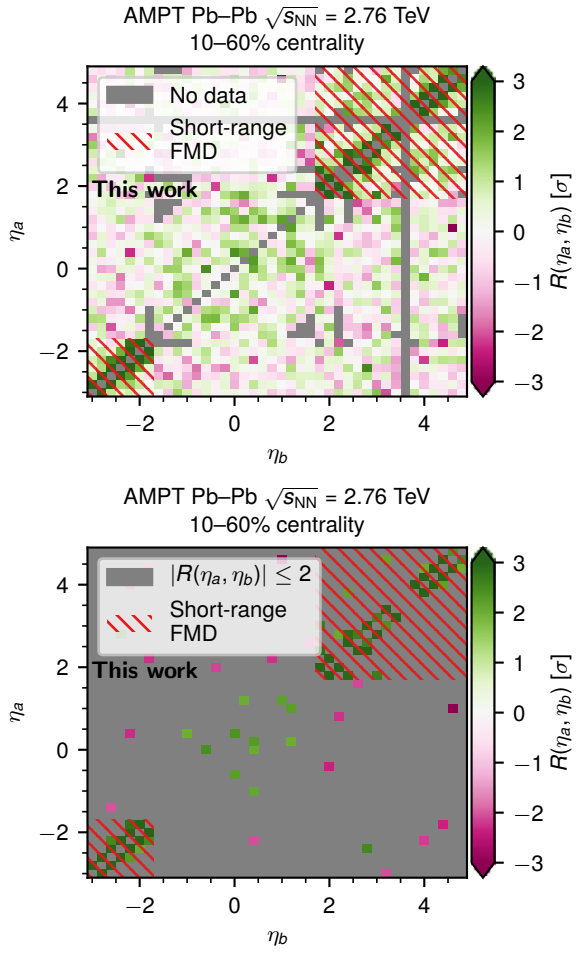

Figure 7.8: Top: Residuals of the MC closure test. Bottom: The same data as in the top panel, but all points within 2σ were removed.

Chapter 8

Event and tracklet selection

This chapter describes the event and tracklet selection performed on each individual event prior to using it in the analysis. While most of the deployed selection criteria are considered standard within the ALICE collaboration the FMD exhibits a particular susceptibility to out-of-bunch pile-up effects which required an additional cut using correlations between the FMD and the V0 detectors.

8.1 Event selection

Events used in this analysis fulfill all of the requirements below.

- The analysis was performed using a **minimum bias** trigger[1] which requires a coincidence in the V0A and V0C or a hit in either layer of the SPD.
- **Vertex selection**
  - A SPD-vertex was successfully reconstructed based on SPD tracklets
  - A TPC-vertex was successfully reconstructed based on TPC tracks
  - The SPD and the TPC-vertex are compatible within their uncertainties
  - The resolution of SPD-vertex is better than 0.25 cm
  - The primary vertex was is located within $-5\,\mathrm{cm} < z_{\mathrm{vtx}} < 6\,\mathrm{cm}$. The asymmetric interval was chosen due to an offset of the mean z_{vtx}-position
- Events with more than one reconstructed primary vertex were identified as **multi-vertex pile-up** and discarded
- **DAQ readout** was complete
- **FMD** was read out successfully

[1] Referred to as kINT7 within the ALICE collaboration

- **SPD background** events were rejected. Background events exhibit a large number of clusters in the SPD (N_{cl}) compared to the number of reconstructed tracklets N_{tr}. Events are considered as background if $N_{\mathrm{cl}} > 65 + 4N_{\mathrm{tr}}$
- **FMD-V0** correlations were used to discard out-of-bunch pile-up as described in Sec. 8.1.1

Due to technical issues at the time of the data collection, the FMD was only included in late stages of each fill of the LHC when the luminosity had decreased significantly. The most restrictive criteria was therefore the availability of the FMD. The second most restrictive criteria was the minimum bias trigger. Out of the initial 36 million events, 8.4 million were selected for the analysis.

8.1.1 Out-of-bunch pile-up

The FMD's long integration time of 2 µs make it susceptible to additional out-of-bunch pile-up and beam-halo effects (particles traveling parallel to the beam). The cut to discard such events is based on the overlap of the slow FMD with the fast V0 detector in pseudorapidity. In the absence of pile-up, the two detectors are highly correlated. Out-of-bunch pile-up events may cause a large multiplicity in the FMD while the V0 is unaffected due to its fast integration time. Thus, pile-up events can be identified as having an uncommonly large multiplicity in the FMD compared to the V0.

Fig. 8.1 displays the correlation between the FMD and the V0 detectors on either side of the interaction point after all other event selections were applied but before any cuts on the FMD-V0 correlation were performed. Out out-of-bunch pile-up events were removed if they met the following empirical criteria

$$A_{V0A} + A_{V0B} < 1.5(N_{FMD3} + N_{FMD1\&2}) \tag{8.1}$$

The correlations, after this cut was applied, are shown in Fig. 8.2. Even though this cut only removed a small number of events it proved crucial to this analysis. The high multiplicity events which are removed by this cut carry a large weight in the computed pair histograms since the number of pairs scales quadratic with the number of hits recorded by the FMD.

8.2 Tracklet selection

The tracklets used in this analysis are formed between one cluster in each SPD layer and the primary vertex. Based on these three points it is possible to compute an azimuthal bending $\Delta\varphi_{tr}$ which can be used as a tracklet selection criteria. A bending of $\Delta\varphi_{tr} < 5\,\mathrm{mrad}$ is required for each tracklet in order to minimize the contribution from secondary particles. This cut has been shown in MC simulations to also effectively impose a p_{T}-cut of $p_{\mathrm{T}} > 0.75\,\mathrm{GeV/c}$ on the selected tracks [49]. Since low momentum particles generally exhibit a smaller anisotropic flow, this cut is expected to increase the observed

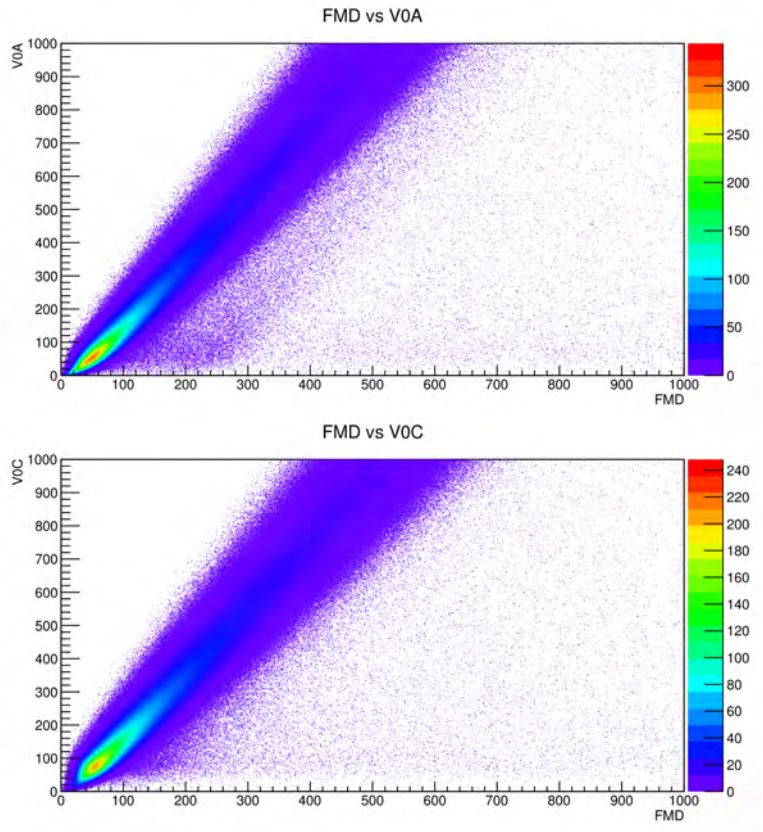

Figure 8.1: Correlation of the FMD3 multiplicity and the V0A amplitude (top) and the FMD1+FMD2 vs. V0C multiplicity (bottom) after all other event selection criteria were applied, except the cut on the FMD-V0 correlations. Out-of-bunch pile-up causes events with a large multiplicity in the FMD while the V0 detectors are able to resolve events separately.

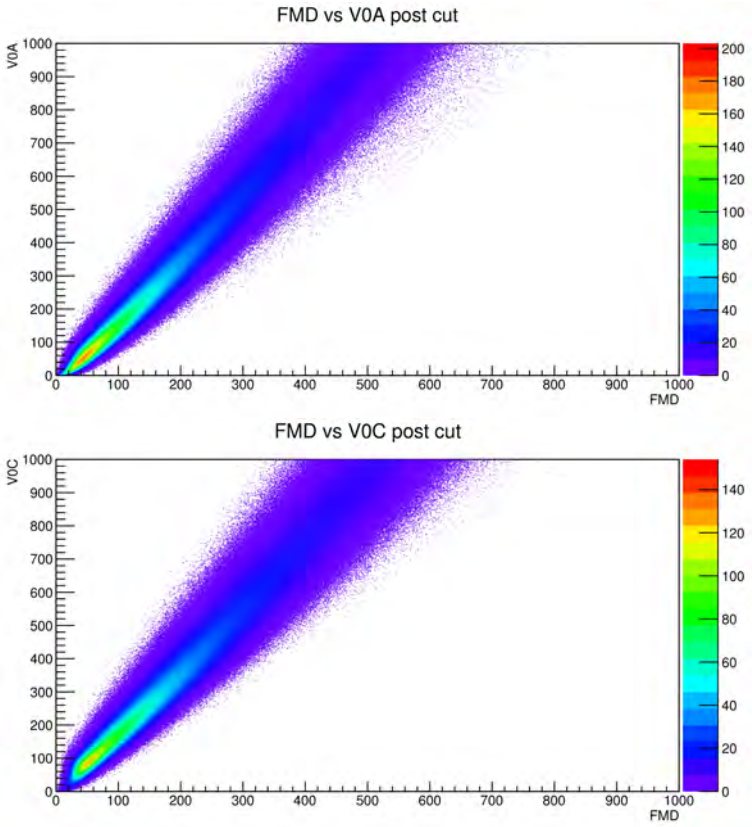

Figure 8.2: Correlation of the FMD3 multiplicity and the V0A amplitude (top) and the FMD1+FMD2 vs. V0C multiplicity (bottom) after all other event selection criteria were applied, including the cut on the FMD-V0 correlations.

$\hat{V}_{n,-n}(\eta_a, \eta_b)$ within the SPD acceptance. Furthermore, tracklets were required to be within $-1.7 < \eta < 1.7$ in order to avoid an overlap with the FMD across different z_{vtx} slices.

Chapter 9

Results

This section presents the results of this analysis at each step, starting from the particle distributions, to the computation of the Fourier coefficients and the final factorization. The single- and two-particle distributions are presented in various projections in Sec. 9.1 and Sec. 9.2. Subsequently, the reduced two-particle distribution, r_2, is formed and again presented in various projections in Sec. 9.3. The two-particle Fourier coefficients $\hat{V}_{n,-n}(\eta_a, \eta_b)$ are then computed from r_2 and presented in Sec. 9.4. The centrality and $|\Delta\eta|$-gap-dependence of the factorization with Model A is described in Sec. 9.5. The decorrelation parameter F_2^{η} of Model B is presented in Sec. 9.6. Lastly, the systematic uncertainties are discussed in Sec. 9.7.

All results in this section are for Pb–Pb collisions at a center of mass energy of $\sqrt{s_{\mathrm{NN}}} = 5.02\,\mathrm{TeV}$. The data set, which was recorded in 2015, is described in detail in Appendix B. A discussion of the results and a comparison to simulations is deferred to the Chapter 10.

9.1 Single-particle distributions

The single-particle distributions $\hat{\rho}_1(\eta, \varphi)$ are measured in 0.5 cm wide z_{vtx}-bins from $-5\,\mathrm{cm}$ to 6 cm as well as in centrality bins of varying size. The acceptance map, which excludes bins that overlap with inactive regions of the detectors as described in Sec. 7.2, was applied to all figures shown in the following.

$\hat{\rho}_1$ in the (η, z_{vtx})-plane

Fig. 9.1 presents the 0–5% centrality bin and is averaged over the φ-dimension; thereby reducing the histogram to the (η, z_{vtx})-plane. The color dimension denotes the average number of observed particles within the given bin and gray areas represent regions of the phase-space which are not covered by any active detector. The observed particle density is lower in the SPD region ($-1.7 \leq \eta \leq 1.7$) than in the FMD. This is due to the secondary particles from material interactions as discussed in Sec. 7.3.1. Furthermore, it is apparent that the acceptance of the involved detectors depends on the z_{vtx} position

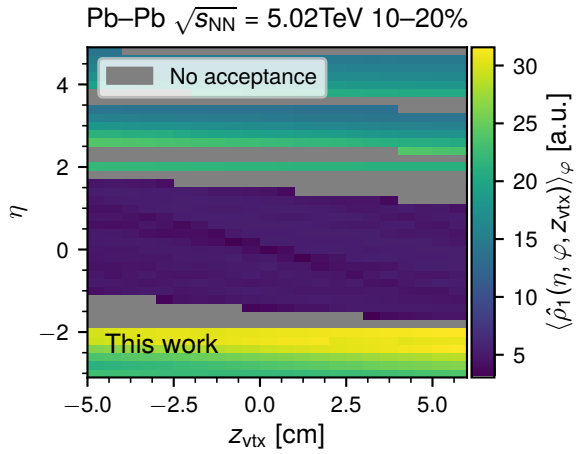

Figure 9.1: Single-particle distribution for Pb–Pb collisions at $\sqrt{s_{NN}} = 5.02\,\text{TeV}$ as a function of η and z_{vtx} averaged over φ. Each slice in z_{vtx} is normalized by the respective number of events in this bin. The distribution shows the dependence of the detector acceptance on these variables. The acceptance of the SPD exhibits a stronger dependence on z_{vtx} than the FMD. The forward and backward regions exhibit a large number of secondary particles from material interactions.

of the collision. This dependence is more significant for the central SPD than for the FMD.

$\hat{\rho}_1$ in the (η, φ)-plane

Fig. 9.2 presents the single-particle distribution in the (η, φ)-plane for $0\,\text{cm} \leq z_{\text{vtx}} < 0.5\,\text{cm}$. Both the SPD and the FMD exhibit a non-uniform acceptance and a φ-dependence. Based on the results of Sec. 4.2.1, any anisotropy in φ is due to detector effects.

9.2 Two-particle distributions

The two-particle distributions, $\hat{\rho}_2$, were measured as functions of $\eta_a, \eta_b, \varphi_a, \varphi_b$, centrality, and z_{vtx}. This large dimensionality makes the visual representation of the measured results challenging since numerous two-dimensional projections are possible. The following focuses on the (η_a, η_b)-plane and (φ_a, φ_b)-plane.

$\hat{\rho}_2$ in the (η_a, η_b)-plane

Fig. 9.3 shows a projection $\hat{\rho}_2$ onto the (η_a, η_b)-plane. The data in the figure is restricted to z_{vtx}-positions from 0 cm to 0.5 cm and the azimuthal coordinates were chosen as $\varphi_a = 0$ and $\varphi_b = 0$. The distribution is normalized such that it reflects the average number of pairs in any given bin. The different detector combinations[1] are easily distinguishable.

[1] See Fig. 7.7 for a visual guide to the various detector combinations covering the (η_a, η_b)-plane.

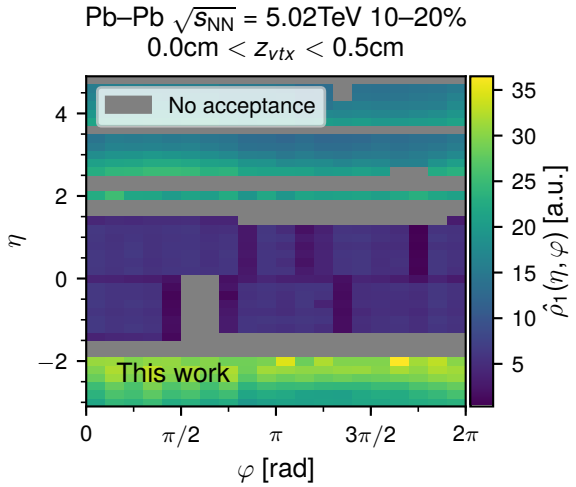

Figure 9.2: Single-particle distribution as a function of η and φ for primary vertex positions z_{vtx} from 0 cm to 0.5 cm in Pb–Pb collisions at $\sqrt{s_{NN}} = 5.02$ TeV. Bins which overlap with inactive detector regions were removed.

The FMD exhibits a large number of secondary particles from material interactions compared to the central region covered by the SPD. This causes the regions where both particles were detected in the FMD to have the largest number of pairs. Combination of the SPD and FMD exhibit significantly fewer pairs while the case of both particles being detected in the SPD is the least common. Depending on the z_{vtx} position, some regions of the phase space are not covered by the detector acceptance. This manifests itself in horizontal and vertical stripes in the (η_a, η_b)-plane. The areas outside of the detector acceptance in Fig. 9.3 correspond to the acceptance map presented in Fig. 7.1.

Note that the diagonal ($\eta_a = \eta_b$) is also excluded. This is due to the fact that the FMD is a hit based detector which provides the most likely number of particles per channel as a decimal number. This makes the definition of a pair ambiguous if a channel is paired with itself. However, this limitation is of no further consequence to this analysis. The phase-space of the two-particle distribution for $\eta_a \approx \eta_b$ is known to be dominated by non-flow effects and is excluded in the factorization procedure with a $|\Delta\eta|$-gap.

$\hat{\rho}_2$ in the (φ_a, φ_b)-plane

Fig. 9.4 shows $\hat{\rho}_2$ as a function of (φ_a, φ_b) where the first particle was chosen from the central region ($\eta_a = 0$) and the second particle from the forward region ($\eta_b = 4$). The distribution is normalized to represent the average number of particle-pairs in each histogram bin. In the absence of detector effects, Fig. 9.4 would exhibit diagonal strips as in Fig. 4.4 (left). The anisotropy from the underlying particle distribution is expected to be in the order of 0.5% of the average number of pairs. The detector effects are found to cause anisotropies which are several orders of magnitude larger than the expected signal.

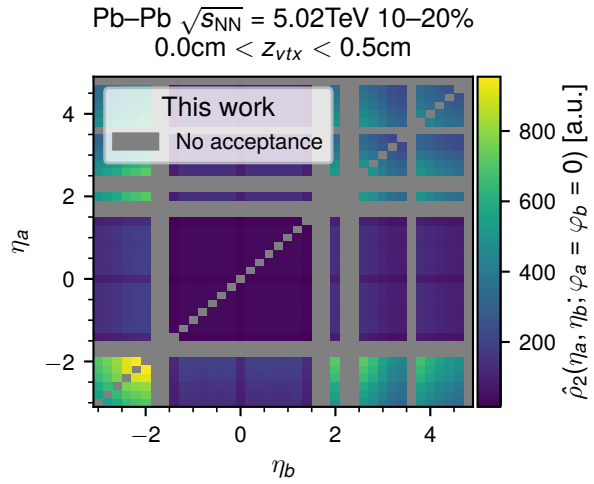

Figure 9.3: Two-particle distribution in the (η_a, η_b)-plane for $0\,\text{cm} \leq z_{\text{vtx}} < 0.5\,\text{cm}$ and $\varphi_a = \varphi_b = 0$. The color-scale represents the average number of pairs per bin. Bins which partly lie outside of the detector acceptance are removed. Pairs between hits in the FMD are the most likely combination due to the large number of secondary particles from material interactions.

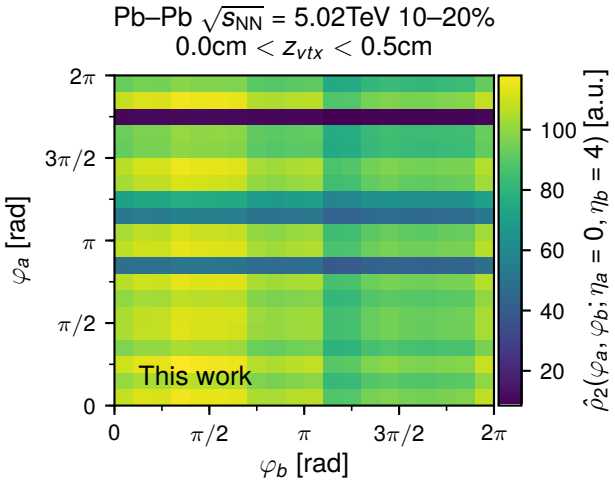

Figure 9.4: Two-particle distribution $\hat{\rho}_2$ in the (φ_a, φ_b)-plane for events occurring at $0\,\text{cm} \leq z_{\text{vtx}} < 0.5\,\text{cm}$ and the η_a and η_b values specified in the label. Detector effects are clearly evident. The distribution is normalized such that it reflects the average number of pairs detected in each bin.

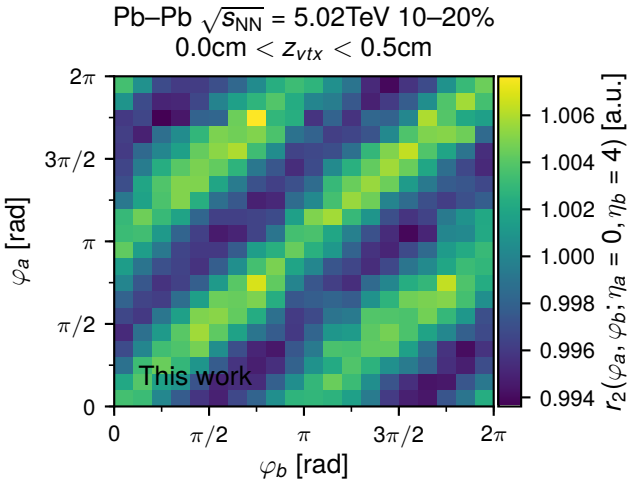

Figure 9.5: Normalized two-particle distribution r_2 in the (φ_a, φ_b)-plane within $0\,\text{cm} \leq z_{\text{vtx}} < 0.5\,\text{cm}$ for $5 - 10\%$ centrality. Each pair is formed from a tracklet in the SPD ($\eta_a \approx 0$) and a hit in the FMD1 ($\eta_b \approx 4$). The detector induced anisotropies seen in Fig. 9.4 have canceled out revealing the underlying anisotropy of the particles created in collisions.

9.3 Reduced two-particle distributions

The reduced two-particle distribution is formed from $\hat{\rho}_1$ and $\hat{\rho}_2$ as defined in Eq. (3.3). Uncorrelated detector efficiencies are expected to cancel out making r_2 the basis for the later Fourier decomposition. This section presents r_2 as projections onto the (φ_a, φ_b)-plane and, after applying the coordinate transformation described in Sec. 4.4.3, onto $\Delta\varphi$.

r_2 in the (φ_a, φ_b)-plane

Fig. 9.5 depicts r_2 in the (φ_a, φ_b)-plane where pairs are formed between SPD-tracklets at $\eta_a \approx 0$ and hits in the FMD1 at $\eta_b \approx 4$. The shown distribution is computed for events with $0 < z_{\text{vtx}} < 0.5\,\text{cm}$. The presented phase-space is therefore identical to the one shown in Fig. 9.4 for $\hat{\rho}_2(\eta_a, \eta_b)$. The diagonal stripes expected for an averaged two-particle distribution are clearly visible.

$\Delta\varphi$-projections of r_2

Fig. 9.6 depicts r_2''; the $\Delta\varphi$ projection of $r_2(\eta_a, \eta_b, \varphi_a, \varphi_b)$ for all studied centralities. The particle-pairs were again formed from SPD-tracklets ($\eta_a \approx 0$) and hits in the FMD1 ($\eta_b \approx 4$) to be compatible with the previous figures. Each centrality exhibits a clear azimuthal anisotropy corresponding to v_2. The magnitude of the anisotropies is smallest for the most central collisions and reaches a maximum in the 40–60% centrality bin.

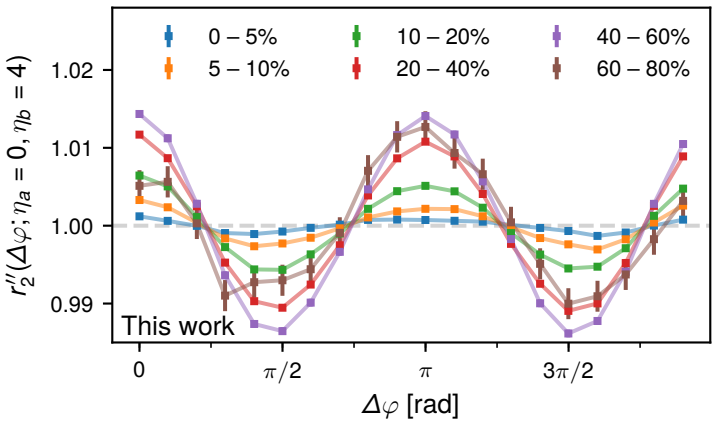

Figure 9.6: Projection of r_2 onto $\Delta\varphi$ (labeled as r_2'') for various centralities. Azimuthal anisotropies are clearly visible for each centrality.

9.4 Two-particle Fourier coefficients $\hat{V}_{n,-n}(\eta_a, \eta_b)$

The Fourier coefficients $\hat{V}_{n,-n}(\eta_a, \eta_b)$ are computed from the $\Delta\varphi$-projection of r_2. The results of that computation are shown for $n = 2$ in Fig. 9.7 (left) for events with $0 < z_{\text{vtx}} < 0.5\,\text{cm}$. The respective relative statistical uncertainties are shown in the right hand panel. Pairs between SPD-tracklets exhibit a significantly larger anisotropy than pairs from other regions of the phase-space. This is expected for several reasons. Firstly, the flow coefficient $v_2(\eta)$ is known to decrease with increasing $|\eta|$ [30]. Secondly, the p_{T}-cut imposed during the SPD-tracklet selection biases toward larger values of v_2 [50]. Lastly, the SPD exhibits considerably fewer secondary particles from material interactions.

9.5 Factorization of $\hat{V}_{n,-n}(\eta_a, \eta_b)$ using Model A

The factorization of $\hat{V}_{n,-n}(\eta_a, \eta_b)$ with Model A (see Sec. 3.3.1) focuses primarily on finding the minimal value of $\Delta\eta_{\text{min}}$ below which non-flow effects significantly break the factorization assumption.

9.5.1 $f_2(\eta_a, \eta_b)$ as a function of $\Delta\eta_{\text{min}}$

Fig. 9.8 depicts the factorization ratio as defined in Eq. (3.11) for four different $|\Delta\eta|$-gaps: 1, 2, 2.6 and 3 for events of $0-5\%$ centrality. Pairs with a separation smaller than the required one were excluded from the fitting procedure (indicated by orange vertical lines). Furthermore, short-range pairs between hits in the FMD were also excluded from the factorization procedure due to possible contributions from pairs of secondary particles from material interactions (indicated by diagonal red lines).

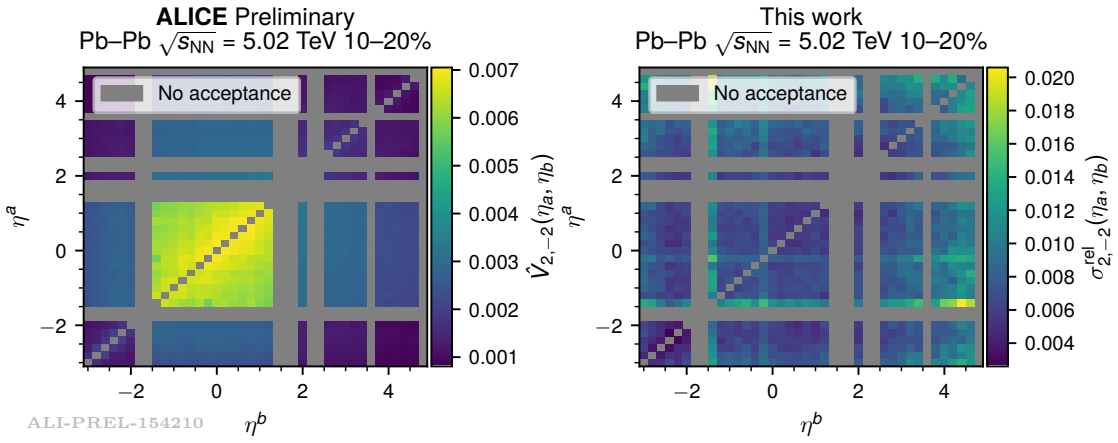

Figure 9.7: Left: Fourier coefficients $\hat{V}_{2,-2}(\eta_a, \eta_b)$ of the normalized two-particle distribution r_2. Right: Relative uncertainties of the coefficients. Both slices depict $0\,\text{cm} < z_{\text{vtx}} < 0.5\,\text{cm}$. Pairs of SPD-tracklets exhibit a larger anisotropy than pairs involving a hit in the FMD.

The relative statistical uncertainties do not differ significantly between the different $|\Delta\eta|$-gaps since they primarily represent the uncertainties of statistical uncertainty of $\hat{V}_{2,-2}(\eta_a, \eta_b)$. Fig. 9.9 depicts the uncertainties for the $|\Delta\eta| > 2.6$ case which can be taken as representative for all four cases.

A deviation from unity indicates that Model A does not describe the observed data in those regions with respect to the region used in the fitting procedure. For all $|\Delta\eta|$-gaps the region along the diagonal of the (η_a, η_b)-plane is not in agreement with the factorization found from the long-range pairs. This finding is expected: the short-range region of the phase-space is known to exhibit a large contribution from non-flow effects such as jets and weak decays. A deviation from unity is also observed along the edges of the involved sub-detectors which coincide with regions of increased statistical uncertainties shown in Fig. 9.9.

The factorization ratio for $|\Delta\eta| \geq 1$ fails to describe the long-range region of $|\Delta\eta| \gtrsim 2$. Increasing the $|\Delta\eta|$-gap from 1 to 2 improves the agreement in the long-range region significantly. A further increase from 2 to 2.6 yields additional minor improvements while a change from 2.6 to 3 does not cause any significant further changes to the factorization ratio. I.e., $|\Delta\eta|$-gaps of 2.6 and 3 yield almost identical $v_2^A(\eta)$.

9.5.2 $f_2(\eta_a, \eta_b)$ as a function of centrality

This section investigates a possible centrality dependence of the factorization ratio in the (η_a, η_b)-plane. Fig. 9.10 depicts the factorization ratio where only pairs with $|\Delta\eta| > 2.6$ were considered during the factorization procedure. All centralities exhibit a non-factorizing behavior for pairs with $|\Delta\eta| \lesssim 1$, whereby the exact width depends on the centrality of the collisions: Central and peripheral collisions show a wider non-factorizing region than mid-central collisions.

Fig. 9.11 shows the projections onto $\Delta\eta$ for each centrality bin in Fig. 9.10. The

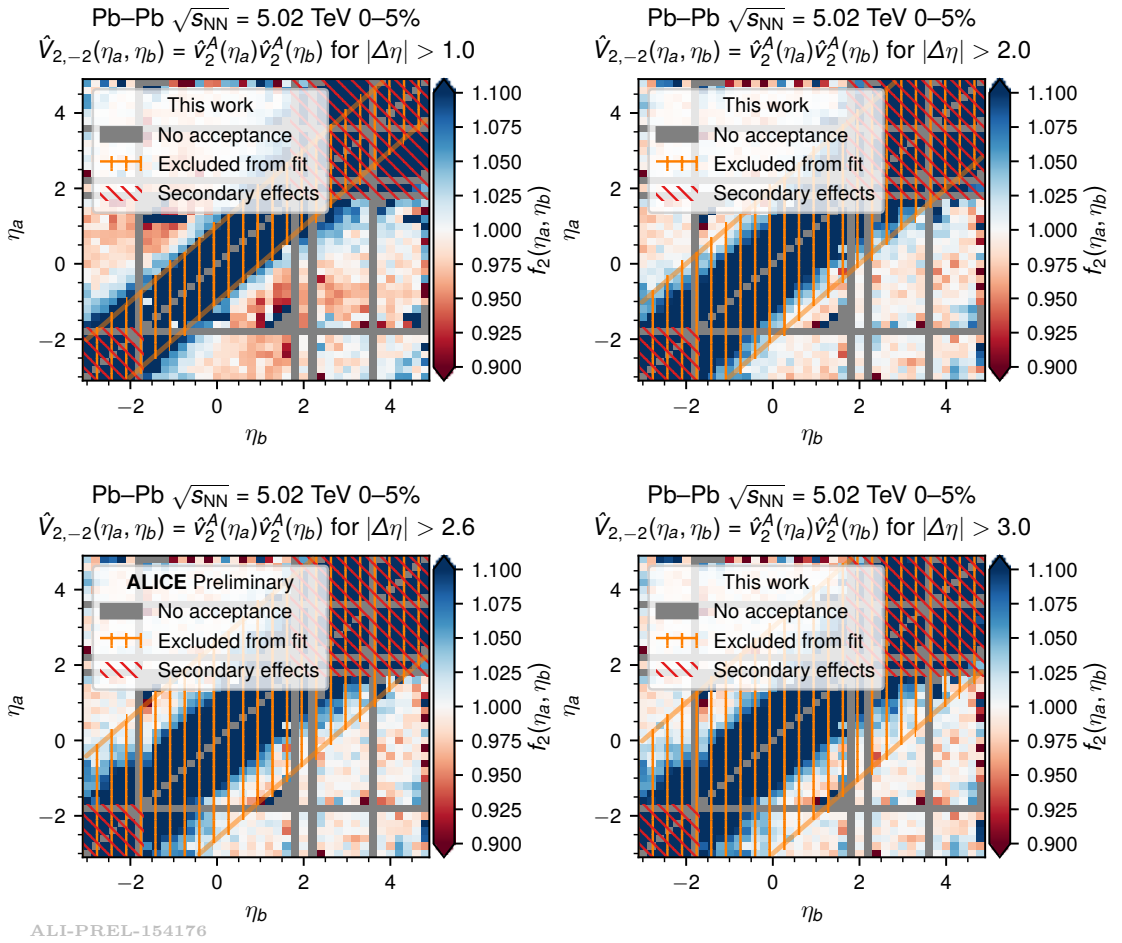

Figure 9.8: $f_2(\eta_a, \eta_b)$ for various $|\Delta\eta|$-gaps imposed during the factorization with Model A and at 0–5% centrality. Factorization does not hold simultaneously for the short and long-range ($|\Delta\eta| \gtrsim 2$) regions for any $|\Delta\eta|$-gap. The $|\Delta\eta|$-gap of 1 is insufficient to describe either region. Minor differences are visible between $|\Delta\eta| > 2$ and $|\Delta\eta| > 2.6$, while the factorized solution does not appear to change between $|\Delta\eta| > 2.6$ and $|\Delta\eta| > 3$.

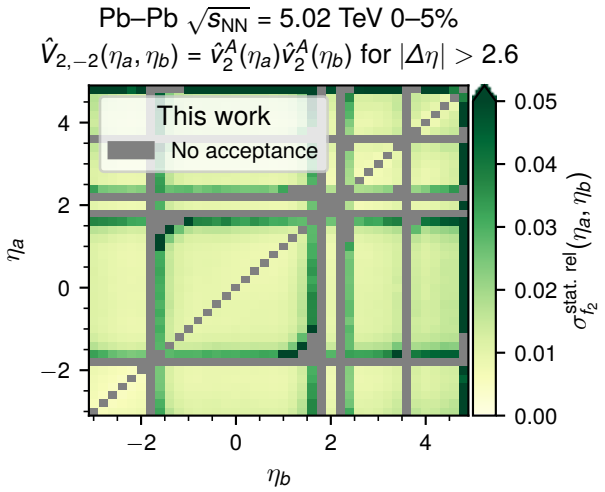

Figure 9.9: Relative statistical uncertainties of $f_2(\eta_a, \eta_b)$. The factorization was performed for pairs with $|\Delta\eta| > 2.6$. The uncertainties for the other $|\Delta\eta|$-gaps in Fig. 9.8 do not differ significantly.

factorization ratios of all centralities are observed to be in agreement with unity for $|\Delta\eta| > 2.6$. The shape of the factorization breaking for pairs with $|\Delta\eta| < 2$ exhibits the centrality dependence also seen in Fig. 9.10.

9.5.3 Uncorrected $v_2^A(\eta)$

The factorization procedure yields the uncorrected flow-coefficients $v_2^A(\eta)$. A correction of the effect caused by secondary particles from material interaction could not be applied in this analysis due to the lack of a suitable MC simulation to date. The uncorrected flow coefficients $v_2^A(\eta)$ are nevertheless presented in Fig. 9.12. The factorization was performed on pairs with $|\Delta\eta| > 2.6$. The observed $v_2^A(\eta)$ in the region of the SPD-tracklets ($-1.7 < \eta < 1.7$) is significantly larger than the regions covered by the FMD. This reflects the minimal p_{T} cut of $p_{\mathrm{T}} \gtrsim 0.75\,\mathrm{GeV/c}$ imposed during the tracklet selection. The relative variation with z_{vtx} is approximately identical for the central and forward/backward region but dependent on centrality. Central (0–5%) and peripheral (40–60%) events varied by $\sim 8\%$ while mid-central collision varied by ($\sim 2.5\%$).

9.6 Factorization of $\hat{v}_{n,n}(\eta_a, \eta_b)$ using Model B

This section presents the results base on Model B as defined in Eq. (3.9). The empirical decorrelation parameter F_2^η for various $|\Delta\eta|$-gaps and centralities is depicted in Fig. 9.13. The fitting procedure yields unstable results for the most central collisions with $|\Delta\eta| > 3$; the respective data point was removed. Central and peripheral collisions exhibit a dependence on the $|\Delta\eta|$-gap imposed during the fitting procedure.

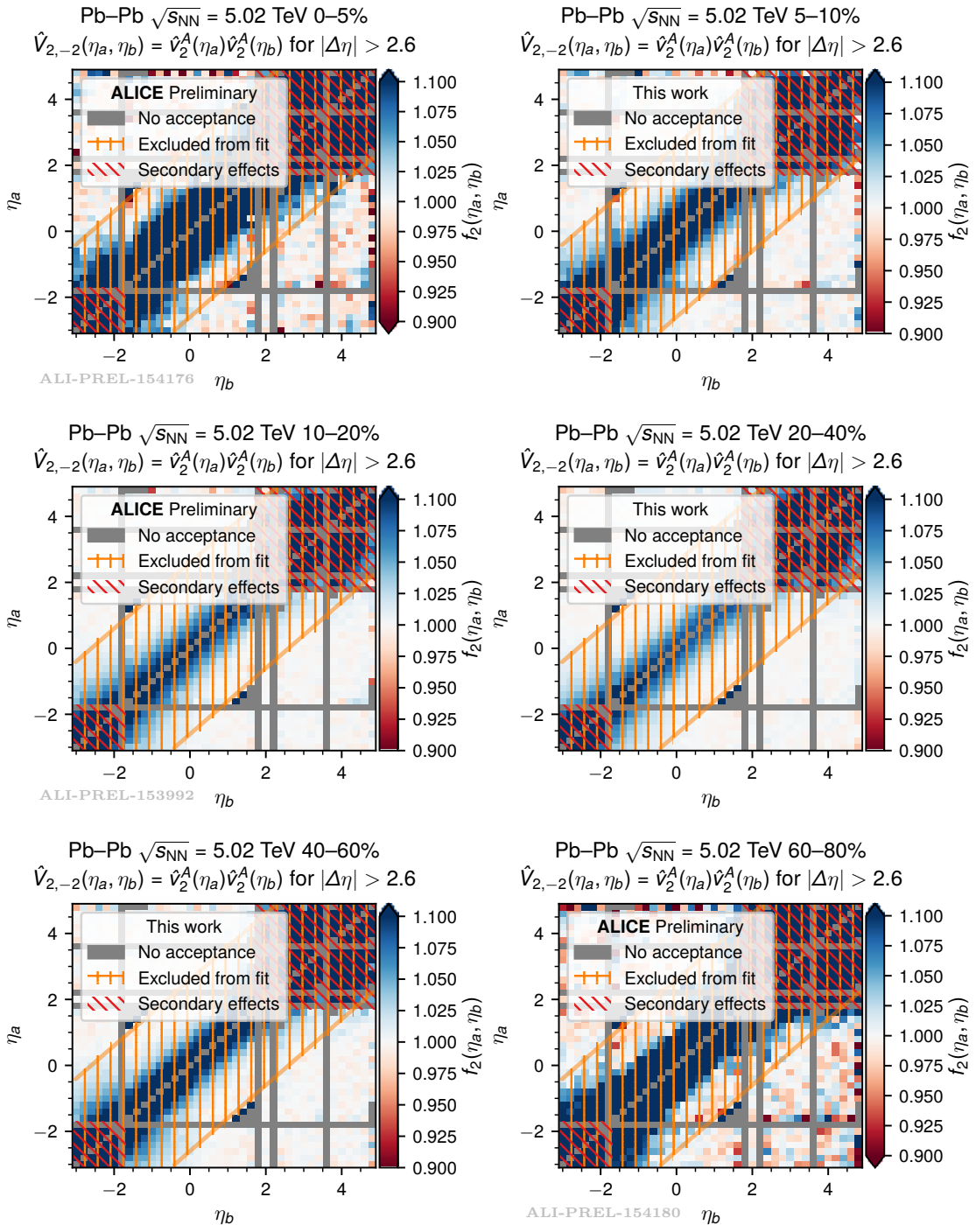

Figure 9.10: Factorization ratios in the (η_a, η_b)-plane for various centrality bins. The width of the non-factorizing region exhibits a centrality dependence.

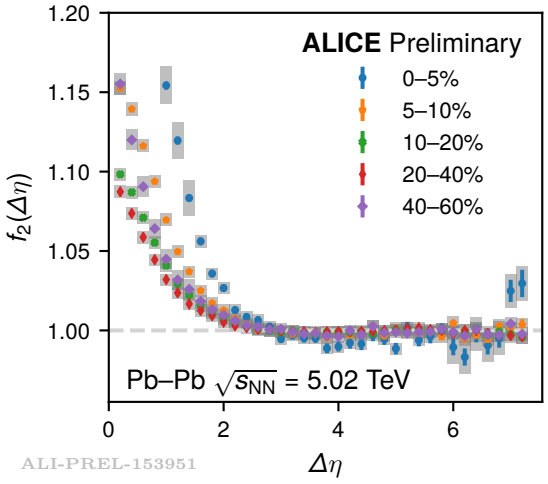

Figure 9.11: Projection of $f_2(\eta_a, \eta_b)$ onto $\Delta\eta$ for each analyzed centrality bin in Fig. 9.10. Only pairs with $|\Delta\eta| > 2.6$ were considered during the fitting procedure with Model A. Systematic uncertainties are shown as shaded gray areas; statistical uncertainties are given as error bars on each point. Good agreement to the model is observed for all centralities with $|\Delta\eta| > 2.6$. The factorization behavior in the region of $|\Delta\eta| < 2$ exhibits a centrality dependence.

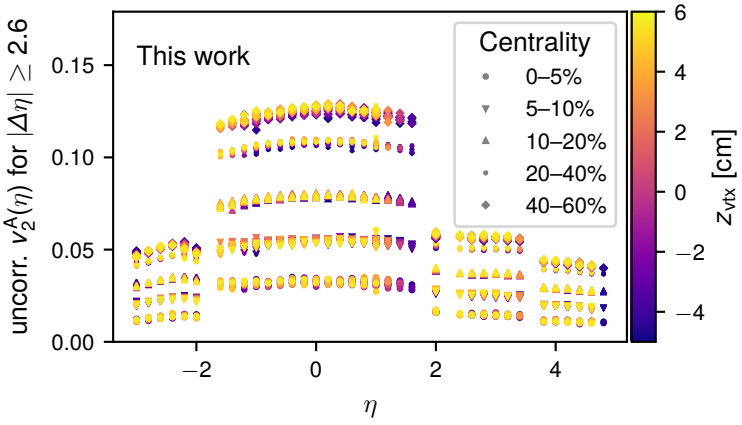

Figure 9.12: Uncorrected $v_2^A(\eta)$ for various centralities. The centrality bin of 60–80% is not shown due to its large statistical uncertainties. The p_T-cutoff imposed on the SPD-tracklets increases the observed v_2^A in the central region while secondary particles from material interaction attenuate the signal in forward/backward regions.

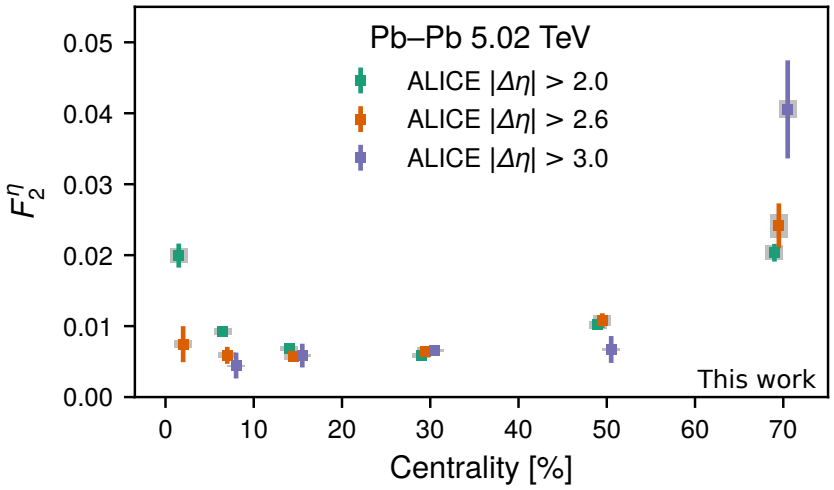

Figure 9.13: Decorrelation parameter F_2^η as a function of centrality. Values are slightly displaced along the x-axis for better readability. The factorization breaking in central and peripheral events exhibits a dependence on the applied $|\Delta\eta|$-gap.

The factorization ratios for Model B with $|\Delta\eta| > 2.6$ are shown in Fig. 9.14. The observed factorization ratios bear a strong resemblance to those obtained with Model A for identical $|\Delta\eta|$-gaps despite F_2^η assuming non-zero values for all centrality bins shown in Fig. 9.13.

9.7 Systematic uncertainties

The discussion of the systematic uncertainties of this analysis is centered around three main potential sources: The approximation of constant efficiency within each bin of the one and two-particle distributions, the choice of the centrality estimator, and the potential effects of pile-up in the high-interaction rate runs of the LHC15o data sample.

The effect of each of these sources is evaluated on the final observables $f_2(\Delta\eta)$ and F_2^η, since a propagation of systematic uncertainties from $\hat{V}_{n,-n}$ through the fitting procedure was deemed unfeasible.

9.7.1 $f_2(\eta_a, \eta_b)$ dependence on the primary vertex bin width

Ideally, the analysis should be conducted in as small bins as possible while maintaining sufficient statistical significance to be able to perform a stable Fourier decomposition in the azimuthal dimensions. A reasonable binning schema which fulfills the above requirements is 40 bins in each η dimension (0.2 bin width), 20 bins in the azimuthal dimensions (the segmentation of the inner FMDs), 6 centrality bins and 22 bins in z_{vtx} (0.5 cm bin width). This section serves as a justification for the z_{vtx}-bin width of 0.5 cm,

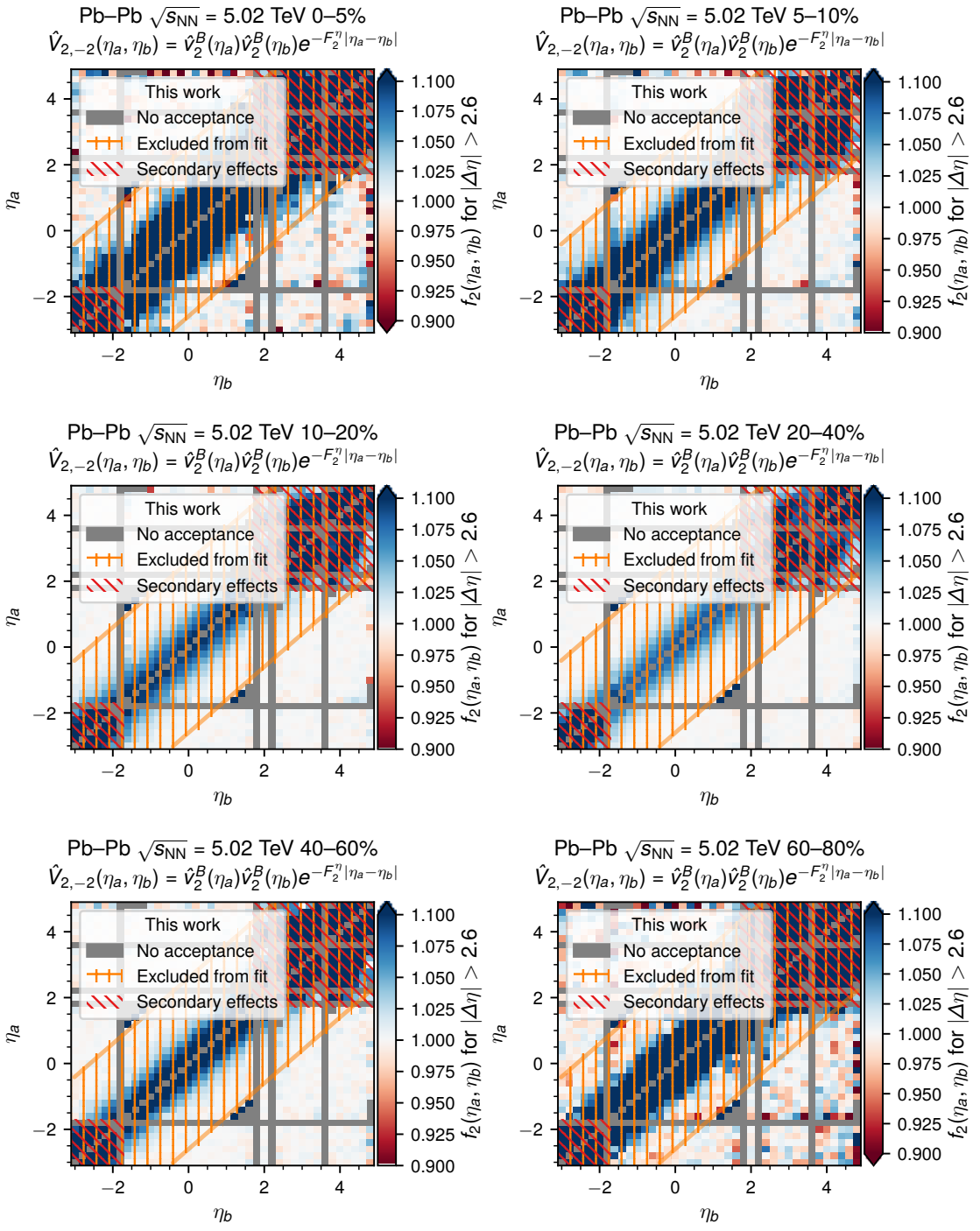

Figure 9.14: Factorization ratios $f_2(\eta_a, \eta_b)$ using Model B and requiring $|\Delta\eta| > 2.6$ for all pairs during the factorization process. Pairs with a large $|\Delta\eta|$-separation are well described by the model. The region of $|\Delta\eta| \lesssim 1.5$ is incompatible with the solution of $v_2^B(\eta)$ and F_2^η found for $|\Delta\eta| > 2.6$.

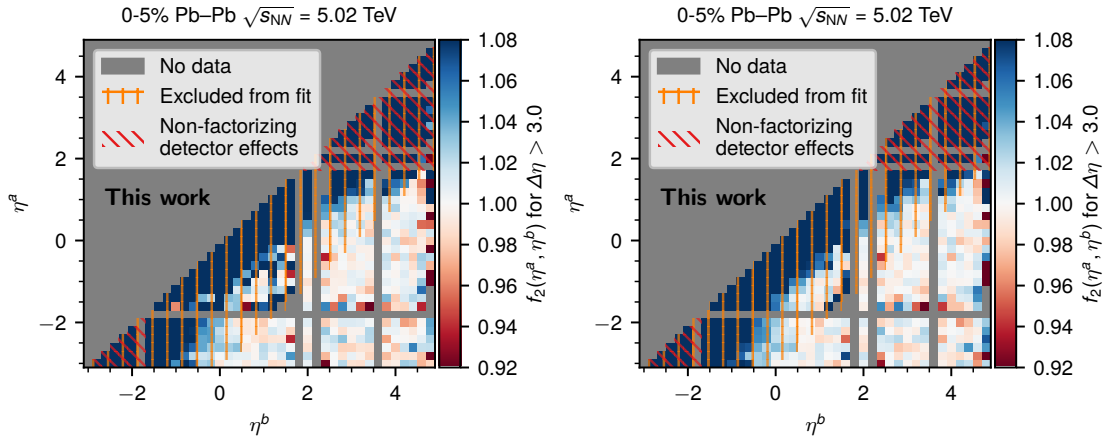

Figure 9.15: Factorization ratio $f_2(\eta_a, \eta_b)$ for a z_{vtx}-bin width of 1 cm (left) and 0.5 cm (right) with $\eta_a < \eta_b$. The fit (Model A) only included particle pairs with $|\Delta\eta| > 3$. The smaller binning leads to better fit results in the mid-range SPD-SPD region, while the fit in the long-range regions remains largely unaffected.

based on qualitative assessments of $f_2(\eta_a, \eta_b)$.

A larger z_{vtx}-bin width of 1 cm, which is more common in ALICE analyses, was considered for this work. Fig. 9.15 depicts $f_2(\eta_a, \eta_b)$ for the two different z_{vtx} bin widths of 1 cm (left) and 0.5 cm (right). The larger bin width yields large bin-to-bin fluctuations in the mid-range region of the SPD-SPD ($1 < |\Delta\eta| < 3$). In comparison, the finer bin width yields a considerably smoother fit in the same region. The region of $|\Delta\eta| > 3$ exhibits no significant dependence on the bin width.

Conducting the measurement again with yet smaller bins in z_{vtx} was found to be unfeasible due to technical limitations by ROOT and the GRID infrastructure[2]. Therefore an alternative method was conceived in order to evaluate if a z_{vtx}-bin width of 0.5 cm is sufficiently small.

The analysis was repeated three times with a z_{vtx} bin width of 0.5 cm but with an overall offset of -0.25 cm, 0 cm, and $+0.25$ cm respectively. If the chosen bin width of 0.5 cm is sufficiently small for the detector effects to cancel out as described in Sec. 7, one expects to find each of the three iteration to yield results compatible within statistical uncertainties[3]. If a significantly larger deviation is observed it is attributed to the approximation of constant efficiency within a given bin.

The method chosen for this study is schematically presented in Fig. 9.16. Each row represents the original and shifted binning respectively, while each rectangle represents

[2]Decreasing the bin width increases the memory usage of this analysis. Analyses running on the GRID cannot consume more than 3 GB of memory. Histograms of more than ~ 1 GB cannot be serialized by ROOT.

[3]Note that statistical fluctuations are expected to be suppressed by the fact that the three observations are conducted on the same event sample and because the shifted bins have a 50% overlap with the original binning. I.e., each of the shifted bins contains approximately 50% of the events found in the original binning.

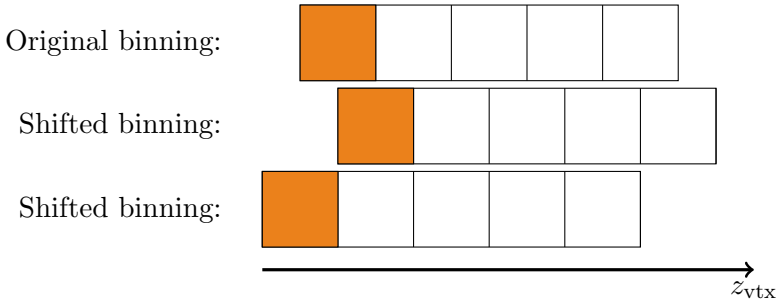

Figure 9.16: Schema for systematic uncertainty evaluation with respect to z_{vtx}-binning. The analysis is conducted with the default binning in z_{vtx} as well as with an offset of $\pm 0.25\,\mathrm{cm}$ in z_{vtx}. The systematic uncertainty for the original bin is estimated based on the measurement in the negatively shifted, the original bin, and the positively shifted bin (orange bins).

a bin of $f_2(\eta_a, \eta_b)$ along the z_{vtx} dimension. The bins marked in orange represent the bins used to compute the variance of $f_2(\eta_a, \eta_b)$ in *one* given bin due to the shift along z_{vtx}. The variance is estimated by comparing the results of the original binning with that of the respective bins in the shifted binning schema. The estimated variance s is given by

$$s = \sqrt{\frac{1}{N-1}\sum_{i=1}^{N}(x_i - \bar{x})^2} \tag{9.1}$$

where $N = 3$ is the number of different binning schemata, x_i is the value of $f_2(\eta_a, \eta_b)$ for schema i and $\bar{x}$ is the mean of $\hat{V}_{n,-n}$ over all three schemata. This allows for the computation of s for each bin in the (η_a, η_b)-plane.

The variance $s(\eta_a, \eta_b)$ corresponding to each bin $f_2(\eta_a, \eta_b)$ was computed on the LHC15o high interaction rate sample over the range of $-5\,\mathrm{cm} < z_{\mathrm{vtx}} < 6\,\mathrm{cm}$. The estimated variance was found to be in agreement with the statistical uncertainty.

9.7.2 Systematic uncertainties of $f_2(\Delta\eta)$

The following investigates the impact of the z_{vtx} offset, the choice of the centrality estimator, and possible pile-up contributions on the observable $f_2(\Delta\eta)$. Depending on $\Delta\eta$, $f_2(\Delta\eta)$ is composed from data of different detector combinations (see Fig. 7.7). Therefore, different systematic uncertainties for different values of $\Delta\eta$ are expected. The following evaluates systematic uncertainties in three distinct $\Delta\eta$ regions:

SPD-SPD dominated ($|\Delta\eta| < 1.5$) This region is dominated by pairs of SPD tracklets

FMD-SPD dominated ($1.5 < |\Delta\eta| < 4.7$) This intermediate region mainly contains pairs composed of one SPD-tracklet and one hit in the FMD

FMD-FMD dominated ($|\Delta\eta| > 4.7$) This region exclusively contains pairs of FMD hits

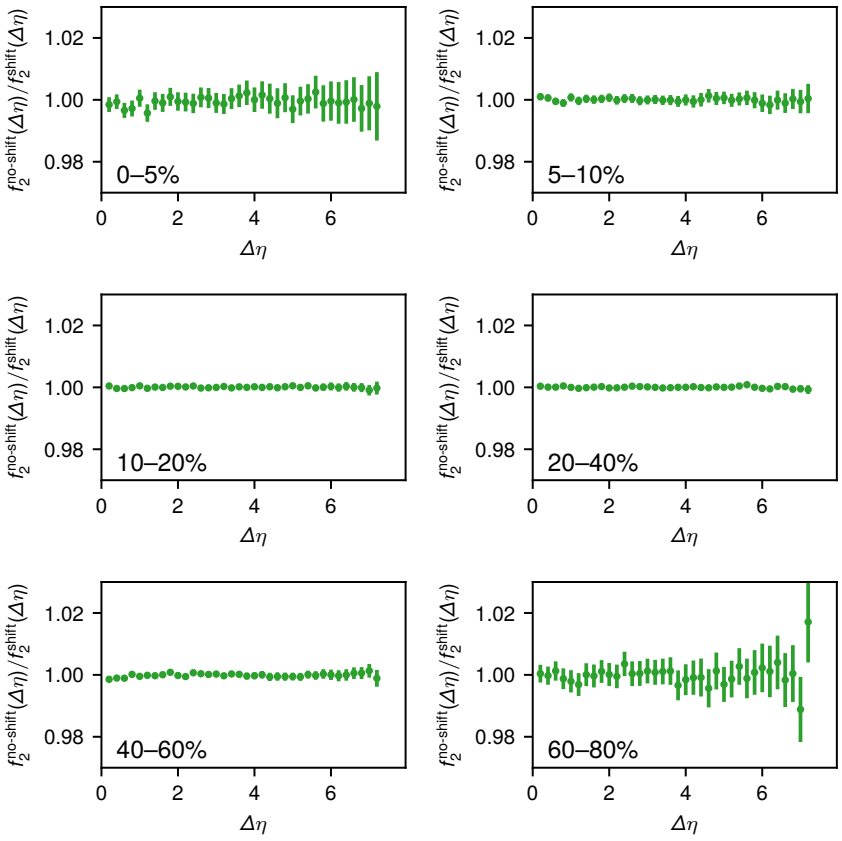

Figure 9.17: Ratio of $f_2(\Delta\eta)$ computed for the default binning and the binning shifted by 0.25 cm along z_{vtx}. No significant deviation from unity is observed for any of the centrality bins.

z_{vtx}-offset

Fig. 9.17 shows the ratio of $f_2(\Delta\eta)$ obtained using the default binning schema divided by $f_2(\Delta\eta)$ computed with the described offset of 0.25 cm along z_{vtx}. No significant deviation is observed for any of the studied centrality intervals and thus no systematic uncertainty is attributed to the z_{vtx}-position or bin width.

Centrality estimator

Generally, it would be preferable to deploy a centrality estimator which does not overlap with the acceptance used in the measurement, since this may lead to unwanted biases. However, due to the large η acceptance of this analysis, no estimator which would reliably work for all centrality classes is available. The V0 detector is commonly used as a centrality estimator, but its z_{vtx}-dependent η-overlap with the FMD made it an unfeasible choice for this analysis. In order to minimized possible z_{vtx}-dependent effects, this analysis uses centrality estimators based on the SPD. Namely:

Table 9.1: Summary of systematic uncertainties of $f_2(\Delta\eta)$. Individual uncertainties are added in quadrature to form the final uncertainty.

		Assigned uncertainty [%]		
	Centrality [%]	$\lvert\Delta\eta\rvert < 1.5$	$1.5 < \lvert\Delta\eta\rvert < 4.7$	$\lvert\Delta\eta\rvert > 4.7$
z_{vtx}-shift	0–20	0.3	0.1	0.1
	20–80	0.1	0.1	0.1
Centrality estimator	0–5	0.5	0.5	0.8
	5–60	0.3	0.3	0.4
	60–80	5	0.5	0.8
Pile-up	0–5	0.5	0.2	0.5
	5–80	0.2	0.2	0.4
Total	0–5	1	0.4	1
	5–40	0.4	0.4	0.4
	40–60	0.6	0.4	0.4
	60–80	5	0.4	0.6

CL0 (default) Number of clusters in the inner most layer of the SPD

SPD tracklets Number of tracklets reconstructed in the SPD

The impact of the centrality estimator choice on $f_2(\Delta\eta)$ is again evaluated by computing this quantity for both estimators and forming the ratio. The result of this procedure is depicted in Fig. 9.18. The most significant deviation is observed for short-range pairs in peripheral events; this region is dominated by pairs of SPD-tracklets. The gray bands indicate the systematic uncertainties assigned to each region in $\Delta\eta$. The exact values can be found in Tab. 9.1.

Pile-up

Pile-up was considered as a final source of uncertainty on $f_2(\Delta\eta)$. The results presented in Fig. 9.11 were computed based on runs with a high interaction rate (HIR). HIR runs exhibit larger pile-up effects than comparable runs at a low interaction rate (LIR)[4]. For a systematic evaluation of pile-up effects, it is desirable to perform this analysis on the HIR and LIR data set separately. The LIR data set contains approximately ~ 1.3 million events which pass the event-selection criteria (15% of the HIR data set). This number of events is too small to perform this analysis. Therefore, a comparison was done between the HIR data set alone and a combined data set (HIR + LIR). The ratios of $f_2(\Delta\eta)$ computed from either data set is shown in Fig. 9.19. The assigned systematic uncertainties are visualized as gray regions. The precise value assigned to each region can be found in Tab. 9.1.

[4]See Appendix B for details on the used data sets

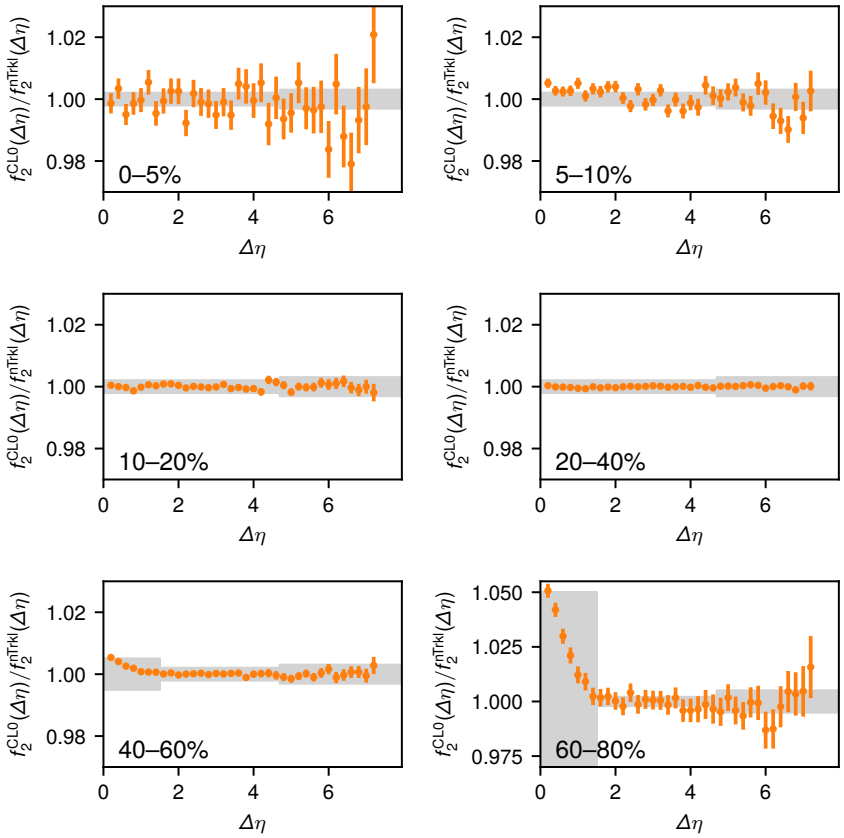

Figure 9.18: Ratio of $f_2(\Delta\eta)$ using the CL0 centrality estimator and number of tracklets. Deviations from unity indicate a bias in $f_2(\Delta\eta)$ due to the centrality estimator. Gray areas indicate the assigned systematic uncertainties.

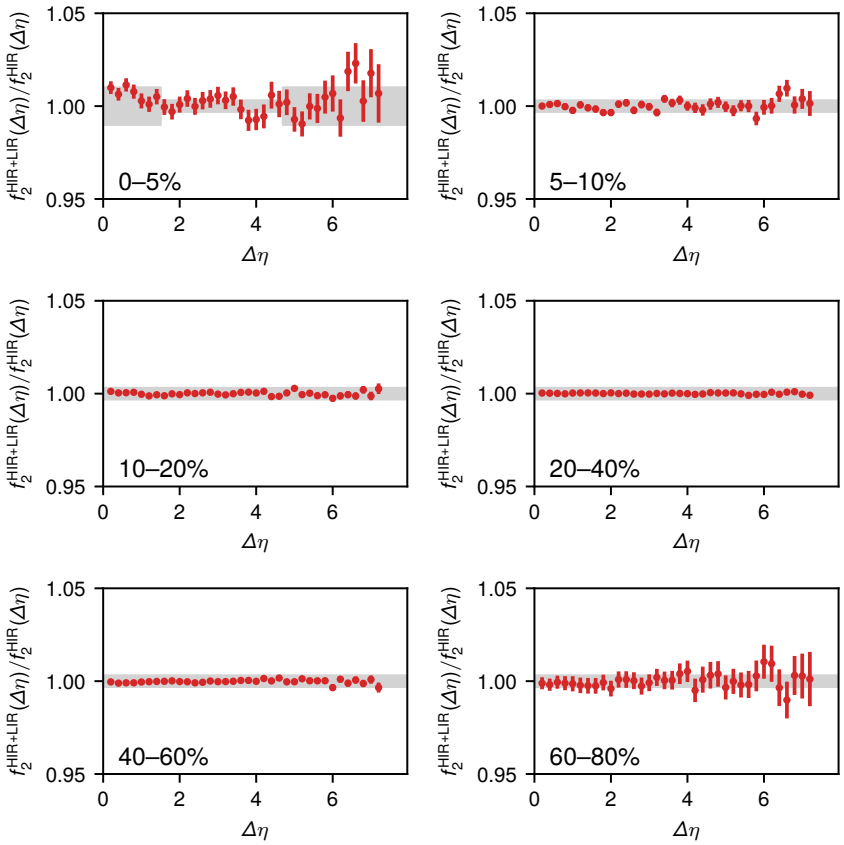

Figure 9.19: Systematic uncertainty of $f_2(\Delta\eta)$ due to pile-up. For these figures $f_2(\Delta\eta)$ was computed on the combined HIR + LIR data set and divided by $f_2(\Delta\eta)$ of the HIR data set. Gray areas indicate the assigned systematic uncertainties.

Table 9.2: Summary of systematic uncertainties of F_2^η for various $|\Delta\eta|$-gaps.

Minimal $\|\Delta\eta\|$	Systematic uncertainty [%]
2.0	5
2.6	7
3.0	3

9.7.3 Systematic effects on F_2^η

The systematic uncertainties of F_2^η were estimated by performing the analysis with variations in the centrality estimator, z_{vtx}-offset, and pile-up contributions. Furthermore, a possible systematic uncertainty due to secondary particles inducing a blurring effect in the (η_a, η_b)-plane was investigated.

Centrality estimator, z_{vtx}-offset, and pile-up

Analogous to the discussion in Sec. 9.7.2, F_2^η is computed with the following variations:

- The combined HIR + LIR data set
- Number of SPD tracklets as the centrality estimator
- Shifted by 0.5 cm along z_{vtx}

These three variations are compared to the default configuration (HIR data set, CL0 centrality estimator and no z_{vtx} offset). The result of each configuration for different $|\Delta\eta|$-gaps is shown in Fig. 9.20. Variations between the four configurations are found to be in the order of their statistical uncertainties make the estimation of the underlying systematic uncertainties challenging. The deviations with respect to the default analysis are added in quadrature and fitted with a constant value over all centrality bins. The resulting values of the systematic uncertainties for each $|\Delta\eta|$-gap are given in Tab. 9.2. The fit of the most central bin for $|\Delta\eta| > 3$ was found to be unstable for the various systematic checks. Therefore, that point is not included in the final results.

Decorrelation effects due to secondary smearing in pseudorapidity

Similar to the blurring of the azimuthal distribution of particles described in Sec. 7.3 it is reasonable to assume a similar effect in the longitudinal direction. Fig. 9.21 depicts the $\Delta\eta$-distribution of particles hitting the FMD with respect to their primary mother particles created in the collision. The secondary particles from material interaction create a blurring effect i.e., the observed η value of a particle is randomly distributed around the η value of its primary mother.

If the event-plane Ψ_n depends on η such a smearing may ultimately affect the event-plane twist parameter F_2^η. The successful MC closure test described in Sec. 7.6 indicates that any such systematic effect must be less than the statistical uncertainties of the

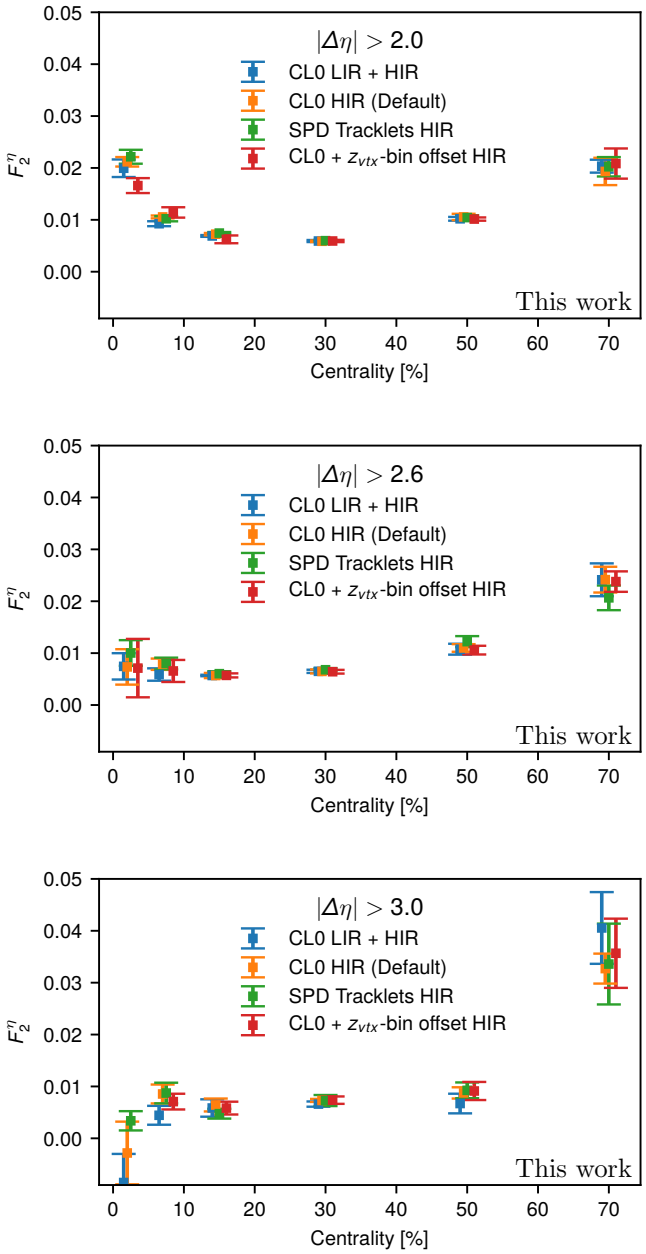

Figure 9.20: F_2^η computed under various changes of the experimental conditions. Each figure presents the data for a different $|\Delta\eta|$-gaps applied during the fitting process. For all but two points the variations are found to be in agreement with the default measurement within statistical uncertainties. Exceptions are the most central bins with $|\Delta\eta| > 2$ and $|\Delta\eta| > 3$. Details on the treatment of these points is given in the text.

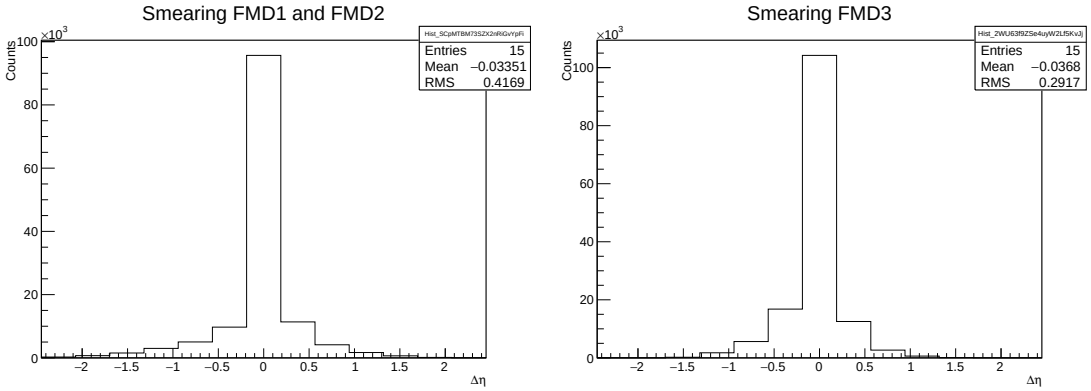

Figure 9.21: Distribution of secondary particles hitting the FMD with respect to their primary particle produced in the collision. A non-zero mean is observed in the forward and backward region.

closure test. However, the statistical uncertainties of the MC closure test are large (up to $\approx 20\%$) and the number of reconstructed events is insufficient to perform a reliable fit with Model B.

Therefore, a Monte Carlo toy simulation was performed in order to further investigate the effect of secondary particles on F_2^η. The premise of the toy model was as follows. According to Model B each point in the $\hat{V}_{n,-n}(\eta_a, \eta_b)$ is attenuated by the factor

$$c(\eta_a, \eta_b) = e^{-F_2^\eta |\eta_a - \eta_b|} = e^{-F_2^\eta |\Delta\eta|} \tag{9.2}$$

The effect of secondary particles can be thought of as blurring in η: instead of comparing the event-planes at η_a and η_b one compares the planes at $\eta_a + \epsilon_a$ and $\eta_b + \epsilon_b$ where ϵ is a random, Gaussian distributed, variable simulating the random deflection of a particle due to material interaction. The distribution has a with of $\sigma_{\text{smear}}/2$, and a mean of μ.

The toy model applies such a random deflection to the η-values in Eq. (9.2) in a MC-like manner:

1. c is computed for all points in the (η_a, η_b)-plane using the same bin widths as in the analysis. However, c is not evaluated at the bin center $(\eta_a^{\text{cent}}, \eta_b^{\text{cent}})$ but at $(\eta_a^{\text{cent}} + \epsilon_a, \eta_b^{\text{cent}} + \epsilon_b)$.

2. The fitting algorithm for Model B is run on the points computed in step 1 yielding $F_2^{'\eta}$ - the decorrelation parameter modified by the blurring due to secondary particles.

3. Step 1 and 2 are repeated 10000 times

4. Step 1, 2, and 3 are repeated for various values of σ_{smear} and μ

The distributions shown in Fig. 9.21 suggest values of $\mu = 0.04$ and $\sigma_{\text{smear}} = 0.5$. Assuming the decorrelation parameter to be $F_2^\eta = 0.01$ the effect of the η-blurring on

F_2^η was found to be less than 0.5%. No systematic uncertainties were assigned to the final results of F_2^η due to this effect.

Chapter 10

Discussion

This chapter discusses the result presented in the previous chapter and compares them to related studies and simulations. Sec. 10.1 discusses the various factorization ratios obtained for different $|\Delta\eta|$-gaps and presents the smallest possible longitudinal separation where the factorization assumption still holds. The knowledge of this minimal separation is important for various other measurements where factorization is implicitly assumed to hold and $|\Delta\eta|$-gaps are routinely applied to suppress di-jet related non-flow contributions. The empirical decorrelation parameter F_2^η, measured by fitting $\hat{V}_{2,-2}(\eta_a, \eta_b)$ to Model B, is compared to AMPT calculations and CMS results in Sec. 10.2.

10.1 Minimally sufficient pseudorapidity separation $\Delta\eta_{\mathbf{min}}$

The $\Delta\eta$-projections of $f_2(\eta_a, \eta_b)$ shown in Fig. 9.11 shows the agreement of the measured $\hat{V}_{2,-2}(\eta_a, \eta_b)$ to Model A when only considering pairs with $|\Delta\eta| > 2.6$ during the fitting procedure. The measured data is found to be in agreement to the model for points with a larger longitudinal separation than 2.6 ± 0.2 for all studied centralities. Performing the factorization with $|\Delta\eta|$-gaps larger than 2.6 only includes pairs in the factorization procedure which were already in agreement to the model for the smaller $|\Delta\eta|$-gap of 2.6. Therefore, increasing the $|\Delta\eta|$-gaps beyond 2.6 is not expected to yield results which differ from those obtained with $|\Delta\eta| > 2.6$. Fitting procedures which include pairs of $|\Delta\eta| < 2.6$, on the other hand are expected to yield different results since pairs which are not compatible with the long-range region of the phase-space are included. This behavior is observed in Fig. 9.8. It is therefore concluded that the minimally sufficient $|\Delta\eta|$-gap for which the factorization ansatz holds in the long-range region is $\Delta\eta_{\mathrm{min}} = 2.6 \pm 0.2$ for the kinematic region studied in this analysis.

This result is also reproduced in AMPT calculations at $\sqrt{s_{\mathrm{NN}}} = 5.02\,\mathrm{TeV}$. The $\Delta\eta$-projection of $f_2(\eta_a, \eta_b)$ (for $|\Delta\eta| > 2.6$) obtained from these calculations is depicted in Fig. 10.1. Pairs with a longitudinal separation larger than 2.6 are found to be in agreement with Model A for all centralities. Pairs with a smaller separation exhibit a centrality dependent incompatibility with the factorized result. The centrality dependent ordering of the factorization breaking in the region of $|\Delta\eta| < 2.6$ is also found to be in

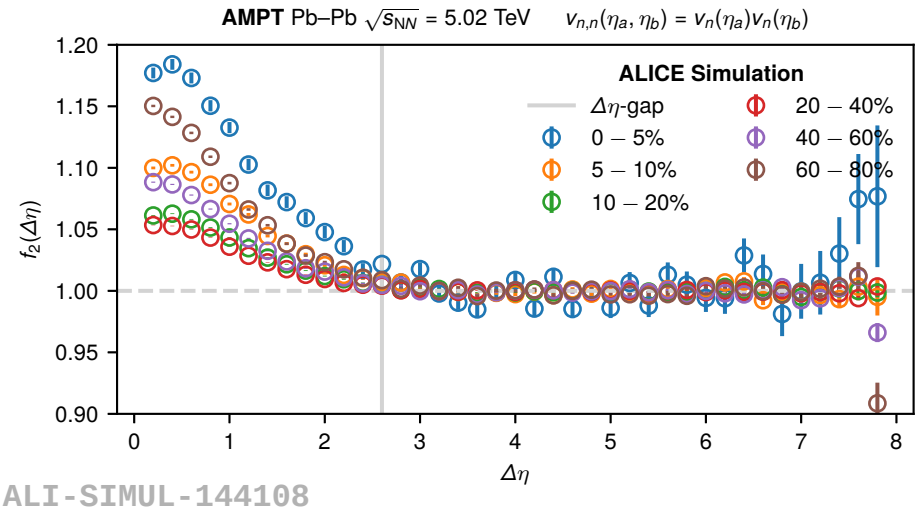

Figure 10.1: Projection of $f_2(\eta_a, \eta_b)$ (based on Model A) onto $\Delta\eta$ for AMPT calculations with string-melting enabled. The factorization was performed using Model A requiring a minimal pair-separation of $|\Delta\eta| > 2$ (vertical gray line). Only statistical uncertainties are shown. The data is in good agreement to the data for $|\Delta\eta| > 2.6$.

agreement with the measured data. This centrality dependence of the factorization breaking may be caused by the centrality dependence of $v_2^A(\eta)$ as shown in Fig. 9.12. Central events exhibit the smallest anisotropic flow of all measured centrality classes. This may make non-flow effects in central events more apparent than in collisions which exhibit a stronger anisotropic flow.

A required minimal separation of $\Delta\eta_{\text{min}} = 2.6 \pm 0.2$ may appear to be in contradiction to previous results. A previous study of the $\Delta\eta$-dependent factorization of two-particle distributions performed by the ATLAS collaboration suggested that a $|\Delta\eta| > 2$ is a sufficient separation [51]. The factorized model was found to be compatible with the observed two-particle distributions to within 5%–10% percent for particles with $p_{\text{T}} < 3$–$4\,\text{GeV}/c$ for the 70% most central collisions. The results presented here have a considerably smaller uncertainty than the ones quoted by the ATLAS collaboration. Fig. 9.11 shows that the deviation from unity at $\Delta\eta = 2$ observed in this work is compatible with the uncertainties quoted by the ATLAS collaboration.

10.2 Empirical decorrelation parameter F_2^η

This section compares the parameter F_2^η as presented in Fig. 9.13 to AMPT calculation and measurements conducted by the CMS collaboration on Pb–Pb collisions at $\sqrt{s_{\text{NN}}} = 2.76\,\text{TeV}$ as described in Sec. 5. The combination of all data points is shown in Fig. 10.2.

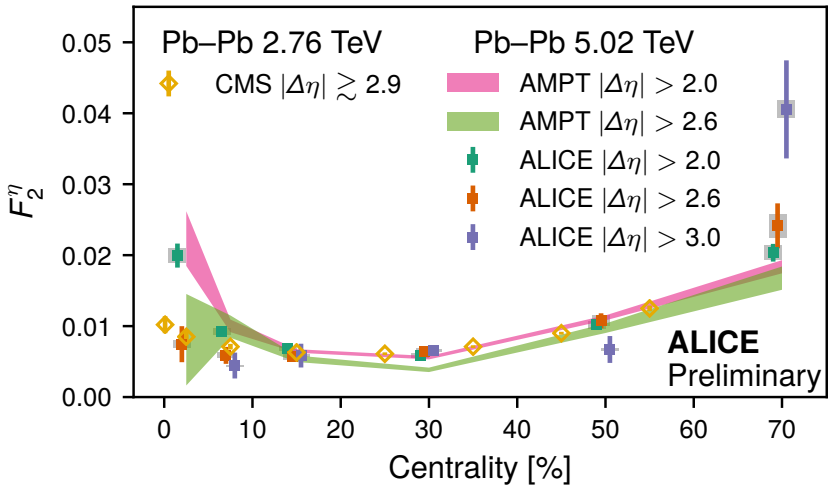

Figure 10.2: Comparison of the empirical factorization breaking parameter F_2^η at different $|\Delta\eta|$-gaps at 5.02 TeV as well as to CMS results at 2.76 TeV. The CMS and ALICE results were measured from different kinematic regions. AMPT calculations were conducted with string-melting enabled.

10.2.1 Comparison to AMPT

The analysis procedure used to estimate F_2^η in AMPT was identical to the one chosen for the experimental ALICE data. The AMPT sample used in this work (see Appendix B.3) exhibited issues with respect to the most central events, increasing the statistical uncertainty for that bin significantly. AMPT with string melting successfully reproduced the decorrelation effects seen in the experimental data. Since the decorrelation effects are dominated by the initial state fluctuations, this suggests that the initial stage fluctuations in AMPT (provided by HIJING) are comparable to those present in Pb–Pb collisions at $\sqrt{s_{\mathrm{NN}}} = 5.02\,\mathrm{TeV}$. Compatible findings for AMTP with respect to the below discussed CMS results have also been published in Ref. [21].

10.2.2 Comparison to CMS results

This section compares the measurements of this analysis to published results from CMS [6] based on the non-factorizing Model B introduced in Sec. 3.3.2. The two methods differ significantly from each other and are conducted in different kinematic regions. Furthermore, the CMS results are based on Pb–Pb collision at $\sqrt{s_{\mathrm{NN}}} = 2.76\,\mathrm{TeV}$. The published CMS results correspond approximately to a $|\Delta\eta|$-gap of 2.9 in this analysis. Despite the difference between the two analyses, good quantitative agreement with the CMS results is observed in all centralities when applying a $|\Delta\eta|$-gap of 2.6. This suggests that the decorrelation effects exhibit only a minor energy dependence. A recent study by the ATLAS collaboration studying the energy dependence of F_2^η corroborates this

observation [7].

The decorrelation effect observed for events of 0–5% centrality exhibits a dependence on the applied $|\Delta\eta|$-gap. With respect to the observed centrality dependence of the factorization breakdown discussed in Sec. 10.1, it appears likely that the $|\Delta\eta|$-gap dependence originates from non-flow effects.

Chapter 11

Conclusion and outlook

This work presents a study of fluctuation and decorrelation effects in the two-particle Fourier coefficients $\hat{V}_{2,-2}(\eta_a, \eta_b)$. The study was conducted using a robust method which enables precise measurements even in the presence of large numbers of secondary particles from material interactions, a non-uniform acceptance, and the lack of precise MC simulations of the detector response. Two common models describing the Fourier coefficients in the (η_a, η_b)-plane were investigated:

Model A assumes that $\hat{V}_{n,-n}(\eta_a, \eta_b)$ can be written as the product of two identical functions of η. This model is defined in Eq. (3.7). It is commonly assumed to hold true in various analyses studying azimuthal anisotropies in multi-particle distributions.

Model B was recently suggested by the CMS collaboration to study decorrelation effects which depend on the longitudinal distance between particle pairs [6]. The decorrelation effect is empirically quantified with the parameter F_n^η. This model is defined in Eq. (3.9)

Model A was used to investigate the minimal $\Delta\eta$-separation required between particles in order for short-range non-flow effects to be negligible with respect to the factorization assumption. For the kinematic regions studied in this analysis, that value was found to be $\Delta\eta_{\mathrm{min}} = 2.6 \pm 0.2$. Analyses which implicitly rely on the factorization assumption to hold true should ideally apply $\Delta\eta_{\mathrm{min}}$ as their $|\Delta\eta|$-gap.

Model B was used to measure F_2^η for various centrality bins. Agreement to measurements performed by the CMS collaboration for Pb–Pb collisions at $\sqrt{s_{\mathrm{NN}}} = 2.76\,\mathrm{GeV}$ was observed over all centrality bins provided the factorization procedure was performed on pairs with $|\Delta\eta| > 2.6$. This corroborates previous observation by the ATLAS collaboration suggesting that the observed decorrelation effect exhibits only a minor dependence on the center-of-mass energy [7]. A dependence on the size of the applied $|\Delta\eta|$-gap for the 0–5% centrality bin was observed raising the question of possible non-flow contributions to the results obtained in that centrality bin.

Future research deploying the here presented method should be extended to smaller collision systems such as pp and pPb collisions and to Fourier modes other than $n = 2$.

Decorrelation effects in pPb collisions were already studied by the CMS and ATLAS collaboration [6, 7] while a similar study of the collective effects observed in pp collisions [52] has not yet been conducted. Understanding if the factorization assumption holds for two-particle distributions of pp collisions would provide valuable insight into the mechanisms creating the observed correlations.

Furthermore, the method presented here allows for a simultaneous factorization in p_{T} as well as η with minimal modifications. A future analysis could therefore measure the flow coefficients $v_n(\eta, p_{\mathrm{T}})$ as suggested by Eq. (2.7). A proof-of-concept of such an analysis is presented in Appendix D.

Abbreviations

CERN European Organization for Nuclear Research.

DPG Data Preparation Group.

IP Interaction Point.

FMD Forward Multiplicity Detector.

TPC Time Projection Chamber.

ITS Inner Tracking System.

SPD Silicon Pixel Detectors.

SDD Silicon Drift Detectors.

SSD Silicon Strip Detectors.

QGP Quark-Gluon-Plasma.

QCD Quantum-Chromodynamics.

CGC Color-Glass-Condensate.

ALICE A Large Ion Collider Experiment.

LHC Large Hadron Collider.

RHIC Relativistic Heavy Ion Collider.

SM Standard Model.

MC Monte Carlo.

HI Heavy Ion.

FFT Fast Fourier Transform.

PDF Probability Pensity Function.

AOD Analysis Object Data.

ESD Event Summary Data.

AMPT A Multi Phase Transport model.

HIJING Heavy Ion Jet Interaction Generator.

ZPC Zhang's Parton Cascade.

ART A Relativistic Transport.

Appendix A

$\hat{V}_{2,-2}(\eta_a, \eta_b)$ for all centralities

This appendix presents $\hat{V}_{2,-2}(\eta_a, \eta_b)$ and the associated statistical uncertainties for $0 < z_{\mathrm{vtx}} < 0.5\,\mathrm{cm}$.

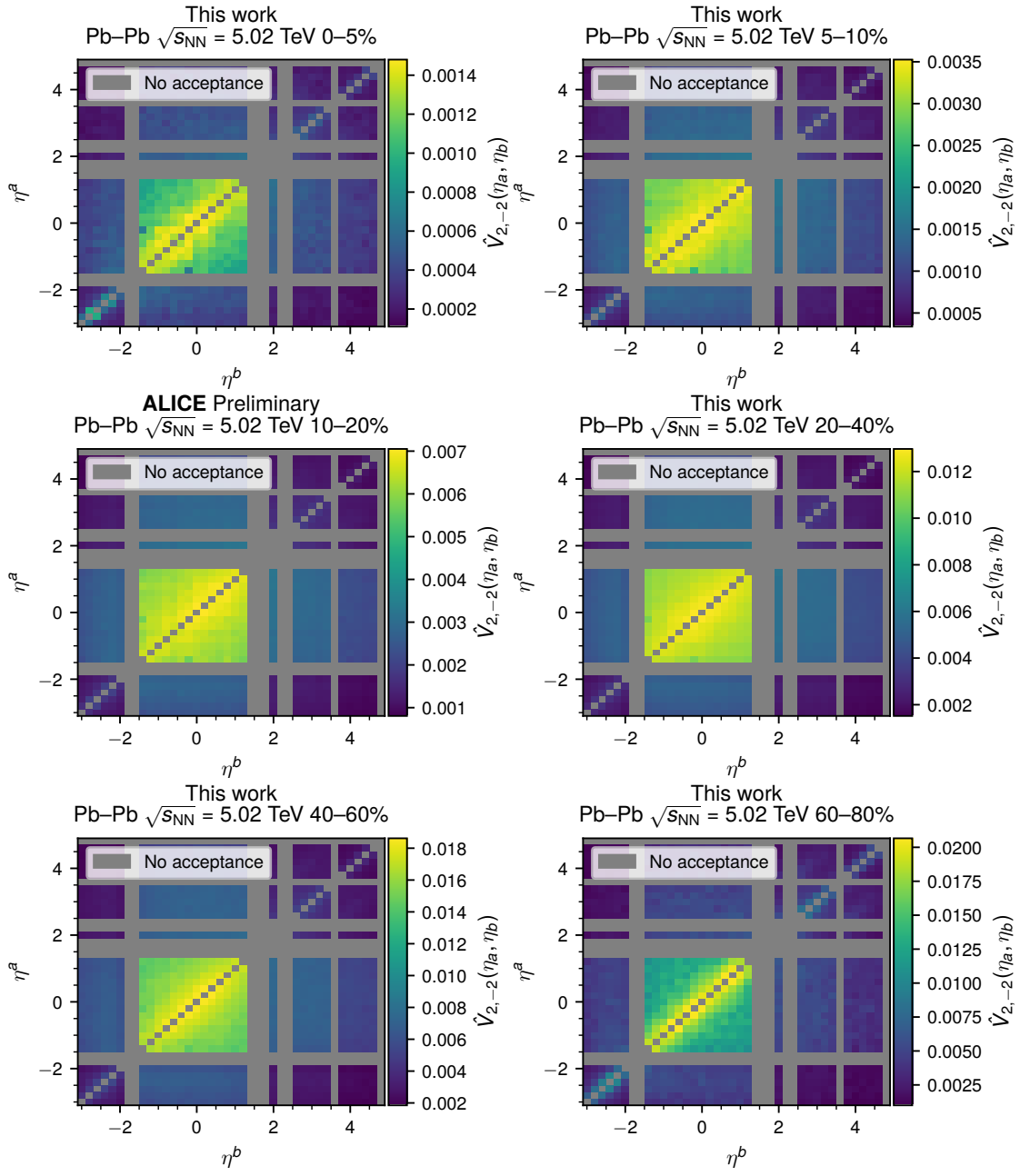

Figure A.1: $\hat{V}_{2,-2}(\eta_a, \eta_b)$ for various centralities and primary vertex positions within $0 < z_{\mathrm{vtx}} < 0.5\,\mathrm{cm}$.

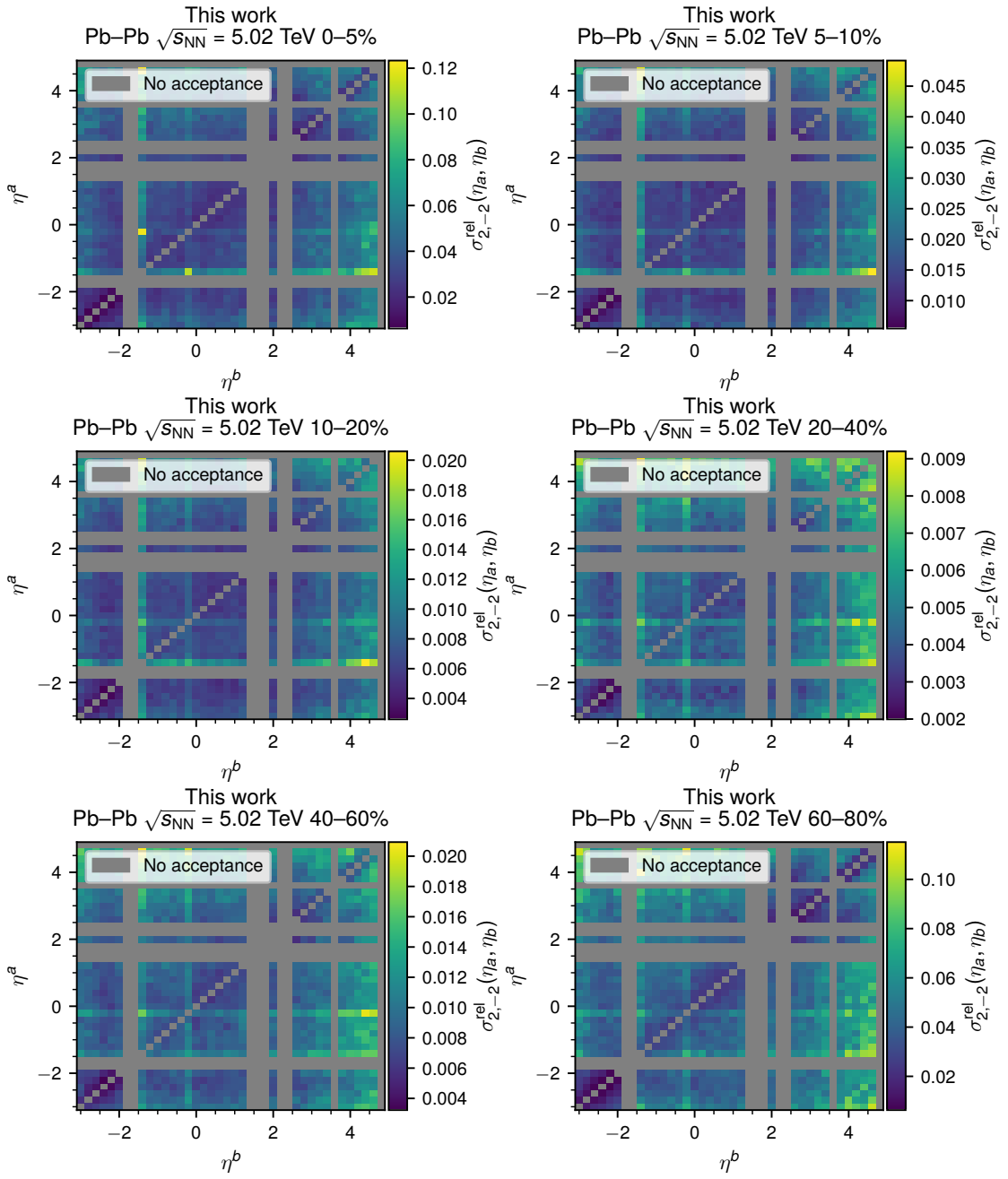

Figure A.2: Relative statistical uncertainties of $\hat{V}_{2,-2}(\eta_a, \eta_b)$ for various centralities and primary vertex positions within $0 < z_{\mathrm{vtx}} < 0.5\,\mathrm{cm}$.

Appendix B

Data sets

This analysis is performed on data sets of Pb–Pb collisions at $\sqrt{s_{\mathrm{NN}}} = 5.02\,\mathrm{TeV}$ recorded in 2015 by ALICE. All runs listed below are marked as "good" by ALICE's data preparation group and the FMD is marked as "good" in the logbook. Furthermore, the reconstructed data is available in the Analysis Object Data (AOD) format. This results in all good runs having at least the V0, ITS, and FMD detectors available.

B.1 LHC15o pass5 low interaction rate

The runs in this data set were recorded at a low interaction rate (LIR) with respect to the considerably larger high interaction rate sample. The LIR data set is expected to have negligible pile-up and is therefore used to asses the pile-up effects in the high interaction rate sample. This data set contains approximately 5 million events of which 1.3 million pass the event selection criteria.

data directory `/alice/data/2015/LHC15o/`

data pattern `pass5_lowIR/AOD194/*/AliAOD.root`

data type aod

run list 245068, 245066, 245064, 244983, 244982, 244980, 244975, 244918, 244917

B.2 LHC15o pass1 high interaction rate

This data set is composed of runs which were recorded at a high interaction rate (HIR). However, the FMD was not included in the data taking at the beginnings of each fill of the LHC. Instead, the FMD was only included once the luminosity had decreased sufficiently for the FMD to work reliably. Nevertheless, HIR runs including the FMD may still exhibit larger pile-up effects than runs in the LIR data set. The large luminosity at the beginning of the fills lead to the FMD being excluded from the majority of the runs in this data sample which is reflected in the small number of analyzed runs. This

data set contains approximately 36 million events of which 8.5 million pass the event selection criteria.

data directory `/alice/data/2015/LHC15o/`

data pattern `pass1/AOD194/*/AliAOD.root`

data type aod

run list 246276, 246275, 246185, 246153, 246089, 245963, 245954, 245833, 245705, 245683

B.3 LHC17i2

The AMPT event generator (version 2.26t7) anchored to the LHC15o period was used to generate this data set of Pb–Pb collisions at $\sqrt{s_{\mathrm{NN}}} = 5.02\,\mathrm{TeV}$ data set with the string melting option enabled. A technical issue in AMPT reduced the number of central events in the 0–5% centrality class. Furthermore, an unrelated technical issues caused the FMD to not be available in the produced AODs data set. Thus, this data set could not be used in the MC closure test described in Sec. 7.6, but provided the data for the model comparison in Sec. 10. The total number of events in this data set is approximately 7.4 M.

data directory `/alice/sim/2017/LHC17i2/`

data pattern `AOD/*/AliAOD.root`

data type aod

run list 244918, 244975, 244980, 244982, 244983, 245061, 245064, 245066, 245068, 245145, 245146, 245148, 245151, 245152, 245231, 245232, 245259, 245343, 245345, 245346, 245347, 245349, 245353, 245396, 245397, 245401, 245407, 245409, 245410, 245411, 245439, 245441, 245446, 245450, 245452, 245454, 245496, 245497, 245501, 245504, 245505, 245507, 245535, 245540, 245542, 245543, 245544, 245545, 245554, 245683, 245692, 245700, 245702, 245705, 245729, 245731, 245738, 245752, 245759, 245766, 245775, 245785, 245793, 245829, 245831, 245833, 245923, 245949, 245952, 245954, 246001, 246003, 246012, 246036, 246037, 246042, 246048, 246049, 246052, 246053, 246087, 246089, 246113, 246115, 246151, 246152, 246153, 246178, 246180, 246181, 246182, 246185, 246217, 246222, 246225, 246271, 246272, 246275, 246276, 246390, 246391, 246392, 246424, 246428, 246431, 246434, 246487, 246488, 246493, 246495, 246553, 246575, 246583, 246648, 246675, 246676, 246750, 246751, 246757, 246758, 246759, 246760, 246763, 246765, 246766, 246804, 246805, 246807, 246808, 246809, 246810, 246844, 246845, 246846, 246847, 246851, 246865, 246867, 246870, 246871, 246928, 246945, 246948, 246980, 246982, 246984, 246989, 246991, 246994

B.4 LHC12a11

This data of Pb–Pb collisions is generated with AMPT at $\sqrt{s_{\mathrm{NN}}} = 2.76\,\mathrm{TeV}$. The reconstruction was anchored to the LHC10h[1] period. There are no known issues with this data set at the time of writing and the FMD is fully reconstructed and available in the AOD format. Until the technical issues with the LHC17i2 data set are resolved this is the only data set which includes flow-like azimuthal anisotropies, a reconstruction of the forward detectors and where the data is available in the AOD format. Therefore, this data set was chosen despite its small statistics of only 900k events for the MC-closure test described in Sec. 7.6.

data directory `/alice/sim/2012/LHC12a11{a-g}`

data pattern `AOD157/*/AliAOD.root`

data type aod

run list 137686, 138534, 138653, 139038, 139437

[1] The 2010 Pb–Pb data taking period

Appendix C

Fourier transformations and Convolutions

C.1 Fourier transformations

The Fourier transformation is a central tool in this analysis and therefore warrants a short summary. Throughout this analysis, the following definition of the Fourier transformation is used

$$\mathcal{F}\left(f(x)\right) = \hat{f}(\omega) \stackrel{\text{def}}{=} \int_{-\infty}^{\infty} f(x) e^{-i\omega x} dx \tag{C.1}$$

where f is any integrable function and ω denotes the angular frequency. For the purpose of this analysis, the Fourier transformation will only be applied to azimuthal dimensions which are defined on the interval $[0, 2\pi[$. The function f may have arbitrarily many other dimensions.

Due to the limited φ-interval, ω can only assume integer values n. Therefore, one can write each *complex* Fourier coefficient A_n as

$$A_n = \frac{1}{2\pi}\mathcal{F}\left(f(x)\right) = \frac{1}{2\pi}\int_0^{2\pi} f(x) e^{-inx} dx \tag{C.2}$$

If $f(x)$ is a real function, as is the case for particle densities, the positive and negative frequencies are each others complex conjugate

$$A_n = A^*_{-n} \tag{C.3}$$

Multidimensional Fourier transformations can be performed independently of each other. Therefore, the coefficients $A_{n,m}$ of a two-dimensional transformation of a function $f(x, y)$, defined over $[0, 2\pi[$ in both dimensions is given by

$$A_{n,m} = \left(\frac{1}{2\pi}\right)^2 \int_0^{2\pi}\int_0^{2\pi} f(x, y) e^{-inx} e^{-imy} dx dy \tag{C.4}$$

The integration order in Eq. C.4 can be exchanged i.e., the order in which multiple transformations are applied can be changed.

C.2 Convolutions

This section provides a non exhaustive summary of the properties of convolutions. A convolution of two function can be thought of as computing their "overlap" at a given separation. The convolution of two functions $g(\varphi)$ and $h(\varphi)$ is defined by

$$g(\varphi) * h(\varphi) = \int_{-\infty}^{\infty} g(\varphi - \varphi')h(\varphi)d\varphi' \tag{C.5}$$

$$= \int_{-\infty}^{\infty} g(\varphi)h(\varphi - \varphi')d\varphi' \tag{C.6}$$

Eq. (C.5) serves as the origin of many useful properties of convolutions. The properties which are used in this analysis are:

Commutative The order of elements in a convolution may be inverted, as is immediately clear from the definition in Eq. (C.5)

$$f * g = g * f \tag{C.7}$$

Associative A series of convolutions may be evaluated in any order

$$(f * g) * h = f * (g * h) \tag{C.8}$$

Associative with scalar multiplication A scalar multiplication with a real or complex number a may be applied before or after the computation of the convolution

$$a\,(g * h) = (ag) * h \tag{C.9}$$

Integration of convolutions The integral over a convolution becomes the product of the integral of the two convoluted functions

$$\int_{-\infty}^{\infty} (g * h)(\varphi)d\varphi = \left(\int_{-\infty}^{\infty} g(\varphi)d\varphi\right)\left(\int_{-\infty}^{\infty} h(\varphi)d\varphi\right) \tag{C.10}$$

Convolution theorem A consequence of the previous property is that a Fourier transform $\mathcal{F}$ of a convolution becomes the product of the Fourier transforms of the convoluted functions.

$$\mathcal{F}\{g * h\} = \mathcal{F}\{g\}\mathcal{F}\{h\} \tag{C.11}$$

Appendix D

Simultaneous factorization in η and p_{T}

The following describes a proof-of-concept of how an analysis based on Model A can be extended to simultaneously perform the factorization procedure in η and p_{T}. Such an analysis can be used to disentangle possible decorrelation effects which simultaneously depend on η and p_{T}.

The original definition of Model A given in Eq. (3.7) has to be modified to include the p_{T} dimension according to the flow ansatz in Eq. (2.6). The modified Model A is given by

$$\hat{V}_{n,-n}(\eta_a, \eta_b, p_{\mathrm{T},a}, p_{\mathrm{T},b}) = \hat{v}_n^{A\prime}(\eta_a, p_{\mathrm{T},a})\hat{v}_n^{A\prime}(\eta_b, p_{\mathrm{T},b}) \tag{D.1}$$

The factorization procedure is identical to the one described in Sec. 7.4, with the exception that the best fit solution is not given by an array of values along η but by a matrix representing the (η, p_{T})-plane.

The reduced two particle distribution is also extended by the respective p_{T} dimensions making r_2 a function of $(\eta_a, \eta_b, \varphi_a, \varphi_b, p_{\mathrm{T},a}, p_{\mathrm{T},b})$ which should be measured in separate z_{vtx} and centrality bins as well. The additional resolution in p_{T} is expected to improve the robustness of the reduced two-particle distribution r_2. A $|\Delta\eta|$-gap or a cut on the p_{T}-range can be applied prior to the factorization.

As a proof-of-concept the here presented analysis is conducted on the publicly available ALICE Open Data [53] which provides approximately 3.5 million Pb–Pb collisions at $\sqrt{s_{\mathrm{NN}}} = 2.76\,\mathrm{GeV}$ from the 2010 data-taking period. The analysis is performed on tracks in the central barrel which provides the necessary p_{T} resolution but limits the η-acceptance to $|\eta| < 0.9$. The factorization was performed for pairs with $|\Delta\eta| > 0.8$. The resulting $v_2(\eta, p_{\mathrm{T}})$ for the 20–30% centrality bin is shown in Fig. D.1. The p_{T}-dependence of $v_2(\eta, p_{\mathrm{T}})$ is clearly visible, while the η-dependence is not statistically significant for this data set. An analysis on a larger data set and potentially over a larger η-acceptance my reveal if $v_2(\eta, p_{\mathrm{T}})$ itself can be factorized into $v_2^{\eta}(\eta)v_2^{p_{\mathrm{T}}}(p_{\mathrm{T}})$.

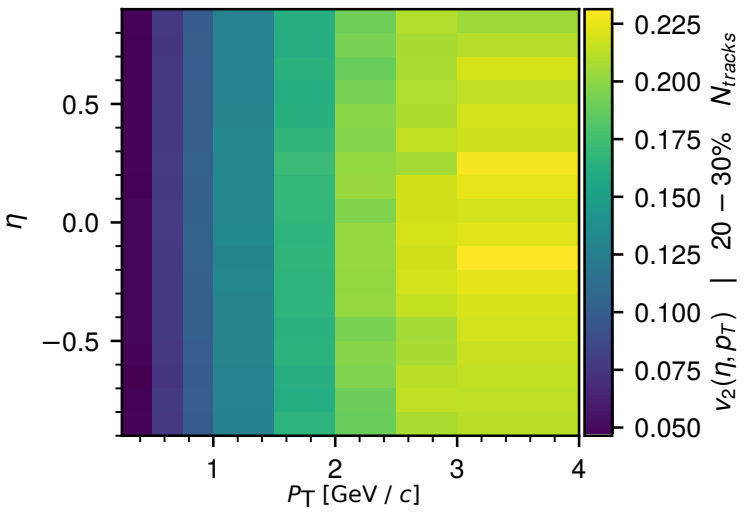

Figure D.1: Flow coefficients $v_2(\eta, p_\mathrm{T})$ in Pb–Pb collisions at 2.76 TeV measured for pairs with $|\Delta\eta| > 0.8$. The factorization was performed simultaneously in η and p_T.

Performance considerations

Performing this analysis using the ALICE software stack (ROOT, AliROOT, and AliPhysics) poses significant technical complications due to the high dimensionality of the involved histograms. Therefore, this proof-of-concept was performed using the milliALICE (mALICE) framework, a custom, open source analysis framework for the ALICE Open Data [54]. The performance improvements of mALICE compared to the default software stack make this analysis easily accessible. The analysis can be performed on the entire public data set on a commodity desktop computer within approximately 4 h.

Bibliography

[1] J. Schukraft. "Heavy-ion physics with the ALICE experiment at the CERN Large Hadron Collider". In: *Philosophical Transactions of the Royal Society A: Mathematical, Physical and Engineering Sciences* 370.1961 (Jan. 2012), pp. 917–932. ISSN: 1471-2962. DOI: 10.1098/rsta.2011.0469.

[2] U. Heinz. "The strongly coupled quark–gluon plasma created at RHIC". In: *Journal of Physics A: Mathematical and Theoretical* 42.21 (May 2009), p. 214003. ISSN: 1751-8121. DOI: 10.1088/1751-8113/42/21/214003.

[3] B. Alver and G. Roland. "Collision geometry fluctuations and triangular flow in heavy-ion collisions". In: *Phys. Rev.* C81 (2010). [Erratum: Phys. Rev.C82,039903(2010)], p. 054905. DOI: 10.1103/PhysRevC.82.039903,10.1103/PhysRevC.81.054905.

[4] ALICE Collaboration. "Harmonic decomposition of two particle angular correlations in Pb-Pb collisions at $\sqrt{s_{\mathrm{NN}}} = 2.76\,\mathrm{TeV}$". In: *Physics Letters B* 708 (Feb. 2012), pp. 249–264. DOI: 10.1016/j.physletb.2012.01.060.

[5] Fernando G. Gardim et al. "Breaking of factorization of two-particle correlations in hydrodynamics". In: *Physical Review C* 87.3 (Mar. 2013). ISSN: 1089-490X. DOI: 10.1103/physrevc.87.031901.

[6] CMS Collaboration. "Evidence for transverse-momentum- and pseudorapidity-dependent event-plane fluctuations in PbPb and pPb collisions". In: *Physical Review C* 92.3 (Sept. 2015). ISSN: 1089-490X. DOI: 10.1103/physrevc.92.034911.

[7] ATLAS Collaboration. "Measurement of longitudinal flow decorrelations in Pb+Pb collisions at $\sqrt{s_{\mathrm{NN}}} = 2.76$ TeV and 5.02 TeV with the ATLAS detector". In: *The European Physical Journal C* 78.2 (Feb. 2018). ISSN: 1434-6052. DOI: 10.1140/epjc/s10052-018-5605-7.

[8] *Elementry particles of the Standard Model*. May 2018. URL: https://en.wikipedia.org/wiki/Standard_Model.

[9] E. V. Shuryak. "Theory of hadron plasma". In: *Sov. Phys.-JETP (Engl. Transl.);(United States)* 47.2 (1978).

[10] Sexty, D. *Non-Zero Density Simulations in Full QCD*. Oct. 2017. URL: http://www.gauss-centre.eu/gauss-centre/EN/Projects/ElementaryParticlePhysics/2017/sexty_pr84to.html?nn=1361054.

[11] U. Heinz and M. Jacob. *Evidence for a New State of Matter: An Assessment of the Results from the CERN Lead Beam Programme*. 2000.

[12] I. Arsene et al. "Quark–gluon plasma and color glass condensate at RHIC? The perspective from the BRAHMS experiment". In: *Nuclear Physics A* 757.1-2 (Aug. 2005), pp. 1–27. ISSN: 0375-9474. DOI: 10.1016/j.nuclphysa.2005.02.130.

[13] B.B. Back et al. "The PHOBOS perspective on discoveries at RHIC". In: *Nuclear Physics A* 757.1-2 (Aug. 2005), pp. 28–101. ISSN: 0375-9474. DOI: 10.1016/j.nuclphysa.2005.03.084.

[14] J. Adams et al. "Experimental and theoretical challenges in the search for the quark–gluon plasma: The STAR Collaboration's critical assessment of the evidence from RHIC collisions". In: *Nuclear Physics A* 757.1-2 (Aug. 2005), pp. 102–183. ISSN: 0375-9474. DOI: 10.1016/j.nuclphysa.2005.03.085.

[15] A. Bracco et al. "NuPECC Long Range Plan 2017 Perspectives in Nuclear Physics". In: (2017).

[16] L. McLerran. *Gluon Saturation and the Formation Stage of Heavy Ion Collisions*. 2008.

[17] P. F. Kolb and U. W. Heinz. "Hydrodynamic description of ultrarelativistic heavy ion collisions". In: (2003), pp. 634–714.

[18] B. Schenke, P. Tribedy, and R. Venugopalan. "Fluctuating Glasma Initial Conditions and Flow in Heavy Ion Collisions". In: *Physical Review Letters* 108.25 (June 2012). ISSN: 1079-7114. DOI: 10.1103/physrevlett.108.252301.

[19] P. Bożek, W. Broniowski, and J. Moreira. "Torqued fireballs in relativistic heavy-ion collisions". In: *Physical Review C* 83.3 (Mar. 2011). ISSN: 1089-490X. DOI: 10.1103/physrevc.83.034911.

[20] P. Bożek and W. Broniowski. "Longitudinal decorrelation measures of flow magnitude and event-plane angles in ultrarelativistic nuclear collisions". In: *Physical Review C* 97.3 (Mar. 2018). ISSN: 2469-9993. DOI: 10.1103/physrevc.97.034913.

[21] Long-Gang Pang et al. "Decorrelation of anisotropic flow along the longitudinal direction". In: *The European Physical Journal A* 52.4 (Apr. 2016). ISSN: 1434-601X. DOI: 10.1140/epja/i2016-16097-x.

[22] B. Schenke and S. Schlichting. "3D glasma initial state for relativistic heavy ion collisions". In: *Physical Review C* 94.4 (Oct. 2016). ISSN: 2469-9993. DOI: 10.1103/physrevc.94.044907.

[23] J. Y. Ollitrault. "Relativistic hydrodynamics for heavy-ion collisions". In: *European Journal of Physics* 29.2 (Jan. 2008), pp. 275–302. ISSN: 1361-6404. DOI: 10.1088/0143-0807/29/2/010.

[24] *Stress–energy tensor*. May 2018. URL: https://en.wikipedia.org/wiki/Stress%5C%E2%5C%80%5C%93energy_tensor.

[25] T. Hirano, N. van der Kolk, and A. Bilandzic. "Hydrodynamics and Flow". In: *Lecture Notes in Physics* (2009), pp. 139–178. ISSN: 1616-6361. DOI: 10.1007/978-3-642-02286-9_4.

[26] C. A. Pruneau. *Data Analysis Techniques for Physical Scientists*. Cambridge University Press, 2017. DOI: 10.1017/9781108241922.

[27] Michael L. Miller et al. "Glauber Modeling in High-Energy Nuclear Collisions". In: *Annual Review of Nuclear and Particle Science* 57.1 (Nov. 2007), pp. 205–243. ISSN: 1545-4134. DOI: 10.1146/annurev.nucl.57.090506.123020.

[28] Miklos Gyulassy and Xin-Nian Wang. "HIJING 1.0: A Monte Carlo program for parton and particle production in high energy hadronic and nuclear collisions". In: *Computer Physics Communications* 83.2-3 (Dec. 1994), pp. 307–331. ISSN: 0010-4655. DOI: 10.1016/0010-4655(94)90057-4.

[29] Zi-Wei Lin et al. "A multi-phase transport model for relativistic heavy ion collisions". In: *Physical Review C* 72.6 (Dec. 2005). ISSN: 1089-490X. DOI: 10.1103/physrevc.72.064901.

[30] ALICE Collaboration. "Pseudorapidity dependence of the anisotropic flow of charged particles in Pb-Pb collisions at $\sqrt{s\_\mathrm{NN}} = 2.76$ TeV". In: *ArXiv e-prints* (May 2016).

[31] Jiangyong Jia et al. "Observables for longitudinal flow correlations in heavy-ion collisions". In: *Journal of Physics G: Nuclear and Particle Physics* 44.7 (June 2017), p. 075106. ISSN: 1361-6471. DOI: 10.1088/1361-6471/aa74c3.

[32] V. Vechernin. "Forward–backward correlations between multiplicities in windows separated in azimuth and rapidity". In: *Nuclear Physics A* 939 (2015), pp. 21–45. ISSN: 0375-9474. DOI: http://dx.doi.org/10.1016/j.nuclphysa.2015.03.009.

[33] B. Alver et al. "Non-flow correlations and elliptic flow fluctuations inAu+Aucollisions atsNN=200GeV". In: *Physical Review C* 81.3 (Mar. 2010). ISSN: 1089-490X. DOI: 10.1103/physrevc.81.034915.

[34] ALICE Collaboration. *ALICE Collaboration*. May 2018. URL: http://alice-collaboration.web.cern.ch/general/index.html.

[35] A. Tauro. *ALICE Schematics*. General Photo. May 2017. URL: https://cds.cern.ch/record/2263642.

[36] K. Aamodt et al. "The ALICE experiment at the CERN LHC". In: *JINST* 3 (2008), S08002. DOI: 10.1088/1748-0221/3/08/S08002.

[37] ALICE Collaboration. *ALICE forward detectors: FMD, TO and VO: Technical Design Report*. Technical Design Report ALICE. Submitted on 10 Sep 2004. Geneva: CERN, 2004.

[38] A. Mastroserio. "Operational experience with the ALICE pixel detector". In: *Journal of Instrumentation* 12.01 (Jan. 2017), pp. C01002–C01002. ISSN: 1748-0221. DOI: 10.1088/1748-0221/12/01/c01002.

[39] C. Holm Christensen et al. "The ALICE Forward Multiplicity Detector". In: *International Journal of Modern Physics E* 16.07n08 (Aug. 2007), pp. 2432–2437. ISSN: 1793-6608. DOI: 10.1142/s0218301307008057.

[40] C Holm Christensen. "The ALICE Forward Multiplicity Detector—From Design to Installation". PhD thesis. Ph. D. thesis, University of Copenhagen, 2009, http://www. nbi. dk/˜ cholm, 2007.

[41] E. Abbas et al. "Performance of the ALICE VZERO system". In: *JINST* 8 (2013), P10016. DOI: 10.1088/1748-0221/8/10/P10016.

[42] A. Bilandzic et al. "Generic framework for anisotropic flow analyses with multiparticle azimuthal correlations". In: *Physical Review C* 89.6 (June 2014). ISSN: 1089-490X. DOI: 10.1103/physrevc.89.064904.

[43] S. Ravan et al. "Correcting Correlation Function Measurements". In: *Phys. Rev.* C89.2 (2014), p. 024906. DOI: 10.1103/PhysRevC.89.024906.

[44] S. van der Walt, S. C. Colbert, and G Varoquaux. "The NumPy Array: A Structure for Efficient Numerical Computation". In: *Computing in Science & Engineering* 13.2 (2011), pp. 22–30. DOI: 10.1109/MCSE.2011.37.

[45] R. Brun and F. Rademakers. "ROOT — An object oriented data analysis framework". In: *Nuclear Instruments and Methods in Physics Research Section A: Accelerators, Spectrometers, Detectors and Associated Equipment* 389.1 (1997). New Computing Techniques in Physics Research V, pp. 81–86. ISSN: 0168-9002. DOI: https://doi.org/10.1016/S0168-9002(97)00048-X.

[46] L. Li. "A new complexity bound for the least-squares problem". In: *Computers and Mathematics with Applications* 31.12 (1996), pp. 15–16. ISSN: 0898-1221. DOI: https://doi.org/10.1016/0898-1221(96)00072-7.

[47] I. N. Bronstein et al. *Taschenbuch der mathematik*. Vol. 1. Springer-Verlag, 2012.

[48] Alexander Colliander Hansen. "Pseudorapidity Dependence of Anisotropic Azimuthal Flow with the ALICE Detector". PhD thesis. Niels Bohr Institute, University of Copenhagen, Oct. 2014.

[49] Jaroslav Adam et al. "Forward-central two-particle correlations in p-Pb collisions at $\sqrt{s_{\mathrm{NN}}} = 5.02$ TeV". In: *PLB* (2015).

[50] Jaroslav Adam et al. "Anisotropic flow of charged particles in Pb–Pb collisions at $\sqrt{s_{\mathrm{NN}}} = 5.02$ TeV". In: *Phys. Rev. Lett.* 116.13 (2016), p. 132302. DOI: 10.1103/PhysRevLett.116.132302.

[51] G. Aad et al. "Measurement of the azimuthal anisotropy for charged particle production in $\sqrt{s_{\mathrm{NN}}} = 2.76$ TeV lead-lead collisions with the ATLAS detector". In: *Physical Review C* 86.1 (July 2012). ISSN: 1089-490X. DOI: 10.1103/physrevc.86.014907.

[52] CMS Collaboration. "Evidence for collectivity in pp collisions at the LHC". In: *Physics Letters B* (June 2016).

[53] ALICE Collaboration. *Pb–Pb data sample at 2.76 TeV from the 2010 data-taking period*. http://opendata.cern.ch/search?page=1&size=20&q=3.5TeV. 2016. DOI: 10.7483/OPENDATA.ALICE.Y4KJ.8HZC.

[54] C. Bourjau. *The mALICE framework*. https://github.com/cbourjau/alice-rs. 2018.

List of Figures

List of Tables